UNIVERSITÀ
DEGLI STUDI
DI PADOVA

Head Office: Università degli Studi di Padova

Department of Geosciences

Ph.D. COURSE IN EARTH SCIENCES

SERIES XXXII

THE PSEUDOTACHYLYTE-MYLONITE ASSOCIATION: AN INSIGHT INTO THE MECHANICS OF DEEP EARTHQUAKES

Coordinator: Prof. CLAUDIA AGNINI

Supervisor: Prof. GIORGIO PENNACCHIONI

Co-supervisor: Prof. LUCA MENEGON

Ph.D. student : SIMONE PAPA

Table of contents

Abstract

The aim of this thesis is to investigate the association of fault rocks formed by seismic deformation with coeval ductile deformation. The only recognised geological record of these two concurrent deformation mechanisms is represented by the relationship between coeval pseudotachylytes (quenched melts produced during seismic slip) and mylonites (high-strain rocks deformed in high-temperature ductile flow). The scientific importance of this association of rocks lies in the fact that their existence in rocks exhumed from below the long-term brittle/ductile transition is a compelling evidence that rheology of the deep crust cannot be treated simply in terms of brittle and ductile models. By investigating associations of coeval pseudotachylytes and mylonites we aim at giving an original and meaningful contribution to the understanding of the mechanisms involved in the interplay in space and time between seismic deformation and ductile flow.

A model proposed to explain such association of fault rocks is "self-localising thermal runaway", assuming a spontaneous acceleration of localized slip in a ductile shear zone eventually leading to seismic slip and melting. This model is supported by numerical modelling, but its application to nature is disputed and speculative. We analyse a pseudotachylyte-ultramylonite association in exhumed lower crustal, quartz-rich metapelites from the Mont Mary nappe of the Western Italian Alps, representing a possible candidate for thermal runaway instability, to find evidence in support or against this process.

- We document by detailed electron backscatter diffraction (EBSD) analysis of quartz-rich layers, the progressive microstructural evolution, at nearly constant temperature conditions (550 °C), to high differential stresses (> 200 MPa) and high strain rates (10^{-9} s^{-1}) within the most strongly deformed portions of the ultramylonite hosting the pseudotachylyte. This microstructural evolution is associated with a switch in deformation mechanism from grain-size-insensitive to grain-size-sensitive creep assisted by grain boundary sliding and creep cavitation. These latest recorded stages of deformation were still aseismic, as the rate-controlling process was precipitation of oriented biotite in cavitation pores.
- We calculate, by calibrated numerical models, the critical conditions for thermal runaway instability in quartz for a wide range of temperature/strain-rate combinations, and determine that deformation in the studied ultramylonite occurred close to the conditions

for the instability to occur. At the same time, we estimate that deformation occurred proximal to brittle-ductile transition for such high strain rates.

- We conclude that the observed pseudotachylyte-mylonite association is best explained by transient downward propagation of seismic rupture from the nearby, overlying base of the seismogenic crust; or by earthquake nucleation below the long-term brittle/ductile transition permitted by the downward deflection of the transition after a large seismic event in the upper crust.

Based on the study of wall-rock garnet coseismic fragmentation in the Mont Mary pseudotachylyte-ultramylonite and on garnet preferential melting within the pseudotachylyte, we suggest a general process for garnet disappearance due to thermal shock fragmentation during co-seismic frictional heating. We show that garnet has the lowest thermal shock resistance between the host rock minerals (garnet, plagioclase, quartz, and sillimanite, in an increasing sequence of resistance), and thus underwent extreme comminution leading to total melting within the frictional melt. Our analysis highlights the critical role of thermal shock as a general process in mineral comminution during the initial stages of co-seismic slip preceding (and promoting) extensive frictional melting. We also present the preliminary results (mechanical and microstructural) of rotary shear experiments designed to reproduce the formation of Mont Mary pseudotachylytes in the lab.

We extend the study of deep crustal pseudotachylytes and pseudotachylyte-mylonite associations to the Calabrian lower crust (Southern Italy) in a preliminary study that aims at paving the way to a further in-depth analysis of Calabrian pseudotachylytes, which represent a unique information source about the rheology of the granulitic continental lower crust. We present microstructural evidence for cyclic pseudotachylyte and mylonite development in the dry lower crust and document the first finding of low-p/high T, cordierite-bearing, peraluminous pseudotachylytes featuring sillimanite microlites.

Riassunto

Lo scopo della presente tesi è di investigare l'associazione di rocce di faglia formata da deformazione sismica coeva a deformazione duttile. L'unica testimonianza geologica della attività simultanea di questi due differenti meccanismi di deformazione è rappresentata dall'associazione coeva di pseudotachiliti (fusi frizionali prodotti durante lo scivolamento sismico) e miloniti (rocce intensamente deformate in maniera duttile ad alta temperatura). La rilevanza scientifica di questa associazione di rocce risiede nel fatto che il loro ritrovamento in rocce esumate da sotto la transizione fragile/duttile, è una chiara evidenza che la reologia della crosta profonda non può essere trattata nei termini di semplici modelli di deformazione fragile o duttile. Tramite lo studio di associazioni esumate di pseudotachiliti e miloniti coeve ci proponiamo l'obiettivo di fornire un contributo originale e significativo alla comprensione dei meccanismi coinvolti nella reciproca interazione, nello spazio e nel tempo, tra deformazione sismica e flusso viscoso.

Un modello proposto per spiegare tale associazione di rocce di faglia è quello delle instabilità duttili (thermal runaway), il quale assume una accelerazione spontanea della velocità di deformazione localizzata in una zona di faglia duttile che risulta in scivolamento a velocità sismiche e fusione della roccia incassante. Questo modello è supportato dalla modellazione numerica, ma la sua applicazione ai casi naturali è ancora materia di dibattito. Abbiamo analizzato una associazione di pseudotachiliti e miloniti in metapeliti ricche in quarzo, esumate dalla crosta profonda, provenienti dalla falda alpina del Mont Mary (Alpi Occidentali). Queste rocce rappresentano una possibile testimonianza geologica di instabilità duttili e quindi le abbiamo analizzate per cercare evidenze a supporto o a discredito di questa interpretazione.

- Abbiamo documentato, tramite analisi di diffrazione di elettroni retrodiffusi (EBSD) su livelli ricchi in quarzo, la progressiva evoluzione della microstruttura, a temperatura pressoché costante (550 °C), verso elevati stress differenziali (> 200 MPa) e velocità di deformazione (10^{-9} s^{-1}) nelle porzioni maggiormente deformate dell'ultramilonite che ospita le pseudotachiliti. Questa evoluzione microstrutturale è associate ad una transizione nel principale meccanismo deformativo da scorrimento viscoso grain-size-insensitive a grain-size-sensitive assistito da grain boundary sliding e cavitazione. Questi ultimi stadi della deformazione viscosa erano ancora asisimici, dato che il processo che limitava la velocità di

deformazione era la precipitazione di lamelle orientate di biotite nei pori aperti dalla cavitazione.

- Abbiamo calcolato, tramite modelli numerici, le condizioni critiche per l'attivazione di instabilità duttili nel quarzo per un'ampia gamma di combinazioni di velocità di deformazione e temperatura. Abbiamo determinato che lo scorrimento viscoso nelle ultramiloniti del Mont Mary avveniva in condizioni non lontane dalla transizione tra flusso stabile e instabile. Allo stesso tempo, abbiamo stimato che la deformazione avveniva in condizioni prossime alla transizione fragile/duttile.
- Abbiamo concluso che l'associazione di pseudotachiliti e miloniti nella falda del Mont Mary può essere spiegata dalla propagazione transiente verso il basso di rotture sismiche dalla base della crosta sismogenetica. Alternativamente, la propagazione di rotture sismiche può causare un aumento di stress e velocita di deformazione nella crosta profonda tale da innescare la nucleazione di rotture sismiche al di sotto della transizione duttile/fragile.

Basandoci sullo studio della fratturazione cosismica del granato nella roccia incassante delle pseudotachiliti e sulla scomparsa preferenziale del granato nel fuso frizionale, abbiamo suggerito un processo generale per la scomparsa del granato dovuto a fratturazione per shock termico durante il riscaldamento frizionale cosismico. Abbiamo dimostrato come il granato abbia la minor resistenza allo shock termico tra i minerali che compongono la roccia incassante (granato, plagioclasio, quarzo, e sillimanite, ordinati per crescente resistenza), e quindi è sottoposto ad una estrema comminuzione che porta alla sua completa fusione all'interno del fuso frizionale. La nostra analisi evidenzia il ruolo dello shock termico come un processo generale di comminuzione dei minerali durante la fase iniziale dello slip cosismico che precede e favorisce la formazione di un fuso frizionale. Presentiamo inoltre i risultati preliminari (dati meccanici e microstrutture) di esperimenti di rotary shear finalizzati a riprodurre la formazione delle pseudotachiliti del Mont Mary in laboratorio.

Infine, abbiamo esteso lo studio delle pseudotachiliti profonde e delle associazioni di pseudotachiliti e miloniti alla crosta inferiore calabrese. Si tratta di uno studio preliminare che intende essere un primo passo verso uno studio dettagliato delle pseudotachiliti calabresi, che rappresentano una finestra unica nella reologia della crosta profonda continentale. Presentiamo evidenze microstrutturali per la formazione ciclica di pseudotachiliti e miloniti nella crosta profonda anidra e documentiamo il primo ritrovamento di pseudotachiliti peralluminose, a cordierite stabile e con microliti di sillimanite, formate in condizioni di alta temperatura e relativamente bassa pressione.

1 Introduction

1.1 General introduction

The yield-strength envelope describes how differential stress (i.e. rock strength) varies with depth (i.e. pressure and temperature) in order to represent the rheology of the lithosphere (Goetze and Evans, 1979; Brace and Kohlstedt, 1980; Kirby, 1983). This kind of model is commonly applied in the modelling of lithospheric deformation (e.g. Handy and Brun, 2004). The yield-strength envelope is composed by the Byerlee's frictional sliding law for brittle failure and the creep equation for viscous crystal-plastic flow. Depending on the assumed geotherm, mineralogy, and water content, different rheological stratification of the lithosphere have been proposed. Current popular yield-strength envelopes envisage either a weak upper mantle rheology in the so-called "crème-brulée" model or strong crustal and mantle layers in the "jelly-sandwich" model (Fig. 1.1; Chen and Molnar, 1983; Schmalholz et al., 2009; Burov and Watts, 2006; Jackson, 2002; Jackson et al., 2008). According to these models, the rheology of the lower crust is largely dependent on water content. Using the

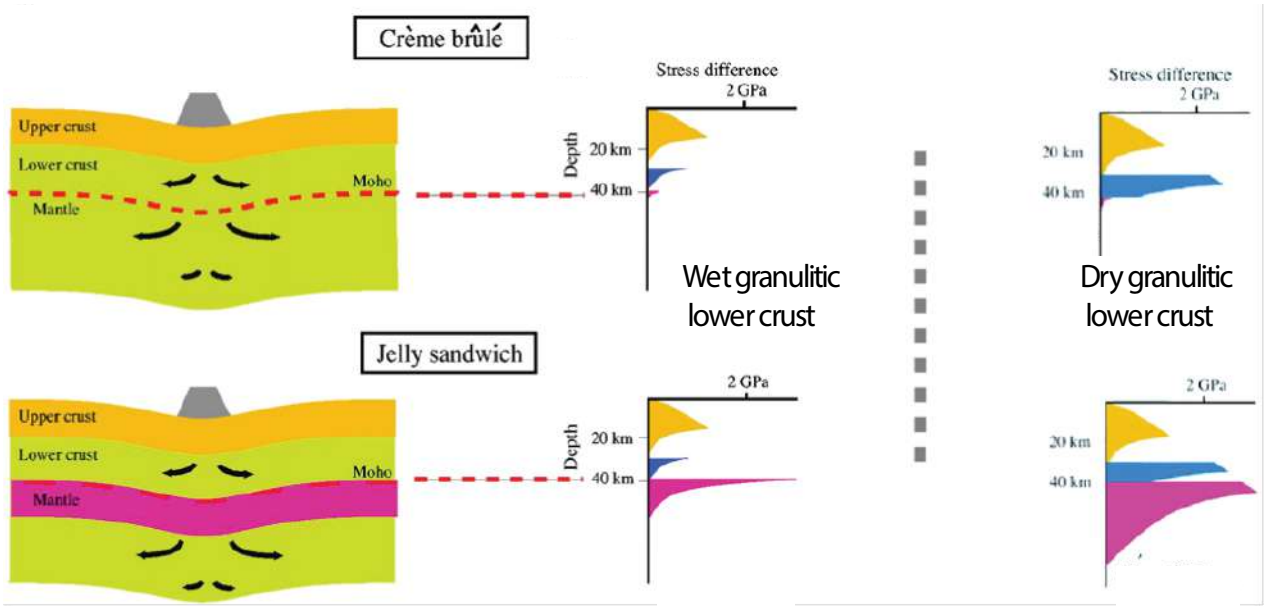

Figure 1. 1 Schematic diagram illustrating contrastingly different models for the long-term strength of continental lithosphere. In the crème-brûlée model, the strength is confined mainly to the uppermost brittle layer of the crust and compensation is achieved mainly by flow in the weak upper mantle. In the jelly sandwich model, the mantle is strong and the compensation for surface loads occurs mainly in the underlying asthenosphere. (from Burov and Watts, 2006).

“wet” flow laws for either quartz or feldspar results in a weak lower crustal layer, while using “dry” flow laws can result in the lower crust being the strongest portion of the lithosphere (Burov and Watts, 2006). It is widely accepted now that large portions of the lower crust are essentially dry (do not contain free fluids), and this would account for a strong and brittle lower crust where large earthquakes can nucleate (Yardley and Valley, 1997; Jamtveit et al., 2000; Jamtveit et al., 2016). In the last twenty years it has been widely demonstrated that there are indeed large-earthquake hypocenters located in the continental lower crust (Deichmann and Rybach, 1999; Maggi, 2000) and examples of lower crustal pseudotachylytes have been discovered in several localities (e.g. Sibson, 1980; Clarke and Norman, 1993; Austrheim and Boundy, 1994; White, 1996; Pennacchioni and Cesare, 1997; Lund and Austrheim, 2003; Lin et al. 2005; Altenberger et al., 2013; Pittarello et al., 2012).

Whichever rheological model we choose to consider, it still implies that large regions of the lithosphere deform exclusively by either brittle fracture or by viscous crystal-plastic flow, with a “brittle-ductile transition” occurring at the depth at which the strength predicted by frictional sliding and flow laws is similar. However, evidence from field observations is piling up that between brittle fracture and ductile flow there is an intimate interplay that involves not only rocks close to the brittle-ductile transition but in the whole middle to lower crust (e.g. Segall and Simpson, 1986; Guermani and Pennacchioni, 1998; Pennacchioni et al., 2006; Pennacchioni and Mancktelow, 2007; Mancktelow and Pennacchioni, 2005; Pennacchioni and Cesare, 1997; Austrheim and Boundy, 1994). For instance, many studies have proved that a dry, and therefore strong, lower crust, despite the high temperature and pressure is very unlikely to deform or to react unless infiltrated by fluids (e.g. Austrheim, 1987; Engvik et al., 2001; Austrheim et al., 1997; Austrheim, 2013; Jamtveit et al., 2018, Petley-Ragan et al., 2018). Even in the hydrated portion of the lower crust, at conditions in which rocks are able to flow at very low differential stresses, brittle precursors are commonly needed in order to localise ductile deformation (e.g. Pennacchioni and Mancktelow, 2007). This implies the occurrence of transient brittle instability during dominant ductile flow. Therefore, it is becoming increasingly clear that bulk rheology and dynamics of the lithosphere cannot be understood in terms of simple brittle and ductile models, but only by considering the intimate interplay in space and time between brittle fracturing, fluid-rock interaction and ductile flow.

Pseudotachylytes are very fine-grained or glassy rocks representing quenched melts produced by frictional heating during seismic slip along a fault (Sibson, 1975). The largest volumes of pseudotachylytes are actually found in association with high grade dry rocks forming the lower

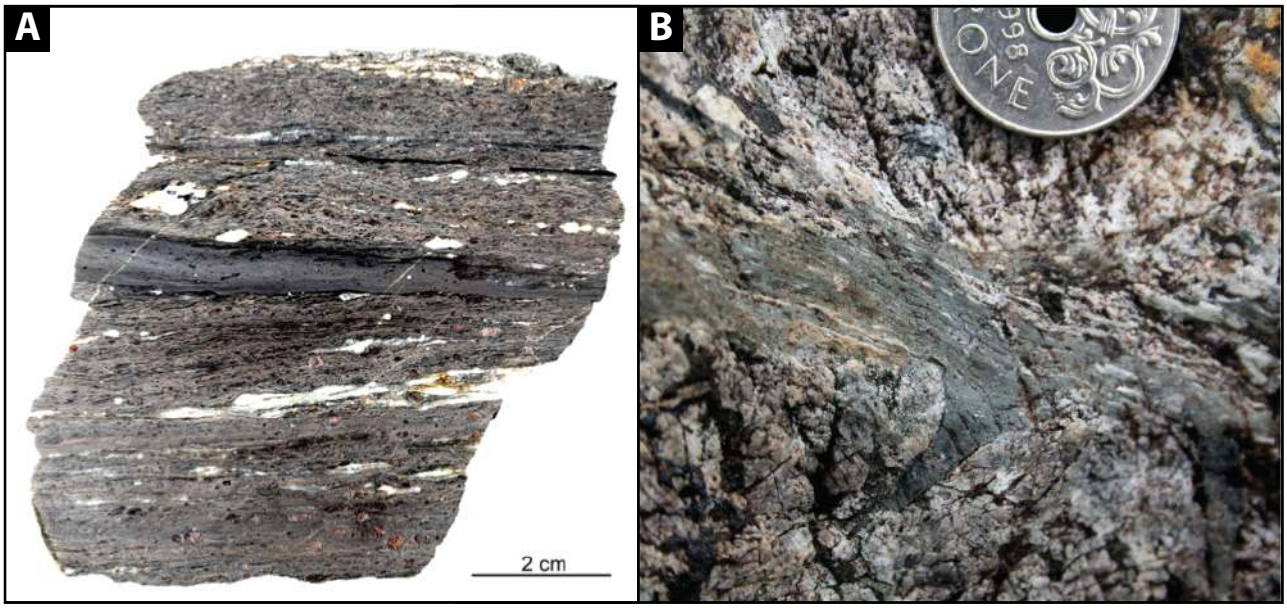

Figure 1. 2 Two end-member examples of pseudotachylyte-mylonite associations. A) Pseudotachylyte developed sub-parallel to the mylonitic foliation of an amphibolite-facies mylonite and then overprinted by ductile shear (Upper Mont Mary unit, Western Alps). B) Pseudotachylyte vein cut through undeformed anorthositic host-rock and subsequently overprinted by ductile shear preserving an undeformed injection vein. (Nusfjord, Lofoten; Menegon et al., 2017)

continental crust instead then in the brittle upper crust (e.g. Camacho et al., 1995). Pseudotachylytes found in lower crustal rocks commonly show a close association with mylonites (e.g. Wenk and Weiss, 1982; Hobbs et al., 1986; Tagaki et al., 2000; Shimada et al., 2004; McNulty, 1995; Passchier, 1982; Lin et al., 2003). In the lower crust it is often observed that pseudotachylytes cut through pristine rocks and then localise ductile deformation (Fig. 1.2; e.g. Menegon et al., 2017; Hawemann et al., 2018). This behaviour can be cyclical, raising the question why brittle failure is still achieved once weak layers that can easily localise ductile flow are available. On the contrary, it is also commonly observed that pseudotachylyte veins are localised within previously existing mylonites (Fig. 1.2; e.g. White, 1996; Pennacchioni and Cesare, 1997). If the brittle transient is coeval with the host mylonite, pseudotachylytes can then in turn be overprinted by ductile shear (Fig. 1.2) under the same ambient conditions as the host mylonite. When this is the case, pseudotachylytes are very easily lost from the geological record (Kirkpatrick and Rowe, 2013). The observation of ductile-brittle-ductile deformation once again raises the question why a ductile shear zone should transiently experience seismic deformation (White, 2012). Possible interpretations that have been proposed to solve this conundrum are discussed in the next chapter.

1.2 Mechanisms for pseudotachylyte formation in the ductile field

Deep-seated pseudotachylytes are inferred to represent seismic events outside the classic seismogenic zone and the mechanisms by which they form is still a matter of dispute (White, 2012). We list and briefly discuss the most common explanation for associations of coeval pseudotachylyte and mylonite in the lower continental crust.

1.2.1 Downward propagation of seismic ruptures

Earthquake ruptures nucleated within the upper seismogenic crust can propagate downward into the underlying ductile crust (Tse and Rice, 1986). This process is a common explanation for deep crustal pseudotachylytes (Sibson, 1980; Lin et al., 2005; Moecher and Steltenpohl, 2009). Moecher and Steltenpohl (2009) proposed that mylonitised pseudotachylytes within granulite-facies orthogneiss require 10–20 km of downward propagation of seismic rupture. Fast strain rates during dynamic propagation would account for transient strengthening of weak ductile rocks. This process does not require long-term high-differential stresses in lower crustal rocks. Dynamic propagation of rupture is followed by subsequent slip to depth for which there is seismological support (Shaw and Wesnousky, 2008; Ide et al., 2011). Fault lubrication provided by the formation of a melt phase by frictional heating on the rupture surface (Di Toro et al., 2006) would also favour extensive deep-penetrating slip. Pseudotachylytes that originated at depths below the long-term brittle-ductile transition and were subsequently deformed in a ductile manner can thus be interpreted as field evidence for deep rupture extension, but this cannot explain earthquake hypocenters in the lower crust and high-stress creep associated with deep-seated pseudotachylytes.

1.2.2 Stress transfer from the seismogenic crust

Major seismic faulting in the upper crust can induce elevated stresses and creep rates below the brittle-ductile transition (Ellis and Stöckhert 2004a, 2004b). High-differential stresses induced by an earthquake can cause significant localised post-seismic creep (Campbell and Menegon, 2019) along the deep crustal continuation of the fault and a time-dependent deepening of the brittle-ductile transition near the tip of the fault. The downward deflection of the brittle-ductile transition zone with time after a large event predicted by numerical models (Ellis and Stöckhert 2004a, 2004b) is

confirmed by observations of aftershock distributions (Rolandone et al. , 2002). This process has been invoked for the nucleation of lower crustal earthquakes in the Woodroffe thrust in Central Australia (Hawemann et al., 2018; Wex et al., 2019) and is favoured by dry conditions that allows storing of high long-term differential stresses (Menegon et al., 2011; Fitz Gerald et al., 2006).

1.2.3 Ductile instabilities

Hobbs et al. (1986) proposed that pseudotachylytes could nucleate entirely within the ductile regime due to a ductile instability. Such instability can develop as result of extreme weakening due to a positive feedback between shear heating and viscosity, a process known as self-localising thermal runaway. Numerical models (e.g. Kaus and Podladchikov (2006), Kelemen and Hirth, 2007; Braeck and Podlachikov, 2007; John et al., 2009; Thielmann et al., 2015), seismological studies (Prieto et al., 2013; Prieto et al., 2017), and experiments (Ohuchi et al., 2017) have investigated thermal runaway instability within the lithospheric mantle. Few exhumed associations of coeval pseudotachylytes and mylonites have been interpreted as the result of ductile instabilities (in middle to lower crust: Hobbs et al., 1986; White, 1996, 2012; Stewart and Miranda, 2017). Thermal runaway requires a fine-grained shear zone as ductile precursor for pseudotachylyte development and high differential stresses on the order of 1 GPa for upper mantle rheology (e.g. Kelemen and Hirth, 2007). Such high stresses (and strain rates) could be reached if a shallower (brittle) earthquake loads deeper parts of the lithosphere where brittle failure is less likely to occur (Thielmann et al., 2015).

1.2.4 Other mechanisms

Other processes that could lead to coeval pseudotachylytes and mylonites can be (1) the presence of stiff bodies within the mylonites that act as stress risers locally nucleating earthquakes ruptures (e.g. Sibson, 1980) or (2) shear instabilities triggered by microscale cavitation during ductile flow (Verberne et al., 2018). Other mechanisms that have been proposed to explain deep earthquakes like dehydration embrittlement (Hacker et al., 2003) and transformational faulting (e.g. Green and Houston, 1995) are more relevant for mantle and subduction zones, although recent works (Shi et al., 2018; Incel et al., 2019) support the case for reaction-induced embrittlement of the lower continental crust.

1.3 Ambient conditions of formation of pseudotachylytes

Pseudotachylytes are the best indicator available for paleo-seismicity in exhumed rocks. Their association with high-grade rocks is direct evidence for major earthquakes in the deep crust and their association and mutual overprinting with mylonites is an evidence for the interplay between brittle and ductile deformation. However, in order to use pseudotachylytes as record for deep crustal earthquakes it has to be ascertained that they formed at lower crustal conditions and not at shallower crustal levels within exhumed lower crustal rocks. This requires a careful study of the stable mineral assemblage preserved in the pseudotachylytes to establish that they were developed under deep conditions, similar to peak metamorphic conditions in the surrounding rocks. In addition, to understand a relationship between what appears to be coeval pseudotachylytes and mylonites, one must demonstrate that pseudotachylytes were formed under the same conditions as the mylonites. This is a crucial point and it is not easy to do for natural pseudotachylytes. Pseudotachylytes are fine-grained rocks that are generally associated with a damage zone of intense brittle deformation. They represent perfect pathways for fluids and are more subject to alteration than the rocks in which they are hosted (Phillips et al., 2019). Even when they are not altered it is often difficult to determine their formation condition analysing their mineralogical content since pseudotachylytes are quenched melts whose minerals are not necessarily representative of the ambient conditions (Moecher and Brearley, 2004). Moreover, pseudotachylyte melts have generally a different chemical composition than their host rocks, because melting is never complete (Lin and Shimamoto, 1998), and they are also very chemically heterogeneous since they are quenched very rapidly before the melt can homogenise (Hawemann et al., 2018). Glass is almost never preserved and devitrification aggregates are often so fine-grained that they require very high-resolution analytical techniques to be studied. An equilibrium paragenesis can be achieved in pseudotachylytes if mylonitic deformation catalyses metamorphic reactions (Moecher and Steltenpohl, 2009; Leib et al., 2016; Menegon et al., 2017). Although deformation can erase the diagnostic features for the recognition of pseudotachylytes (Price et al., 2012), crystallisation of high-grade minerals during pseudotachylyte mylonitisation has been commonly used to constrain the condition at which a seismic event occurred (e.g. Moecher and Steltenpohl, 2009; Leib et al., 2016; Menegon et al., 2017).

Garnet is an important index mineral because it is stable over a large range of pressure and temperature conditions as well as bulk rock compositions, and thus its stability in pseudotachylytes is diagnostic of their depth of formation. Unfortunately garnet is also a refractory phase, in the sense that it re-equilibrates very slowly in response to changing external conditions (Hollister, 1969), and it requires a large overstepping of metamorphic reactions is required to provide the driving force necessary for porphyroblast nucleation and growth (Spear, 2017). Garnet is often present in lower crustal pseudotachylytes as cauliflower shape and it has commonly been observed that the presence of tiny host-rock garnet fragments in the pseudotachylyte melts is a nucleation seed for growth of cauliflower garnets (Altenberger et al., 2013; Pittarello et al., 2012; Lund and Austrheim, 2003; Steltenpohl et al., 2006; Pittarello et al., 2015; Hawemann et al., 2018). It has also been commonly observed that garnet clasts are seldomly preserved within pseudotachylytes and that host-rock garnet is commonly extremely fragmented close to pseudotachylyte veins (Austrheim et al., 1996; Austrheim et al., 2017).

1.4 Regional geology: Mont Mary nappe

Chapter 2, 3, and 4 of this thesis concern the study of pseudotachylytes hosted in amphibolite-grade mylonites/ultramylonites of the Upper Unit of the Mont Mary nappe (Western Alps). The Mont Mary nappe is located in the Western Italian Alps; North of the Aosta Valley, between the Valpelline to the West and the Valtournenche to the East. It is a continental basement nappe, part of the Dent Blanche Tectonic System (Manzotti et al. 2014a, b), the largest continental klippe exposed above the oceanic domains of the Western Alps (Piedmont ophiolites) (Fig. 1.3A). It is subdivided into two lithological units called the Upper and Lower units (Canepa et al., 1990; Dal Piaz et al., 2010) and it is separated from the Dent Blanche s.s. nappe by a low-grade Alpine shear zone called the Roisan-Cignana Shear Zone (Manzotti et al., 2014b). The Mont Mary Upper and Lower units can be related to the two lithological units in which is subdivided the Dent Blanche s.s. nappe, respectively the Valpelline series and the Arolla series (Argand, 1906). The first represent slices of the late-Palaeozoic lower crust, the second slices of upper crust made up by Permian granitoids (Compagnoni et al. 1977a; Dal Piaz, 1993). The Upper Unit of the Mont Mary nappe consists mostly of paragneisses that preserve pre-Alpine high-temperature assemblages (Canepa et al., 1990). Pre-Alpine peak

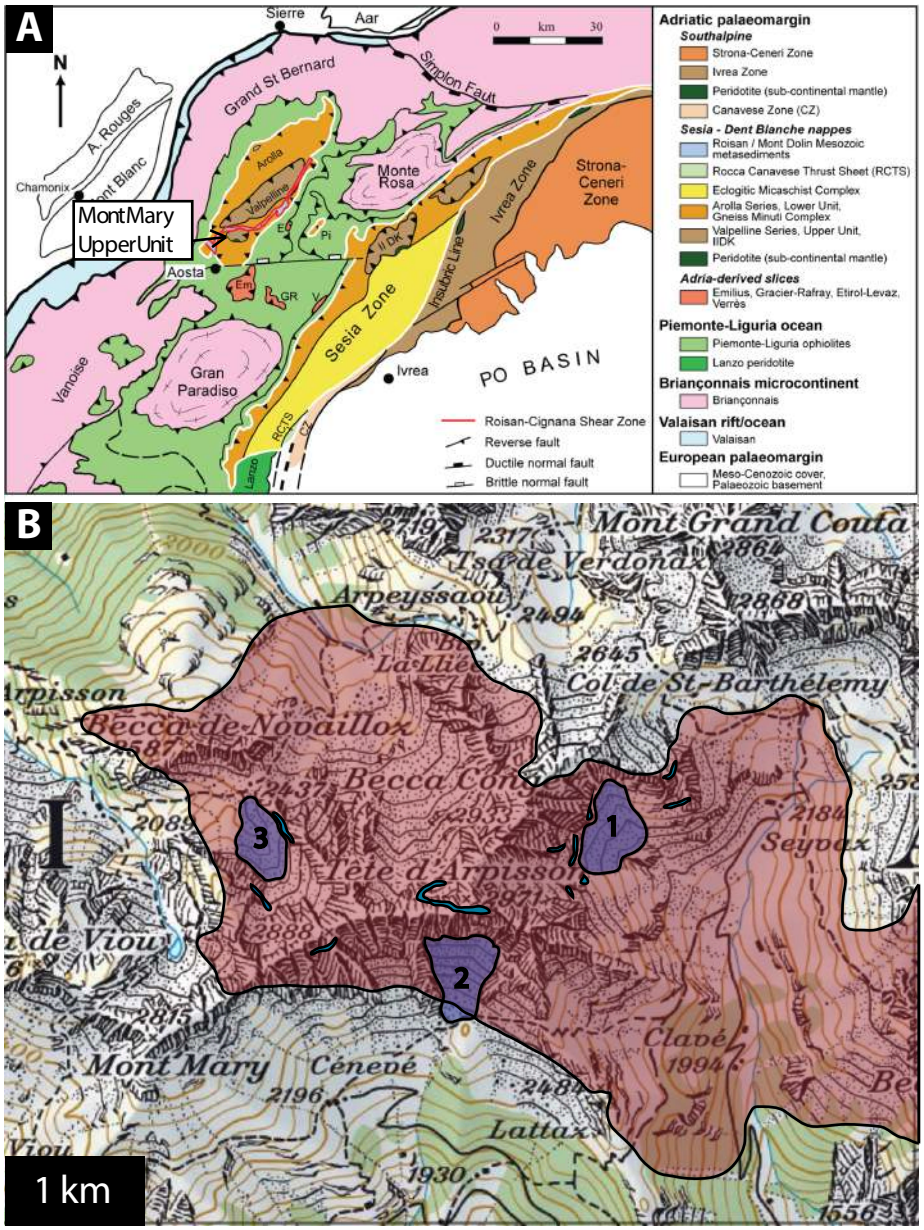

Figure 1. 3 A. Simplified tectonic map of the north-western part of the Western Alps (from Manzotti et al., 2014c, modified after Le Bayon and Ballèvre, 2006). B. Map of the study area. Upper Mont Mary unit in red, outcrops of pre-Alpine mylonites in turquoise, sampling areas in violet. Topographic base is from the website www.geo.admin.ch of the Swiss Federal Office of Topography swisstopo. Lithological boundaries from the Carta Geologica d'Italia, Foglio 070 Monte Cervino and Foglio 091 Chatillon.

metamorphism is of Permian age and pertain to the upper amphibolite to granulite facies conditions (Zucali et al. 2011; Manzotti and Zucali, 2012). In the Upper Mont Mary nappe, Alpine deformation, characterised by a low temperature and intermediate pressure condition (blueschist–greenschist facies; Roda and Zucali, 2008) is localised in shear zones at the boundary units, while the bulk of the unit has mostly preserved the granulitic to amphibolitic pre-Alpine imprint. Peak conditions of the pre-Alpine metamorphism are related to Permo-mesozoic lithospheric extension responsible for asthenosphere upwelling causing high temperature metamorphism at medium pressure with a high

geothermal gradient of 35–40 °C km^{-1} (Manzotti and Zucali, 2012). A comprehensive review and synthesis of the tectonometamorphic evolution of the Austroalpine units of the Western Alps can be found in Manzotti et al. (2014a).

The upper tectonic unit of the Mont Mary nappe consists of upper amphibolite to granulite paragneisses, metabasites and marbles (Canepa et al., 1990). The pre-Alpine coarse-grained paragneisses ("kinzigites" Auct.) consist of quartz + garnet + sillimanite + biotite + plagioclase + K-feldspar + ilmenite + graphite ± cordierite. These rocks host a few-meters-thick horizon of amphibolite-facies mylonite/ultramylonite subparallel to the main foliation and to the Mont Mary unit boundaries (Pennacchioni and Cesare, 1997; Dal Piaz et al., 2010). The mylonitic assemblage is quartz + garnet + sillimanite + biotite + plagioclase + muscovite + ilmenite + graphite. These mylonites show, in comparison with the protolith: consumption of K-feldspar, development of muscovite, growth of new small garnet, recrystallization of biotite, and persistence of sillimanite. The pressure-temperature conditions of mylonitization were estimated at 545 ± 35 °C and 0.35 ± 0.1 GPa (Pennacchioni and Cesare, 1997). This points to a pre-Alpine age of deformation, since amphibolite facies metamorphic conditions were never reached during the Alpine orogeny in the Western Alps. Mylonitization was referred to the activity of lithospheric detachments during Permian extensional tectonics that affected the Hercynian continental crust (Pennacchioni and Cesare, 1997). The latest metamorphic stage of the pre-Alpine evolution is associated with a local static mineral-chemical re-equilibration under greenschist facies conditions, characterised by substitution of sillimanite by chlorite and crystallisation of epidote and muscovite.

The samples studied in chapters 2, 3, and 4 of this thesis are loose cobbles and boulders collected from scree deposits at the bottom of the east face of Becca Conge, and south and north faces of Tête d'Arpisson (Fig. 1.3). Outcrops displaying the mylonitic horizon are commonly located on inaccessible cliffs, and where locally reachable are heavily weathered. No detailed field study of pseudotachylytes geometry on a scale larger than that of hand samples was possible.

1.5 Aim and outline of the thesis

The topic of lower crustal earthquakes has received much attention in recent years (Shi et al., 2018; Incel et al., 2019; Petley-Ragan et al., 2018, 2019; Hawemann et al., 2018, 2019; Wex et al., 2018, 2019; Campbell and Menegon, 2019; Menegon et al., 2017; Stewart and Miranda, 2017). With this thesis we aim to aid to this discussion by providing original and meaningful contributions to the

understanding of the mechanisms involved in the interplay between seismic deformation and ductile flow at depth. The approach applied in this thesis consists of careful field analysis and collection of representative samples, followed by thorough microstructural/petrologic analysis of selected samples and development of models constrained by field and lab study.

This thesis is subdivided into four main chapters, all first-authored:

Chapter 2 describes in detail the microstructures of the pseudotachylyte/mylonite association of the Mont Mary nappe of the Western Alps. We propose an interpretation for the observed microstructural evolution of the ultramylonite that lead to pseudotachylyte formation and we show the results of the first numerical model for thermal runaway in a quart rich crust. A slightly different version of this chapter has been submitted for publication to the journal Earth and Planetary Science Letter.

Chapter 3 tackles the topic of garnet fragmentation associated to pseudotachylytes and garnet preferential disappearance within frictional melts, observed in the Mont Mary samples and by other authors before. We propose a model to explain garnet behaviour during coseismic slip and frictional heating. This chapter, in a slightly different version, was published in the journal Geology (Papa et al., 2018).

Chapter 4 reports the results (mechanical and microstructural) of rotary shear experiments carried on to simulate the formation of Mont Mary pseudotachylytes and to compare the lab microstructures to the natural ones, especially for what concerns garnet behaviour.

Chapter 5 is a preliminary study of pseudotachylytes and pseudotachylyte/mylonite associations from the Calabrian lower crust, where we present microstructural and petrological evidence for repeated cycles of ductile and seismic deformation in the lower crust.

2 High-stress creep preceding coseismic rupturing in amphibolite-facies ultramylonites

Simone Papa[1], Giorgio Pennacchioni[1], Luca Menegon[2,†], Marcel Thielmann[3]

Abstract

Coeval pseudotachylytes (solidified frictional melts) and mylonites are generally regarded as the geological record of transient seismic events during dominant ductile flow. Self-localising thermal runaway has been proposed as a model to explain the pseudotachylyte-mylonite association. In the Mont Mary unit (Western Alps), pseudotachylyte fault veins exploited the amphibolite-facies (ca. 550 °C; 0.35 GPa) ultramylonitic foliation in paragneisses and were locally overprinted by ductile shearing, therefore possibly as a result of thermal runaway ductile instabilities. The microstructure of the most strongly deformed quartz in ultramylonite and of quartz clasts in the pseudotachylyte is investigated here to find possible evidence for the occurrence of ductile instability. Quartz aggregates show an evolution under constant temperature to ultrafine-grained recrystallised grain size (2.5 μm), reflecting high differential stresses (200 MPa) and high strain rates (), along very localised foliation-parallel layers. In these ultrafine aggregates viscous grain boundary sliding became dominant and promoted cavitation leading to disaggregation of quartz aggregates and precipitation of oriented biotite in pore spaces. The strain rate-limiting process was aseismic fluid-assisted precipitation of biotite. Calibrated numerical models were performed to investigate the potential occurrence of ductile thermal runaway instability for pure quartz layers at the deformation conditions of the Mont Mary ultramylonites. These models predict a switch from stable flow to thermal runaway at background strain rates faster than 10^{-9} s^{-1} for critical stresses that are comparable to the brittle strength of rocks. However, there is no evidence in the preserved microstructures that such fast strain rates were ever reached during mylonitic creep in the Mont

[1] Department of Geosciences, University of Padova, Via Gradenigo 6, I-35131 Padua, Italy
[2] School of Geography, Earth and Environmental Sciences, University of Plymouth, Drake Circus, PL48AA Plymouth, UK
[3] Bayerisches Geoinstitut, University of Bayreuth, Universitätstraße 30, 95440 Bayreuth, Germany
[†] now at: The Njord Centre, Department of Geosciences, University of Oslo, Postbox 1048, Blindern, 0316 Oslo, Norway

Mary samples. Thus, the microstructural record in the Mont Mary is better explained by transitory events at high strain rates induced by a seismogenic source in the upper crust, causing a transient downward deflection of the brittle/ductile transition.

2.1 Introduction

Coeval pseudotachylytes and mylonites in exhumed mid to lower crustal rocks records transient seismic slip during ductile flow (e.g. Sibson, 1980). Different models have been proposed to explain this association of fault rocks. Earthquake ruptures nucleating at the base of the seismogenic crust (c.a 15 km depth) can propagate downward into the underlying ductile crust (Tse and Rice, 1986) producing pseudotachylytes that are then overprinted by mylonitization during post- and interseismic creep. This process was proposed by Lin et al. (2005) for the mylonitic pseudotachylytes along the Woodroffe Thrust (Central Australia). Numerical models show that seismic faulting in the upper crust can cause a transient downward deflection of the brittle-ductile transition and a zone of increased strain rate below the fault tip (Ellis & Stöckhert, 2004). This can explain transient high stresses in the middle to lower crust resulting in aftershock seismicity in the otherwise ductilely flowing crust (e.g. Hawemann et al., 2018; Jamtveit et al., 2018).

The above process assumes a distal trigger for the seismicity in the middle and lower crust. Where deep-seated pseudotachylytes are not associated with mylonites, a local trigger for seismicity may be interpreted to represent the release of high long-term differential stresses accumulated in dry metastable rocks due to brittle fracturing (e.g. Scambelluri et al., 2017).

Hobbs et al. (1986) proposed that pseudotachylytes could nucleate during high temperature flow due to ductile instabilities. Such instabilities develop as a result of extreme weakening due to the positive feedback between shear heating and viscosity - a process known as self-localizing thermal runaway. Numerical models (e.g. Kelemen and Hirth, 2007; Braeck and Podlachikov, 2007; Thielmann et al., 2015), seismological studies (Prieto et al., 2013), and experiments (Ohuchi et al., 2017) have investigated thermal runaway instabilities within the lithospheric mantle and the lower crust (John et al., 2009). Few exhumed pseudotachylyte/mylonite associations have been interpreted to have resulted from ductile instabilities (in middle to lower crust: Hobbs et al., 1986; White, 1996, 2012; Stewart and Miranda, 2017). Stewart and Miranda (2017) interpreted grain

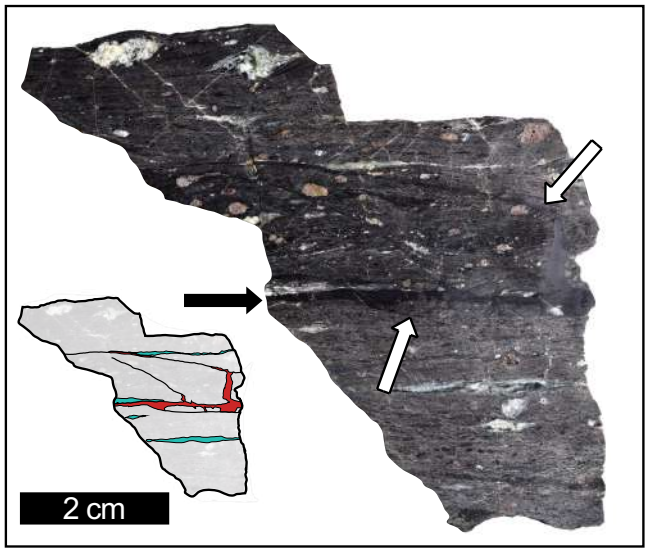

Figure 2.1 Polished slab of a loose block of pseudotachylyte-hosting amphibolitic ultramylonite (sample MMS42). The main pseudotachylyte fault vein, indicated by the black arrow, is parallel to the mylonitic foliation and located at the boundary of a quartz-rich layer in the host mylonite. The white arrows indicate melt-bearing contractional ramps part of a 'sidewall ripout' structure, typically associated with pseudotachylytes (Swanson, 1992). In the sketch on the left, the melt is represented in red and quartz-feldspar-rich layers close to the main vein in turquoise.

boundary sliding (GBS) traits of quartz aggregates as the ductile precursor to pseudotachylyte development. Nevertheless, unambiguous microstructural evidence for the process of ductile instability is missing.

The pseudotachylytes of the Mont Mary nappe (Western Alps: Pennacchioni and Cesare, 1997) are invariably hosted within amphibolite-facies ultramylonites in paragneiss. The pseudotachylyte fault veins are sub-parallel to the ultramylonitic foliation, and were overprinted by ductile shear. These pseudotachylytes therefore represent a candidate for recording ductile instabilities. We used electron backscattered diffraction (EBSD) to investigate the quartz microstructure and crystallographic preferred orientations (CPO) of the ultramylonite host of pseudotachylyte, and of clasts within pseudotachylyte in order to infer the deformation mechanisms preceding frictional melting. The aim of this study is to understand the rheological evolution of the ultramylonite and to detect signs of localized accelerated creep rate that could eventually have evolved into pseudotachylytes.

2.2 Geologic setting and sample description

The upper tectonic unit of the Mont Mary nappe consists of upper amphibolite to granulite facies paragneisses, metabasites and marbles (Canepa et al., 1990). The well-preserved dominant deformational and metamorphic imprint is pre-Alpine (Permian: Manzotti et al., 2014 and references therein) and Alpine greenschist-facies retrogression is localized within mylonitic shear zones at the unit boundary.

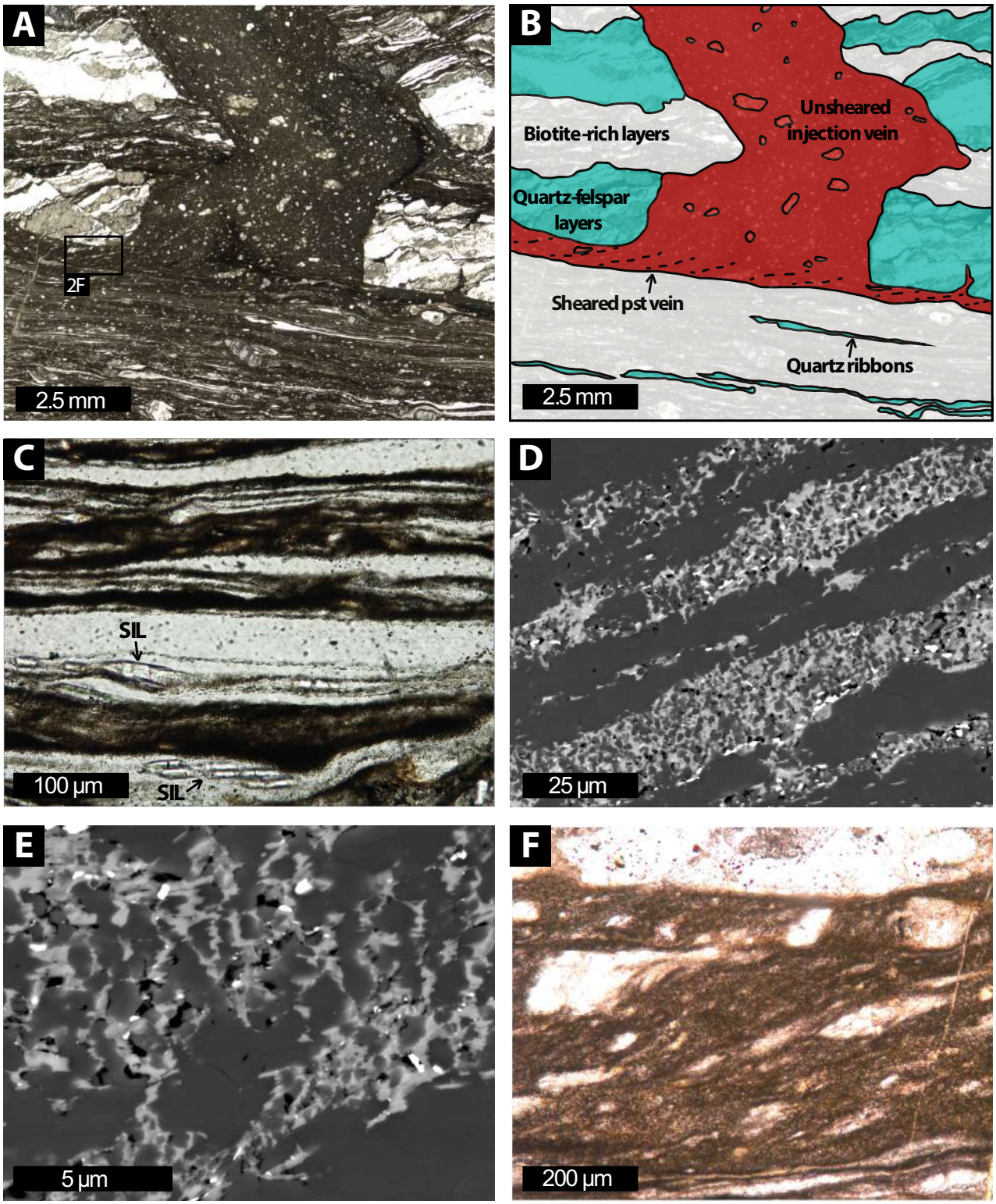

The pre-Alpine coarse-grained paragneisses consist of quartz + garnet + sillimanite + biotite + plagioclase + K-feldspar + ilmenite + graphite ± cordierite. These paragneisses host a few-meters-thick horizon of amphibolite-facies mylonite/ultramylonite subparallel to the main foliation and to the Mont Mary unit boundaries. These mylonites show, in comparison with the protolith: breakdown of K-feldspar, development of muscovite, growth of new small garnet and

Figure 2. 2 A) Plane-polarised light image of an array of pseudotachylyte fault vein and injection veins. The pseudotachylyte main vein, parallel to the foliation, was overprinted by ductile shear as shown by an oblique, dextral foliation. Injection veins, intruding at a high angle the host-rock foliation, do not show any ductile overprint (enlargement of the area enclosed by the black rectangle in 2F). Note the alternation in the host mylonite of quartz-feldspar rich layers and darker biotite rich layers. In the upper part of the image, the microstructure is characterised by pervasive cataclastic deformation, mainly represented by shear fractures subparallel to the main injection vein. B) Sketch showing the most relevant features in (A). C) Detail of a quartz-rich layer, showing an alternation between quartz ribbons and turbid, brownish layers not resolvable with polarized light microscopy. Note the abundance of small, prismatic porphyroclasts of sillimanite (indicated by black arrows). Plane-polarised light. D) SEM-backscattered image of the same kind of microstructure shown in (C). Turbid layers consist of quartz grains (dark grey) in a matrix mainly composed of biotite (light grey) and small acicular ilmenite crystals (white). (E) Detail of a quartz + biotite layer showing the typical microstructure of columnar, few-microns-thick quartz aggregates, separated by thin vertical biotite layers in which biotite lamellae grew with their long axes parallel to the foliation (SEM-backscattered image). (F) Blow-up of the pseudotachylyte vein of Fig. 2A, clearly showing the dextral oblique foliation.

recrystallization of biotite. The pressure-temperature conditions of mylonitization were estimated at 545 $\pm$ 35 °C and 0.35 $\pm$ 0.1 GPa (Pennacchioni and Cesare, 1997). Mylonitization was linked to the activity of lithospheric detachments during Permian extensional tectonics that affected the Hercynian continental crust (Pennacchioni and Cesare, 1997).

Pseudotachylyte veins occur within the ultramylonites as thin (commonly a few mm thick) fault and injection veins (up to a few cm thick) subparallel and crosscutting at a high angle the host foliation, respectively (Fig. 2.1). The pseudotachylyte fault veins form isolated structures, subparallel arrays and are locally arranged in more complex geometries with interacting fault and injection veins, similar to sidewall ripouts, on both sides of the slipping surface (Fig. 2.1; Swanson, 1992). Pseudotachylytes also commonly mark an angular discordance in the host foliation associated with block rotation during coseismic slip. Pennacchioni and Cesare (1997) and Papa et al. (2018) inferred that the pseudotachylytes were coeval with the mylonitic deformation because of: (i) the presence of local ductile shearing of pseudotachylytes showing the same kinematics as the host ultramylonite (Fig. 2.2F); and (ii) the stability of amphibolite facies minerals (sillimanite and An_{35}-plagioclase clasts) together with the incipient growth of new dendritic garnet coronas on the rare garnet clasts. Pseudotachylytes have only been found within ultramylonites.

The paragneiss ultramylonites display a sub-centimetric layering with alternating quartz ribbons, and quartz-feldspar and biotite-rich layers (Fig. 2.2A-B). Plagioclase, garnet and sillimanite occur as rounded to sigmoidal porphyroclasts. A detailed description of the mylonitic microstructure and mineral assemblage can be found in Pennacchioni and Cesare (1997) and Pennacchioni et al. (2001). A distinguishing microstructure of the ultramylonites is the alternating thin layers, few tens of

micrometers thick, of finely recrystallized quartz ribbons and optically irresolvable dark layers in the most high-strain domains (Fig. 2.2C). In backscattered SEM images, these dark layers appear to consist of a fine-grained mixture of quartz and biotite that show gradational relationships with the adjacent recrystallised quartz ribbons (Fig. 2.2D). The evolution of the quartz microstructure and CPO in ultramylonites and of clasts of ultramylonitic quartz within the pseudotachylyte is the focus of the present study.

2.3 Methods

2.3.1 Sample preparation and data processing

Thin sections of ultramylonite were prepared from rock chips cut parallel to the stretching lineation and perpendicular to the (ultra)mylonitic foliation (XZ plane of finite strain ellipsoid). The thin sections were SYTON-polished and carbon coated.

Electron backscattered diffraction (EBSD) analyses were carried out on a JEOL 7001 FEG SEM equipped with a NordLys Max EBSD detector (AZtec acquisition software, Oxford Instruments) and on a JEOL 6610 tungsten filament SEM equipped with a NordLys Nano detector at the Electron Microscopy Centre of the University of Plymouth. EBSD patterns were acquired on rectangular grids with step sizes of 0.3, 0.35 and 0.4 µm. Working conditions during acquisition of EBSD patterns were 20 kV accelerating voltage, 70° sample tilt, high vacuum, and a working distance between 17 and 23 mm.

Noise reduction was performed using CHANNEL5 software of HKL Technology, Oxford Instruments, by removing wild spikes and replacing zero-solution points with the orientation of nearest neighbours starting from eight neighbours down to five. Critical misorientation for the distinction between subgrains and grain boundaries was set at 10°. The pole figures are plotted as equal area, lower hemisphere projections oriented with the general shear zone kinematics reference system (X = stretching lineation; Z = pole to foliation). Misorientation axes have been determined in sample and crystal coordinates for ranges of misorientation angles of 2-10° and 10-45°. The threshold of 10° was chosen to separate subgrain boundaries from grain boundaries, and the upper limit of 45° to avoid the contribution of Dauphiné twins in the misorientation axes distribution of grain

boundaries. The misorientation axis distributions are plotted in crystal coordinates as equal area, lower hemisphere projections. Contoured projections have constant contouring parameters (halfwidth = 10°).

2.3.2 Grain size analysis

To avoid any contribution from Dauphiné twin boundaries (misorientation of 60° around the [c] axis) grains were calculated from EBSD data using the point group 622 and transforming the grain mean orientation back into trigonal point group 321, as in Kilian and Heilbronner (2017), using the MTEX toolbox by Ralf Hielscher (https://mtex-toolbox.github.io/). Grain size was calculated as diameter of the area equivalent circle. The minimum cut-off area was set to 10 pixels, which means that, depending on the map acquisition step size, only grains of a size > 1.07 μm (0.3 μm step size), >1.25 μm (0.35 μm), and 1.43 μm (0.4 μm) were considered. The number-weighted distribution of the logarithm of grain sizes is presented as a histogram, for which the arithmetic mean was determined. For piezometric estimates, according to Cross et al. (2017), the root mean square (RMS) of the grain size distribution is used. The population of recrystallized grains is segmented in 2 classes of high- and low-strained grains by calculating a threshold grain orientation spread (GOS) value, following the method of Cross et al. (2017). The arithmetic mean of grain size distribution of low-GOS grains is considered as the average recrystallized grain size. This method was calibrated using experimentally deformed samples of Black Hills Quartzite, where large, non-recrystallized grains, with a high degree of intracrystalline lattice distortion are quite distinguished from small recrystallized grains. In the case of a natural mylonite with a prolonged deformation history, it is not so easy to separate old recrystallised grains from those related to the last recrystallization event. Nonetheless, we followed the procedure in order to obtain representative and reproducible results, but we are aware of the limitations this method involves. Considering only high-GOS grains, and setting the critical misorientation to 2°, we used the same procedure to calculate subgrain size.

2.4 Results

The EBSD analysis was conducted on different thin sections of the pseudotachylyte-hosting ultramylonite MMS42 (Fig. 2.1) for a total of 9 EBSD maps (Table S2). The analysis was performed

on quartz aggregates of the ultramylonite and of clasts within the pseudotachylyte vein. The maps presented herein and in the supplementary material are therefore representative of a larger dataset and the reported textural information is supported by a robust database.

In the ultramylonite, the most strongly deformed domains, displaying a fine alternation of quartz ribbons and mixed quartz + biotite layers, were selected. We have investigated both recrystallized ribbons not immediately adjacent to pseudotachylyte and unaffected by the (coseismic) cataclastic deformation, and nearby the pseudotachylyte where the quartz is overprinted by fracturing. In the pseudotachylyte, we have analyzed only clasts of recrystallized quartz unaffected by later ductile deformation. These clasts are embedded in a pristine, not foliated pseudotachylyte matrix; they are generally angular, with sharp boundaries and can be distinguished from elongated quartz clasts in foliated pseudotachylytes that have experienced later ductile deformation.

2.4.1 Microstructures and CPO of quartz in the ultramylonite

Monomineralic, mm-thick quartz layers along the mylonitic foliation range from monocrystalline ribbons to dynamically recrystallized aggregates (Fig. 2.3). In recrystallized ribbons, the grain size is heterogeneous and varies from 1 μm to as large as ca. 30 μm (Fig. 4C). Using the method of Cross et al. (2017), the recrystallized grain population was segmented in 2 classes: i) high aspect ratio, larger grains, elongated slightly oblique to the ribbon boundary, with a higher degree of internal distortion (*quartz$_1$*); and (ii) smaller, equant, almost strain-free grains (*quartz$_2$*). *Quartz$_1$* includes abundant subgrains having a similar size distribution as *quartz$_2$* grains (Fig. 4D). The average grain size of *quartz$_2$* in recrystallized ribbons is 4-5 μm (Fig. 2.4C, Table S2). *Quartz$_2$* has a heterogeneous spatial distribution and preferentially occurs at the ribbon boundary adjacent to the mixed quartz + biotite layers. In the recrystallized quartz ribbons, grains with grain size < 5 μm form on average less than 15% of the cross-sectional area (Fig. S4).

The recrystallized quartz displays a bulk [c]-axis CPO characterized by a short girdle centered on the Y axis, and nearly orthogonal to the foliation, with either 2 maxima symmetrically developed aside Y or a single asymmetric maximum (Fig. 2.3B; Fig. 2.5C). For *quartz$_1$* and *quartz$_2$*, no significant change in pole figure is observed although a slight weakening of the CPO is observed in the *quartz$_2$* (Fig. 2.4B). Misorientation axis distribution in crystal coordinates for both low angle (subgrain)

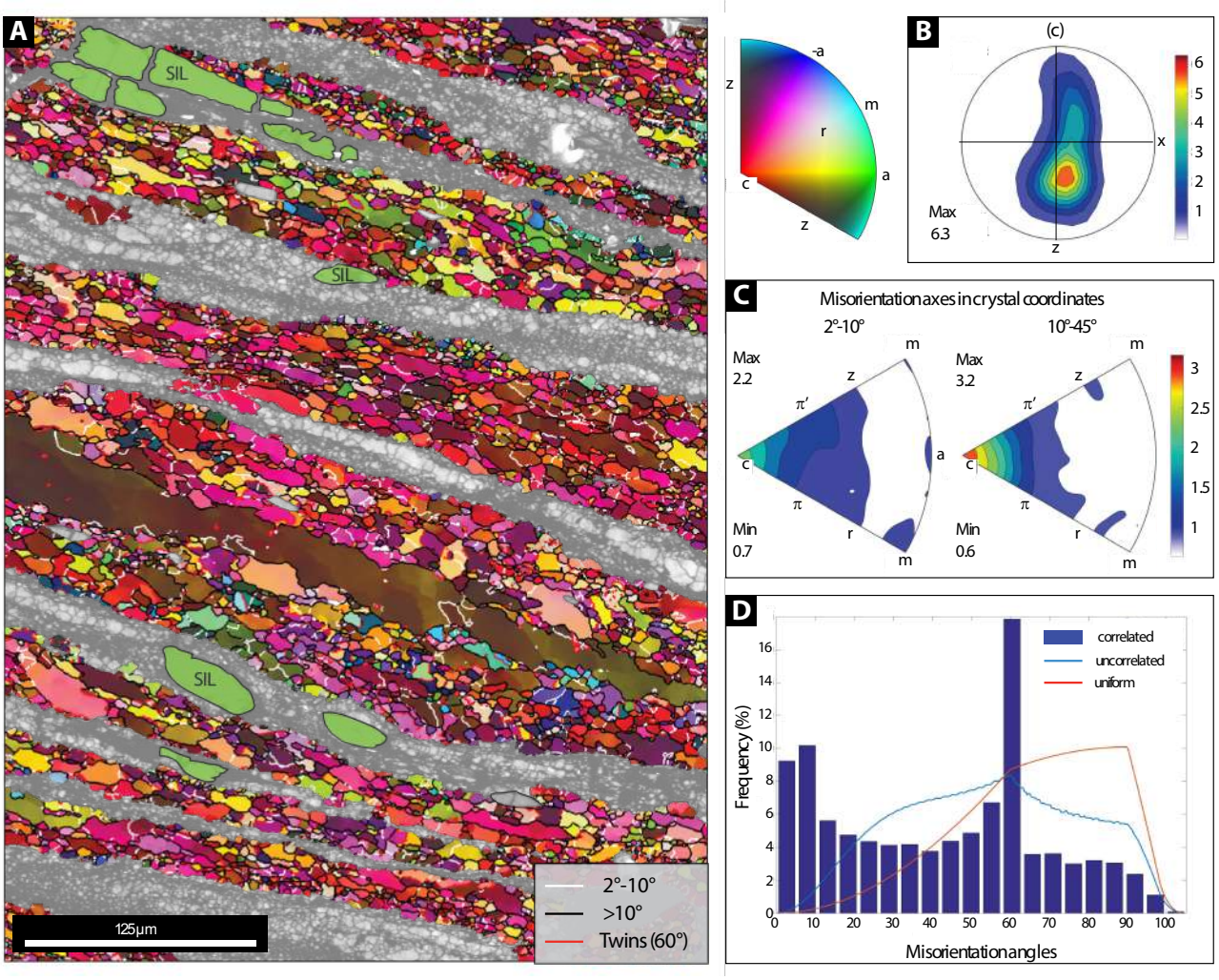

Figure 2. 3 EBSD analysis of quartz ribbons of the host mylonite. The trace of the mylonitic foliation is horizontal. A) Inverse pole figure map, colour coded with respect to the Y direction, of the selected subset consisting of recrystallised, non-disaggregated quartz ribbons. Background band contrast image shows layers of partially disaggregated quartz and biotite (black), rich of sillimanite clasts (coloured in green). B) Contoured pole figure for the (c)-axis. C) Misorientation axis distribution in crystal coordinates for subgrains (2-10°) and grain boundaries (10-45°). Max and min are expressed as multiples of the uniform distribution (m.u.d.). D) Misorientation angle distributions for correlated and uncorrelated misorientations. The red line represents the theoretical random distribution for the point group 321.

boundaries (2-10°) and high angle (grain) boundaries (10-45°) shows a strong maximum parallel to the [c]-axis (Fig. 2.3C). The distribution of uncorrelated misorientation angles shows higher frequencies for angles < 60° with respect to the random distribution, while for correlated ones higher frequencies are for angles of 60° (Dauphinè twins) and < 10° (subgrains) (Fig. 2.3D).

Aggregates of *quartz₂* at the boundaries of recrystallized ribbons transitional to mixed quartz + biotite layers are commonly spatially associated with sillimanite porphyroclasts (Fig. 2.3A; Fig. 2.5A). The CPO of these aggregates is similar in type as the one in the ribbon center but significantly weaker (Subset B in Fig. 2.5C). The misorientation axis distribution also shows a relatively weaker maximum

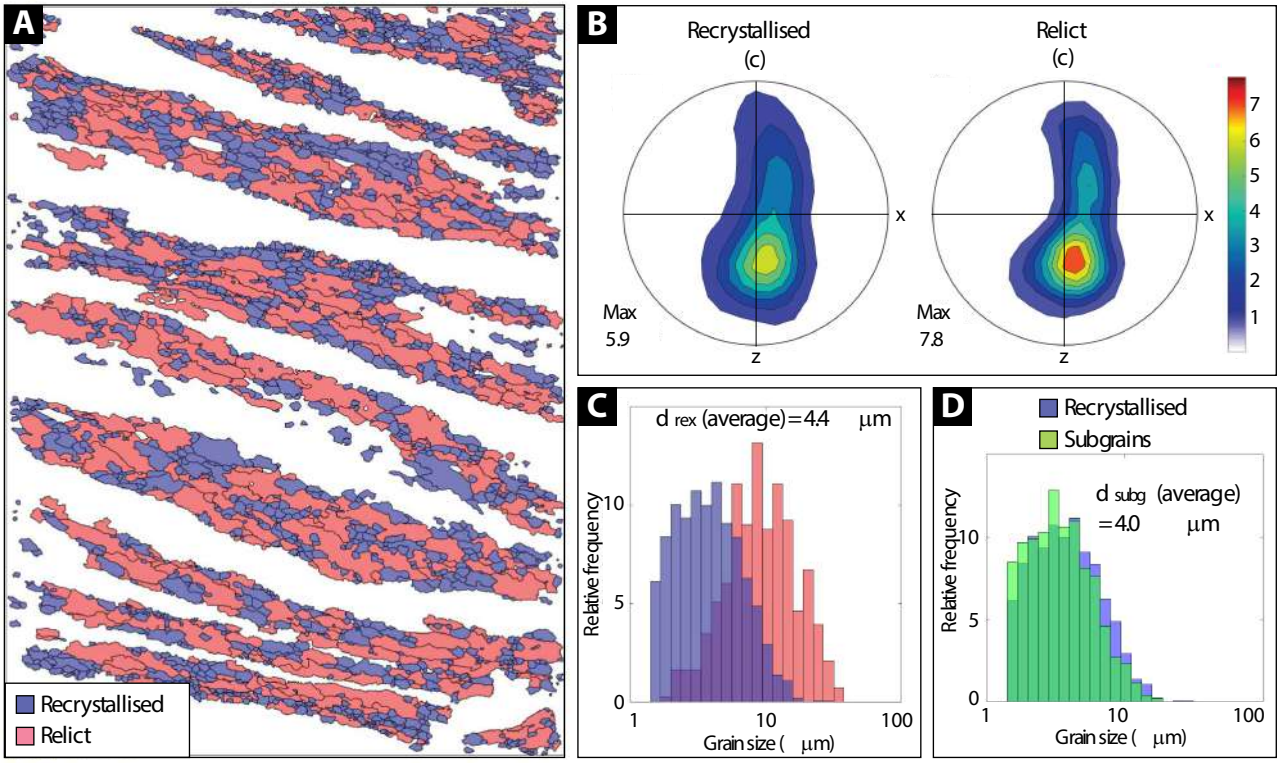

Figure 2. 4 A) GOS-separated recrystallised and relict grains for the map shown in Fig. 3A. Border grains have been removed and grains have been calculated considering a hexagonal symmetry to discard twin boundaries. B) (c)-axis contoured pole figure for recrystallised (quartz$_2$) and relict grains (quartz$_1$). Max and min expressed as multiples of the uniform distribution (m.u.d.). C) Grain size distribution for recrystallised (quartz$_2$) and relict grains (quartz$_1$). D) Grain size distribution for recrystallised grains (quartz$_2$) and subgrains.

parallel to [c] and an increased dispersion (Subset B in Fig. 2.5C). Distribution of uncorrelated misorientation angles at the ribbon periphery is close to a random distribution (Subset B in Fig. 2.5C). Finely recrystallised *quartz$_2$* grains dominate the microstructure at the ribbon boundary: the average grain size is smaller than 3 µm and most grains are smaller than 10 µm (Fig. 2.5G). The few *quartz$_1$* grains are smaller than inside the ribbons and contain subgrains of similar grain size of *quartz$_2$* (Fig. 2.5E).

The aggregates of dominant *quartz$_2$* at the ribbon boundary display common four-grain junctions and aligned, straight grain boundaries. Locally tiny cavities between grains are filled by a second phase, non-indexed in EBSD maps (Fig. 2.5E). Towards the mixed quartz + biotite layer, the *quartz$_2$* aggregate is locally disrupted, along the grain boundaries nearly orthogonal to the ribbon boundary, to form single-grain-thick columns separated by biotite preferentially orientated with the basal planes orthogonal to the quartz columns and subparallel to the foliation (Fig. 2.2E; Fig. 2.5D). This microstructure is transitional to mixed quartz + biotite layers where small (< 2.5 µm in diameter) strain-free quartz grains occur isolated within a biotite matrix (Fig. 2.5D).

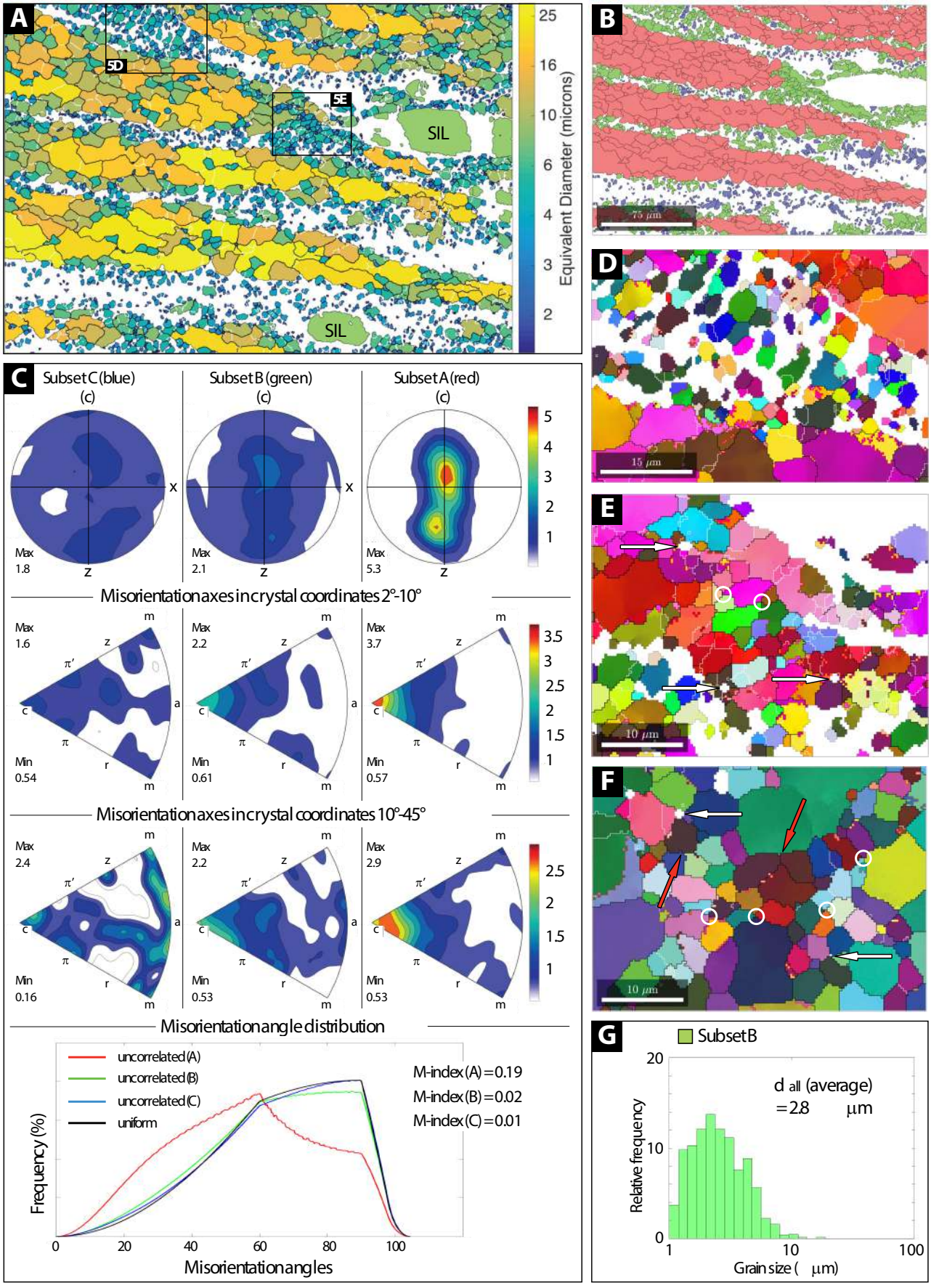
A
5D
5E
SIL
SIL
25
16
10
6
4
3
2
Equivalent Diameter (microns)
B
75 μm
C
Subset C (blue)
(c)
Subset B (green)
(c)
Subset A (red)
(c)
Max 1.8
Max 2.1
Max 5.3
Misorientation axes in crystal coordinates 2°-10°
Max 1.6
Min 0.54
Max 2.2
Min 0.61
Max 3.7
Min 0.57
Misorientation axes in crystal coordinates 10°-45°
Max 2.4
Min 0.16
Max 2.2
Min 0.53
Max 2.9
Min 0.53
Misorientation angle distribution
uncorrelated (A)
uncorrelated (B)
uncorrelated (C)
uniform
M-index (A) = 0.19
M-index (B) = 0.02
M-index (C) = 0.01
Frequency (%)
Misorientation angles
D
15 μm
E
10 μm
F
10 μm
G
Subset B
d all (average) = 2.8 μm
Relative frequency
Grain size (μm)

Figure 2. 5 EBSD analysis of quartz ribbons of the host mylonite. The trace of the mylonitic foliation is horizontal. A) EBSD maps of quartz grains colour coded according to grain size (diameter of the equivalent circle). B) Subsets of (A) analysed in (C). Subset A (red) consists of recrystallised, non-disaggregated quartz ribbons; subset C (blue) consists of quartz grains or aggregates of grains completely detached from the host ribbons and embedded in the biotite matrix. Subset B (green) is transitional between the two. C) (c)-axis contoured pole figures, misorientation axes distribution, and misorientation angle distribution for the subsets in (B). D) Selected area of (A) showing an incipient mixed layer of quartz and biotite between two quartz ribbons. Opening and precipitation of new biotite preferentially along planes perpendicular to the ribbon elongation forms the typical columnar quartz aggregates described in the text. E) Detail of a fine-recrystallised area at ribbon boundary, showing quadruple junctions (white circles) and interstitial biotite grains (not indexed in EBSD maps) along grain boundaries and at grains junctions (white arrows). Location of this area is indicated in (A). F) Detail of a completely recrystallised area in a quartz clast within pseudotachylyte (see figure S3). Four-grain junctions are common and associated with straight aligned grain boundaries (white circles and red arrows). Recrystallised grains are small and devoid of subgrains. Locally tiny biotite (non-indexed points) is found at four-grain junctions (white arrows). (D), (E), and (F) are inverse pole figures maps colour coded with respect to the Y direction. Boundaries are colour coded like in Fig. 3A. G) Grain size distribution for subset B.

The transition through the partially disaggregated columnar quartz to the mixed layer is associated with the progressive weakening of the "parent" CPO of the *quartz₂* at the ribbon boundary, ending up in almost random CPO and almost random distribution of uncorrelated misorientation angles (Subset C in Fig. 2.5C). Subgrain and grain boundaries show an increased dispersion of misorientation axis (Subset C in Fig. 2.5C).

The above described quartz ribbons are mostly unaffected by coseismic cataclastic deformation and only locally they are sharply crosscut by brittle fractures discontinuously decorated by a very thin layer of pseudotachylyte/ultracataclasite. When adjacent to pseudotachylyte (Fig. S1), the quartz ribbons are offset by optically sharp micro-shear zones that, in EBSD maps, consist of aggregates, a few tens of μm thick, of fine (2-3 μm grain size) strain-free quartz grains. These fine aggregates show a host-controlled CPO consistently weakened with respect to the quartz ribbons, and are very similar to the coseismic ultrafine dynamic recrystallized quartz described in Bestmann et al. (2011) and to quartz microstructures observed in 'kick and cook' experiments by Trepmann et al. (2007). In at least one of these bands we observe a clear maximum of the misorientation axes of subgrain boundaries parallel to the (π') direction that is not present in the host rock (Fig. S1). Apart from these localized structures, the quartz mylonite shows very similar microstructures, recrystallized grain size, and misorientation axes distribution as the quartz ribbons described above. Zones of very-fine recrystallization with associated disaggregation are not present.

2.4.2 Microstructure and CPO of quartz clasts

The clasts have an angular shape and are surrounded by a cloud of micrometric quartz grains within the pseudotachylyte matrix. The clasts consist of aggregates of recrystallized quartz remarkably similar to the aggregates in the ultramylonite host rock (Fig. 2.6; Fig. S2): (i) the grain size ranges from 1 to > 30 μm and 2 grain size classes (internally distorted coarser *quartz*$_1$ and smaller, strain-free *quartz*$_2$) can be distinguished (Fig. 2.6F); (ii) the spatial distribution of *quartz*$_2$ is heterogeneous with domains of *quartz*$_2$ scattered within an aggregate of dominant *quartz*$_1$ and domains of dominant *quartz*$_2$ (Fig. 2.6A); (iii) *quartz*$_1$ grains have a larger aspect ratio with long axes aligned to define a shape preferred orientation (Fig. 2.6A); (iv) *quartz*$_1$ grains contain subgrains of similar size as *quartz*$_2$ (Fig. 2.6F); and (v) four-grain junctions and alignment of straight grain boundaries are common in the aggregates of predominant *quartz*$_2$ (Fig. 2.5F; Fig. S3). As main difference with respect to the host mylonites, the quartz aggregates of clasts have a smaller average grain size (quartz$_2$ average grain size 3-4 μm; Fig. 2.6F; Fig. S4).

The bulk [c]-axis pole figures of quartz within clasts is characterized by an incomplete girdle with either one asymmetric maximum or two symmetrical maxima as in the host mylonite (though passively rotated during float within the frictional melt) (Fig. 2.6E; Fig. S2C). The CPO is strong in *quartz*$_1$-rich clast domains and weakens in *quartz*$_2$-rich ones with an increased degree of weakening with decreasing grain size (Fig. 2.6C). In crystal and sample coordinates the misorientation axis distributions generally have less well developed maxima than in the host mylonite. For misorientation angles <10° (subgrain boundaries) a maximum is commonly present between the directions (π') and (z) and, in just one case, a weak maximum is parallel to [c]. Misorientation axes of grain boundaries show either a nearly random distribution or one weak maximum parallel to [c] (Fig. 2.6D; Fig. S2B; Fig. S3B). Uncorrelated misorientation angles grade toward the uniform distribution curve moving from coarse-grained to fine-grained areas (M-index diminishes from 0.30 to 0.18), and correlated misorientation angles show maximum values at small angles (< 15°) in addition to the maximum at around 60° (Dauphinè twins) (Fig. 2.6C-E).

Quartz clasts are not completely monomineralic: a micrometric film of a second phase is commonly present along the grain boundaries, locally associated with small iron sulfide crystals (Fig. 2.6B). This second phase along grain boundaries, although more prevalent in areas of dominant *quartz*$_2$, is not associated with important weakening of the CPO and no development of columnar quartz or mixed biotite and quartz layers was observed.

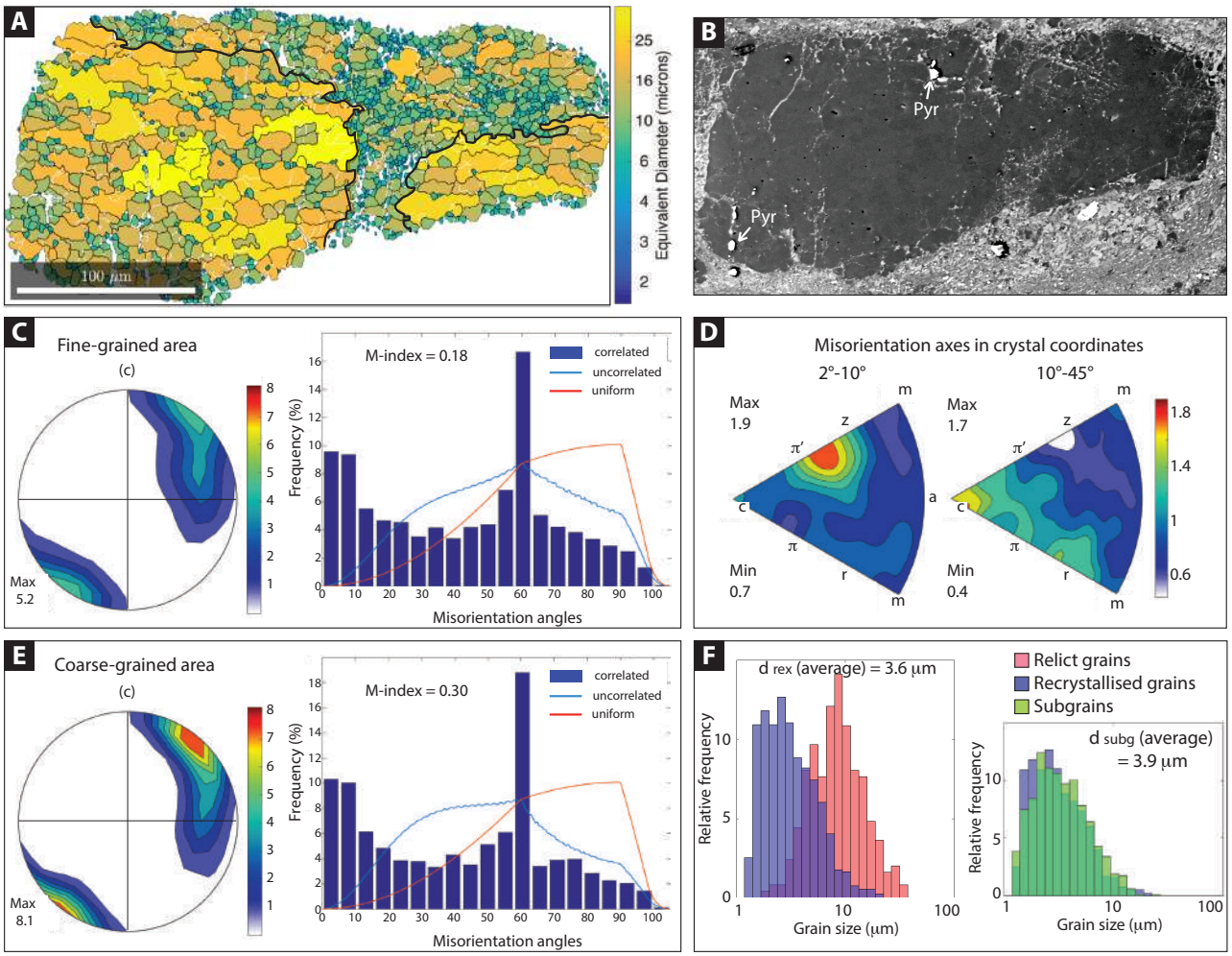

Figure 2. 6 EBSD analysis of quartz clast within pseudotachylyte. A) EBSD map colour coded by grain size (diametre of the equivalent circle). Thick black line separates two subsets in which the microstructure is dominated by fine-grained quartz$_2$ grains (above the line) and coarse-grained quartz$_1$ grains (below the line). B) Backscattered SEM image of the quartz clast. C) (c)-axis contoured pole figures and misorientation angle distributions for the fine-grained area above the thick black line in (A). D) Misorientation axes distribution in crystal coordinates for subgrains (2-10°) and grain boundaries (10-45°) for the whole clast. E) (c)-axis contoured pole figures and misorientation angle distributions for the fine-grained area above the thick black line in (A). F) Grain size distribution for recrystallised (quartz$_2$), relict grains (quartz$_1$), and subgrains for the whole clast.

2.5 Discussion

2.5.1 Deformation mechanisms of quartz in ultramylonite

In the ultramylonite, monomineralic quartz layers underwent recrystallization by dominant subgrain rotation resulting in a strong CPO. The short girdle centered on the Y-axis in the [c]-axis pole figures of recrystallized quartz is typical of prism<a> and rhomb<a> intracrystalline slip (e.g. Schmid and

Casey, 1986). Maxima of misorientation axes of subgrain boundaries correspond to axes of tilt boundaries of {m}<a>, {r}<a>, and {π}<a> slip systems and to combinations of twist boundaries for {z}<a>, and {π'}<a> (Lloyd et al., 1997). These features have been commonly observed in quartz mylonites deformed at amphibolite facies conditions (e.g. Stipp et al., 2002; Toy et al., 2008; Pennacchioni et al., 2010). The similarity between subgrain and new grain sizes indicates negligible grain growth after subgrain rotation recrystallization.

The heterogeneous grain size and the similar CPO for larger and smaller grains suggest that dynamic recrystallization occurred at variable differential stresses under similar temperature conditions, as there is no evidence of changes in the P-T conditions of deformation during mylonitic creep (i.e., no evidence of retrograded metamorphic reactions in biotite, garnet and sillimanite). The average recrystallized grain size in quartz ribbons is 4-5 µm, but overall the number weighted distribution of grain sizes is largely dominated by grains smaller than 4 µm. The smallest new grains (2.5 µm average grain size) dominate in foliation-parallel bands of nearly complete recrystallization. The aggregates of fine recrystallized grains are commonly spatially associated with sillimanite grains that acted as local stress risers within the ribbon (e.g. Bestmann et al., 2006; Cross et al., 2015) that resulted in a decrease in recrystallised grain size of quartz that in turn promoted a change in deformation mechanism within the aggregate. The weakening of the CPO and of the density of misorientation axes of grain boundaries, the development of four-grain junctions and the alignment of straight grain boundaries all suggest that GBS became increasingly active within the finest grained aggregates (e.g. White, 1979). The transition from dominant dislocation creep to dominant GBS has been already inferred for quartz in ultrafine recrystallized aggregates (Behrmann and Mainprice, 1986; Kilian et al., 2011; Fukuda et al., 2018). In the Mont Mary ultramylonites, when recrystallization by subgrain rotation produced an aggregate dominated by small grains, GBS and associated cavitation (Fusseis et al., 2009; Kilian et al., 2011; Menegon et al., 2015) promoted opening along the grain boundaries accommodated by biotite precipitation. Cavitation preferentially occurred along grain boundaries aligned orthogonal to the ribbon, as also observed by Gilgannon et al. (2017), resulting in development of the columnar quartz microstructure (Fig. 5D). Syn-kinematic, stress-controlled precipitation of biotite along the opening grain boundaries is indicated by the strong preferred orientation of biotite orthogonal to cavitation pore walls (Fig. 2E). This process eventually ended up into complete disaggregation of the quartz aggregate and transition to a mixed quartz + biotite matrix. Pinning by a second phase impeded grain growth and caused a permanent switch between dislocation creep and a grain size sensitive (GSS) deformation

mechanism. Dynamic recrystallization of quartz grains finally embedded in the softer biotite matrix was no longer possible and further quartz grain deformation was achieved by dissolution-precipitation processes (Kilian et al., 2011).

2.5.2 Deformation mechanisms of quartz in pseudotachylyte clasts

Quartz clasts within pseudotachylyte veins show microstructures similar to those of the host mylonite, with the important distinction that the degree of fine recrystallization is consistently higher for all the analyzed clasts. This suggest that pseudotachylytes developed from more strongly sheared and more pervasively finely recrystallized ultramylonitic layers than those preserved in the host ultramylonite. The clasts in pseudotachylyte do not show the peripheral disaggregation into quartz + biotite by cavitation process observed in ultramylonites, which could not survive frictional melting due to biotite low melting temperature. The local presence of a thin film of a second phase along grain boundaries is related to the stage of frictional melting as testified by the presence of sulfide droplets (Magloughlin, 2005). The subgrain boundaries misorientation axes generally show a wide maximum between the (π') and (z) directions suggestive of an enhanced activity of rhomb <a> slip system with respect to the host mylonite. In one case, a weak maximum parallel to (m), which can be related to activity of basal <a> slip system, was observed. A switch between dominant prism <a> to combined of prism, rhomb, and basal <a> intracrystalline slip can be interpreted in terms of increase of differential stress (e.g. Tokle et al., 2019) or decrease in temperature (e.g. Stipp et al., 2002), although the concept of temperature dependency of <a> slip systems has been challenged by Kilian and Heilbronner (2017). The common observation of subgrain boundaries misorientation axes parallel to the (π') direction in clasts and in a coseismic recrystallisation band in quartz ribbons at the vein boundary (Fig. S1), may suggest that the very fine recrystallised grains in clasts partly developed during coseismic deformation (Bestmann et al., 2011; Trepmann et al., 2007). This could explain the increased pervasiveness of fine recrystallisation in quartz clasts with respect to host-mylonite ribbons. However, the different activation of slip systems can also be interpreted in terms of differences in orientation of the original quartz ribbon with respect to the kinematic framework (Ceccato et al., 2017).

2.5.3 Paleopiezometry and rheological model

Figure 2.7A displays the deformation mechanism map of quartz calculated for the deformation conditions of the Mont Mary ultramylonites. The flow law of Hirth et al. (2001) is used to calculate the dislocation creep component of the strain rate:

(1) $\dot{\varepsilon} = A f_h \sigma^n e^{(-Q/RT)}$,

where A is the pre-exponential factor ($MPa^{-n}\ s^{-1}$); f_h is the water fugacity; σ is the differential stress (MPa); n is the stress exponent; Q is the activation energy ($J\ mol^{-1}$); R is the gas constant ($J\ K^{-1}\ mol^{-1}$); and T is the temperature (K). The Mont Mary mylonites have been considered to develop under water-deficient conditions based on: (i) the occurrence of synkinematic water-consuming reactions, (ii) the high differential stress during mylonitization (iii) the association of mylonites and pseudotachylytes at amphibolite facies conditions (Pennacchioni and Cesare, 1997), and (iv) the grain boundary morphology of recrystallized quartz (Mancktelow and Pennacchioni, 2004). Nevertheless, the observed healing by biotite precipitation of cavitation pores in ultramylonites indicates that conditions were not totally dry.

The flow law for thin-film pressure solution by den Brok (1998) was used to calculate the grain size sensitive (GSS) component of creep:

(2) $\dot{\varepsilon} = C \frac{\rho_f}{\rho_s} \frac{\sigma^n}{d^m} \frac{VcD_w}{RT}$,

where C is a shape constant, ρ_f and ρ_s are the fluid and solid densities (kg/m^3), d is the grain size (μm), m is the grain size exponent, V is the molar volume ($\mu m^3/mol$), c is the solubility of the solid in the fluid phase (molar fraction), and D_w is the diffusivity of the solid in the grain-boundary fluid ($\mu m^2\ s^{-1}$).

Differential stress during deformation was estimated using the "sliding resolution" piezometer of Cross et al. (2017). The creep of quartz in ultramylonites is considered to have taken place at the temperature and pressure conditions estimated by Pennacchioni and Cesare (1997) of 545 °C and 0.35 GPa for mylonitization, since no syn-kinematic breakdown of high-grade minerals is observed in ultramylonites. All the flow laws parameters and details for derivation of deformation maps are given in the supplementary material.

Figure 7A indicates that the finest-grained aggregates of the host mylonite (RMS ≅ 3 μm), developed at differential stress in excess of 200 MPa and strain rate of about $10^{-9}\ s^{-1}$. In the deformation mechanism map, these values plot in the field of dislocation creep very close to the boundary to GSS creep. The transition from dislocation creep to a process of GBS is recorded by the occurrence

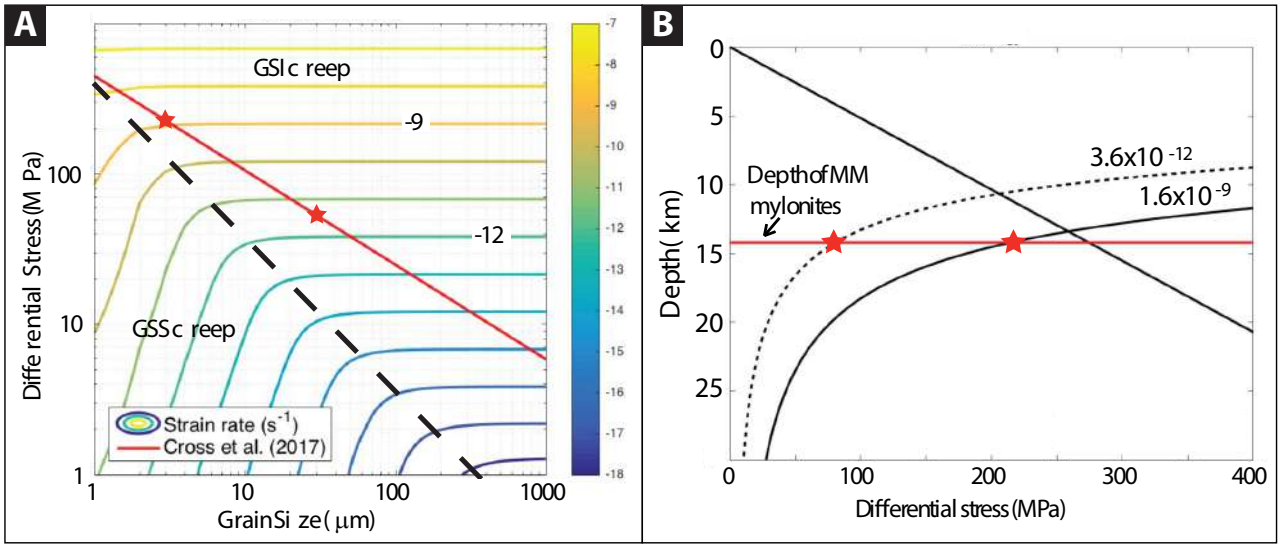

Figure 2. 7 (A) Deformation mechanisms map for quartz with contoured strain rate curves. The red line is the "sliding resolution" piezometer by Cross et al. (2017) while the black dotted line represents the boundary between fields of dominant grain size sensitive and grain size insensitive creep. The two stars correspond to the grain size of coarse recrystallised quartz grains in ribbons (30 μm) and ultrafine aggregates of quartz$_2$ at ribbons boundary (3 μm). Details on the derivation of this map can be found in the main text and supplementary material. (B) Simplified crustal strength diagram for quartz, plotted for the strain rates calculated in (A). The frictional sliding law for an extensional fault is used with a friction coefficient of 0.7. The geothermal gradient is 35 K/km.

of cavitation in the finest grained recrystallized quartz aggregates and disaggregation assisted by precipitation of biotite in micro-cavitation spaces. This transition likely resulted in weakening, that could either imply an increase in strain rate if the shear zone evolved at constant stress, or vice versa a stress drop. The application of paleopiezometry is legitimized by the observation that the new finest recrystallized grains still developed by subgrain rotation before the grain boundaries started to slide and cavitate.

The largest recrystallized grains in quartz ribbons of the host mylonite (30 μm) record differential stresses of about 50 MPa and strain rate in excess of 10^{-11} s^{-1}, i.e. two orders of magnitude slower. In the 2-stages, deformation experiments on quartzite at increasing stress of Kidder et al. (2016), the resulting recrystallized grain size distribution is bimodal, therefore preserving the record of both the earlier lower stress state and the later high stress one. In the Mont Mary shear zone, where the stress evolution was more complex, we can assume that the largest grain size records lower stress condition during the mylonitic deformation that "gradually" evolved to higher stress in ultramylonites. We also calculated deformation maps using the flow law for fine-grained quartz aggregates deforming by mixed diffusion and dislocation creep by Fukuda et al. (2019), and the flow

law for dislocation creep of quartz deformed at high stresses and low temperatures by Tokle et al. (2018). The results are not dissimilar and are shown in the supplementary material (Fig. S6).

In a simplified rheological model of quartz-built crust (Fig. 2.7B), formation of the Mont Mary ultramylonites along a Permian extensional detachment (Pennacchioni and Cesare, 1997) occurred close to the brittle/ductile transition. Assuming that pressure, temperature, and depth remained the same for the low- and high-stress stages, the change in strain rate produced a ca. 3-km downward shift of the brittle/ductile transition. Considering the high-strain rate flow and assuming a depth of 14 km, the associated differential stress is close to the brittle strength of extensional faults, calculated assuming dry conditions (pore fluid factor $\lambda = 0$) and a friction coefficient of 0.7. In our simplification, we assumed that the mylonitic foliation was optimally oriented for reactivation as shear fracture.

2.5.4 Ductile instabilities

Ductile instabilities potentially develop from the positive feedback between shear heating and strain rate in a localized shear zone, - a process known as thermal runaway (Kelemen and Hirth, 2007; Braeck and Podlachikov, 2007; John et al., 2009; Thielmann et al., 2015). This process has been suggested to explain the association of coeval pseudotachylytes and mylonites in the deep crust (Hobbs et al., 1986; White, 1996, 2012; Stewart and Miranda, 2017).

Localized zones of finely recrystallized grain size and elevated strain rates may represent ideal precursors for thermal runaway (Thielmann et al., 2015), provided the differential stress exceed a critical threshold. Thielmann et al. (2015) showed that pinning due to secondary phases favors the instability by inhibiting grain growth. In the Mont Mary samples, quartz clasts within pseudotachylytes show a more extensive grain size reduction than in the host ultramylonite and this may suggest that pseudotachylytes developed from zones where thermal runaway was favored by strong grain size reduction and high strain rate.

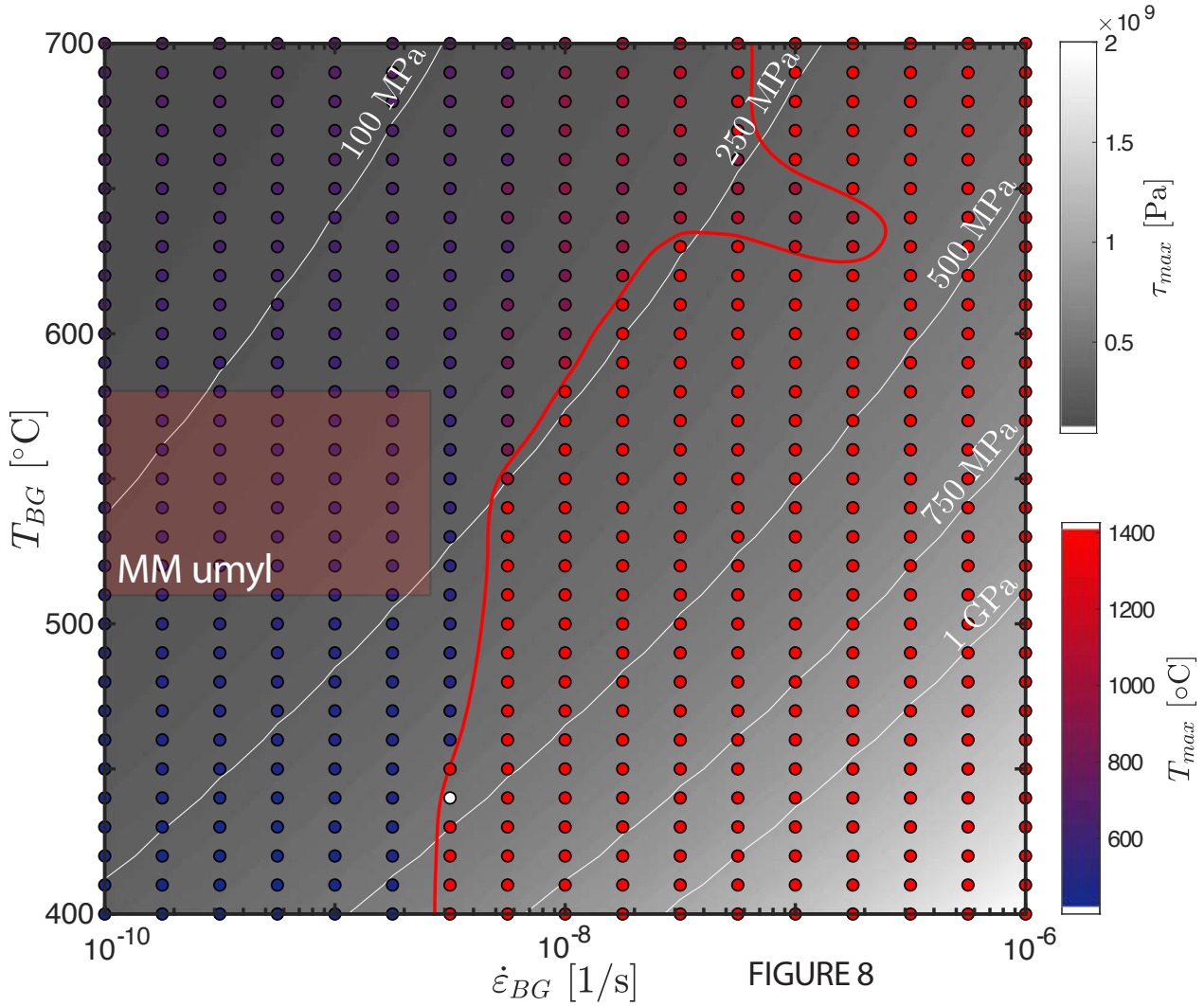

Figure 2. 8 Results of a 1D model coupling the evolution of stress, grain size and temperature in a viscoelastic medium for quartz rheology. Each circle indicates a simulation, with colors denoting the maximum temperature reached in the respective simulation (simulations were aborted when temperatures reached values of 1700 K). Peak stresses are shown in the background in grey colors, with white contour lines denoting selected stress levels. The hand-drawn solid red line separates the thermal runaway regime from the stable regime. The red shaded area approximates the estimated temperature/strain rate conditions for the Mont Mary ultramylonites.

We use the model presented in Thielmann et al. (2015) and Thielmann (2018) to estimate whether ductile thermal runaway is a viable process to generate pseudotachylytes under the deformation conditions recorded in the Mont Mary ultramylonites. In this model, a viscoelastic slab is deformed in simple shear, taking into account the evolution of both grain size and temperature (see Thielmann (2018) for a detailed derivation of the model and the solution procedure). Here, we assume a 1 km thick slab deformed in simple shear. In the middle of the slab, we inserted a 2 m wide zone where the rheological parameters are perturbed by increasing the strain rate of both dislocation creep and GSS creep by a factor of 10 (additional material parameters, numerical details, and a study of the impact of perturbing both rheological and grain growth parameters can be found in the

supplementary material). 527 simulations were performed at different background strain rates (ranging from 10^{-10} to 10^{-6} s^{-1}) and temperatures (ranging from 400 to 700 °C). The peak stress as well as the maximum achieved temperature were recorded for each simulation. Simulations were aborted whenever temperatures reached values larger than 1427 °C (1700 K), as melting would certainly have occurred at this temperature. Such high temperatures are only reached in models that exhibit thermal runaway, which is why we used the maximum temperature as an indicator of thermal runaway. In figure 2.8, we show the numerical model results. Each simulation is indicated with a circle, with the circle color indicating the maximum temperature obtained during the simulation. Peak stresses are shown in the background in grey colors, with white contour lines denoting certain stress levels. The solid red line in figure 8 separates the simulations exhibiting thermal runaway from simulations not resulting in instability.

Model results indicate that ductile thermal runaway can be achieved in a quartz-rich crust, given that rheological contrasts within the crust are large enough. Critical stresses at the regime boundary range from approximately 250 to 500 MPa. In the ranges of temperature and strain rate estimated for the Mont Mary ultramylonites the model predicts a stable behaviour. However, a slightly faster strain rate of approximately $5*10^{-9}$ s^{-1} could trigger thermal runaway at a critical stress (~ 250 MPa) that at the inferred depth of the Mont Mary mylonites (10-18 km) is comparable to the brittle strength of a quartz-rich rock (Fig. 2.7B).

The microstructural analysis of Mont Mary ultramylonite and of survivor clasts in pseudotachylyte provides evidence that melting was preceded by the local switch in the dominant deformation mechanism of quartz from dislocation creep to GBS creep. Stewart and Miranda (2017) interpreted similar microstructures in a pseudotachylyte-mylonite association from the South Mountains metamorphic core complex in Arizona as evidence for pseudotachylyte development as ductile instabilities. They argued that GBS domains in the mylonitic quartz aggregates record ductile instabilities triggering pseudotachylyte nucleation due to high strain rate/low effective viscosity during GBS. We tend to discard this interpretation for the Mont Mary ultramylonites, since the mechanism of GBS is followed by cavitation and precipitation of biotite in pore spaces. Therefore, the strain rate-limiting process during quartz disaggregation is the rate of fluid-assisted precipitation of oriented biotite, which cannot occur at seismic rates. However, although the switch to GBS induces a weakening that may initiate instability, Thielmann (2018) showed that the weakening associated with dislocation-accommodated grain boundary sliding is such that critical runaway stresses are never reached. Once the mixed layer of biotite and quartz is fully developed, the

associated weakening will impede the development of a ductile instability. Therefore, although the model shows that thermal runaway could be possible in a quartzitic rock at conditions comparable to those we estimated for our case study, the microstructural record preserved in the highest strain microstructures of the Mont Mary ultramylonites apparently excludes that thermal runaway did actually occur.

2.5.5 Failure mechanisms

Microstructures in the Mont Mary ultramylonite record a multi-stage process of subgrain rotation recrystallization where localized, ultrafine-grained aggregates associated with high differential stresses (>200 MPa) overprinted lower stress/strain rate, coarser recrystallized grains. Fitz Gerald et al. (2006) described a similar bimodal distribution of quartz grain size, with coarser (100's μm) recrystallized grains partially mantled by equant, polygonal grains a few microns in diameter for mylonitic pegmatite from the same Mont Mary shear zone. Such an increase in stress, associated with the extreme strain localization in the ultramylonites, could be interpreted as result of a progressive deformation at decreasing temperature. Using the flow law by Hirth et al. (2001) a stress rise of over 150 MPa at constant strain rate would imply a temperature decrease of ca. 200 °C. However, there is no evidence of such a temperature drop, as the synkinematic amphibolite-facies mineral assemblage is always stable in the ultramylonites. We infer that the observed high strain rate/differential stress evolution in the ultramylonite resulted from transient, externally-induced change of boundary conditions under constant ambient temperature.

The strain rate of 10^{-9} s^{-1} estimated for the finest grained quartz of ultramylonites lie at the higher end of the typical range of strain rates for quartz dislocation creep in shear zones (Fagereng and Biggs, 2019). Such accelerated creep rates and high differential stress can be related to major seismic events occurring in the upper crust that altered the steady state conditions of ductile flow in the underlying crustal domains (Ellis and Stöckhert, 2004). Figure 2.7B shows that the differential stresses recorded in the finest-grained portions of the host mylonite are close to the brittle failure criterion for an extensional fault. This suggests that pseudotachylytes may develop within the ductile portion of the crust due to the strain-rate dependent transient deepening of the brittle/ductile transition following a major earthquake in the seismogenic upper crust. This process may enable brittle failure at temperatures at which a quartz-rich rock should be able to flow at much

lower differential stresses if the strain rate is within a typical range for mylonitic shear zones. According to this interpretation, the Mont Mary pseudotachylytes may represent aftershock seismicity related to major events in the upper crust (Jamtveit et al., 2018).

2.6 Conclusions

The numerical model shows, for the first time, that thermal runaway could be a viable mechanisms for earthquake nucleation in the middle to lower crust for a quartz-rich rheology. The conditions we determined for the Mont Mary ultramylonites are not far from the switch between stable and unstable flow as predicted from the model. However, the whole recorded microstructural evolution of quartz in ultramylonites is compatible with aseismic flow. The observed overprinting of a high stress (> 200 MPa) deformation phase over a lower stress microstructure under roughly constant temperature is explained by transients of accelerated creep induced in the ductile crust by stress transfer from a seismogenic source in the upper crust (Ellis and Stöckhert, 2004; Jamtveit et al. 2018). Transients of high strain rate in the lower crust can lead to brittle failure if the strain rate is high enough to cause a rheological switch due to the transient downward migration of the brittle/ductile transition. Our calculations show that this could have happened for the Mont Mary ultramylonites.

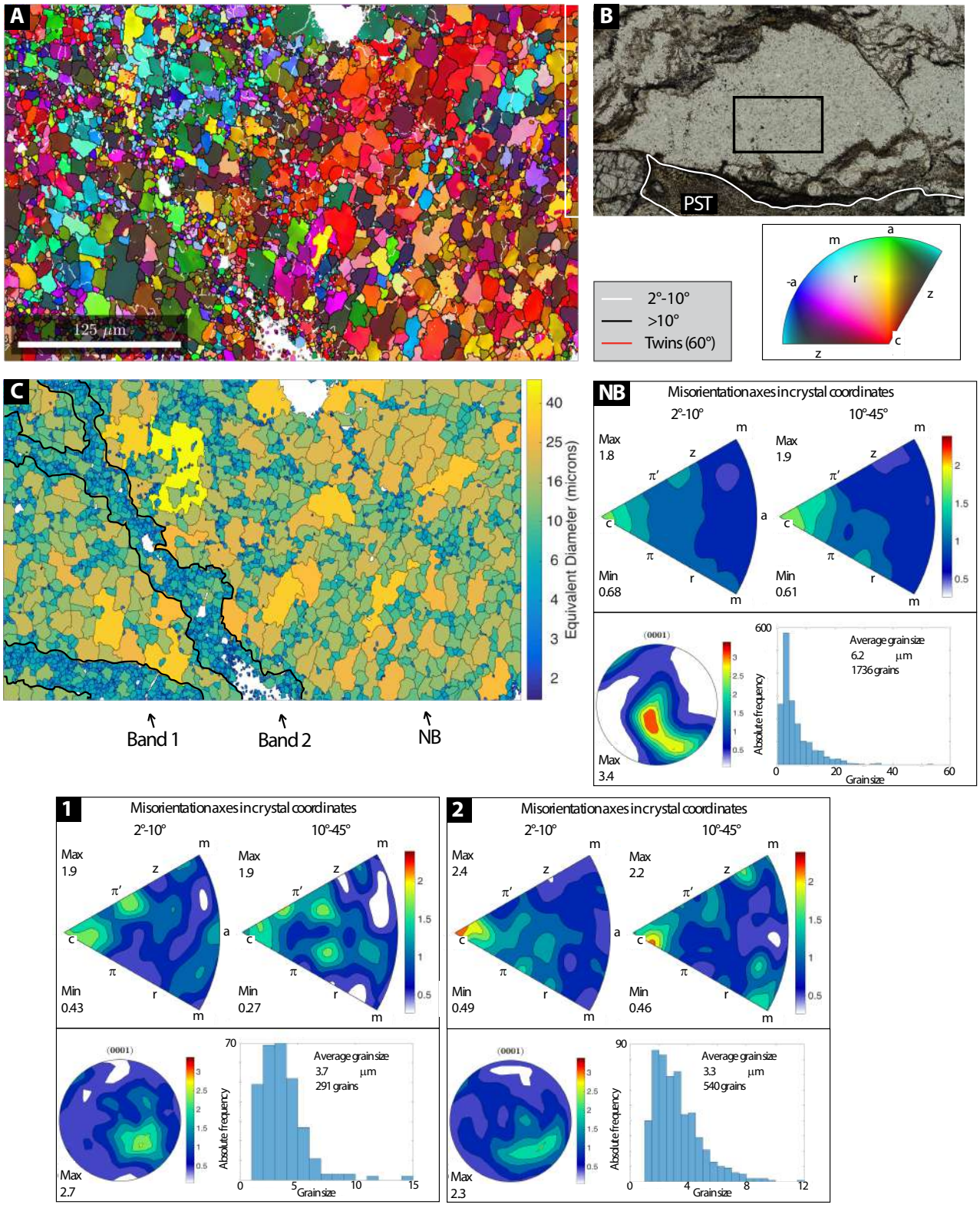
A
125 μm
B
PST
2°-10°
>10°
Twins (60°)
m
a
-a
r
z
c
C
Equivalent Diameter (microns)
40
25
16
10
6
4
3
2
Band 1
Band 2
NB
NB
Misorientation axes in crystal coordinates
2°-10°
10°-45°
Max 1.8
Min 0.68
Max 1.9
Min 0.61
(0001)
Max 3.4
Average grain size 6.2 μm
1736 grains
Absolute frequency
Grain size
1
Misorientation axes in crystal coordinates
2°-10°
10°-45°
Max 1.9
Min 0.43
Max 1.9
Min 0.27
Max 2.7
Average grain size 3.7 μm
291 grains
2
Misorientation axes in crystal coordinates
2°-10°
10°-45°
Max 2.4
Min 0.49
Max 2.2
Min 0.46
Max 2.3
Average grain size 3.3 μm
540 grains

FIGURE S1

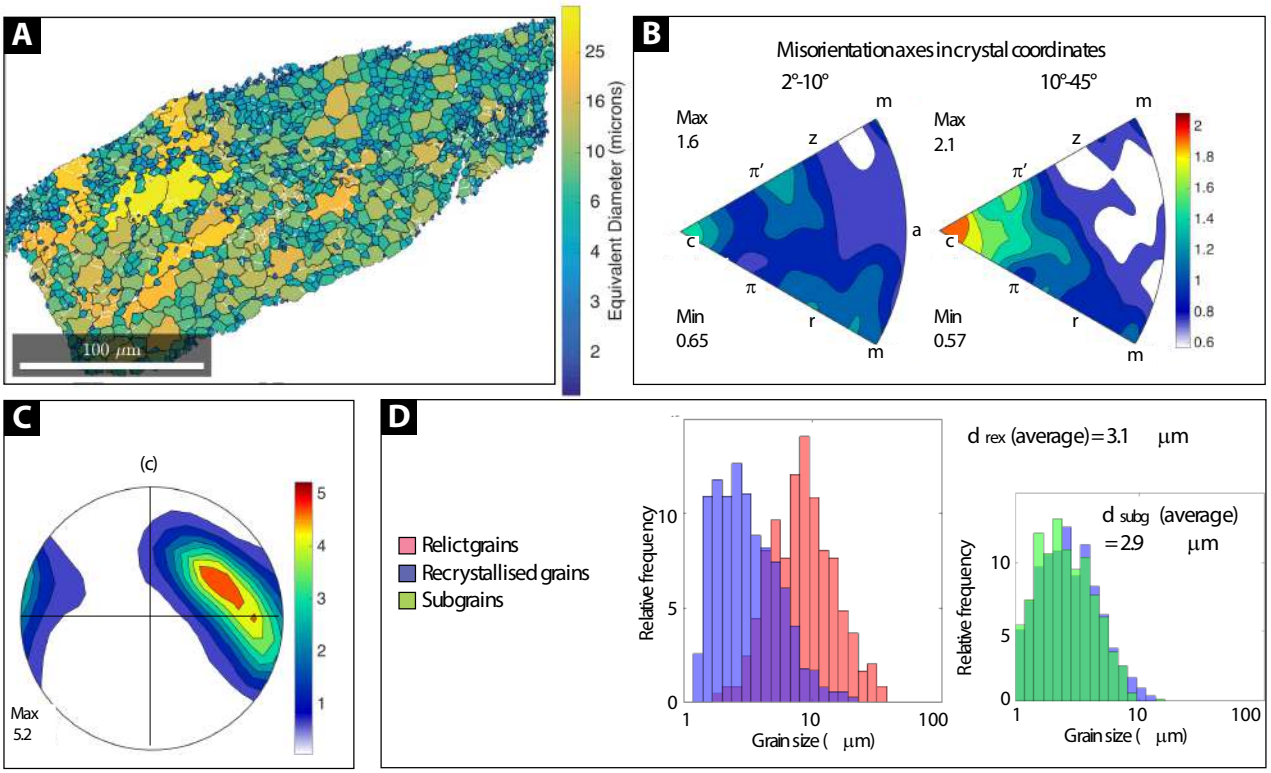
A
100 μm
Equivalent Diameter (microns)
25
16
10
6
4
3
2
B
Misorientation axes in crystal coordinates
2°-10°
10°-45°
Max
1.6
Min
0.65
Max
2.1
Min
0.57
m
z
π′
c
a
π
r
2
1.8
1.6
1.4
1.2
1
0.8
0.6
C
(c)
Max
5.2
5
4
3
2
1
D
Relict grains
Recrystallised grains
Subgrains
Relative frequency
Grain size (μm)
d rex (average) = 3.1 μm
d subg (average) = 2.9 μm

FIGURE S2

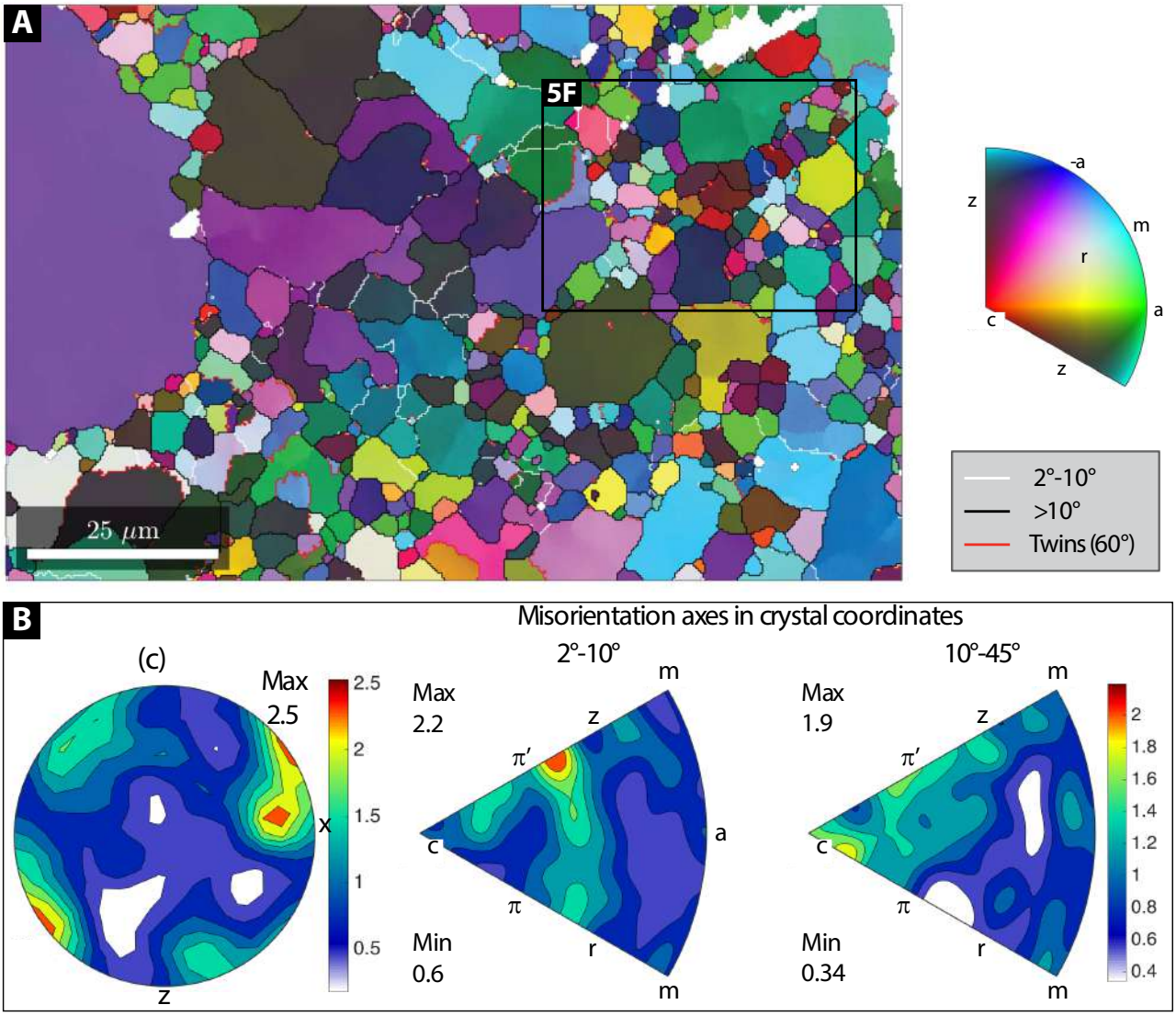
A
5F
25 μm
-a
z
m
r
a
c
z
2°-10°
>10°
Twins (60°)
B
Misorientation axes in crystal coordinates
(c)
Max
2.5
Min
0.6
2°-10°
Max
2.2
Min
0.6
10°-45°
Max
1.9
Min
0.34
x
z
m
a
c
π
π′
r

FIGURE S3

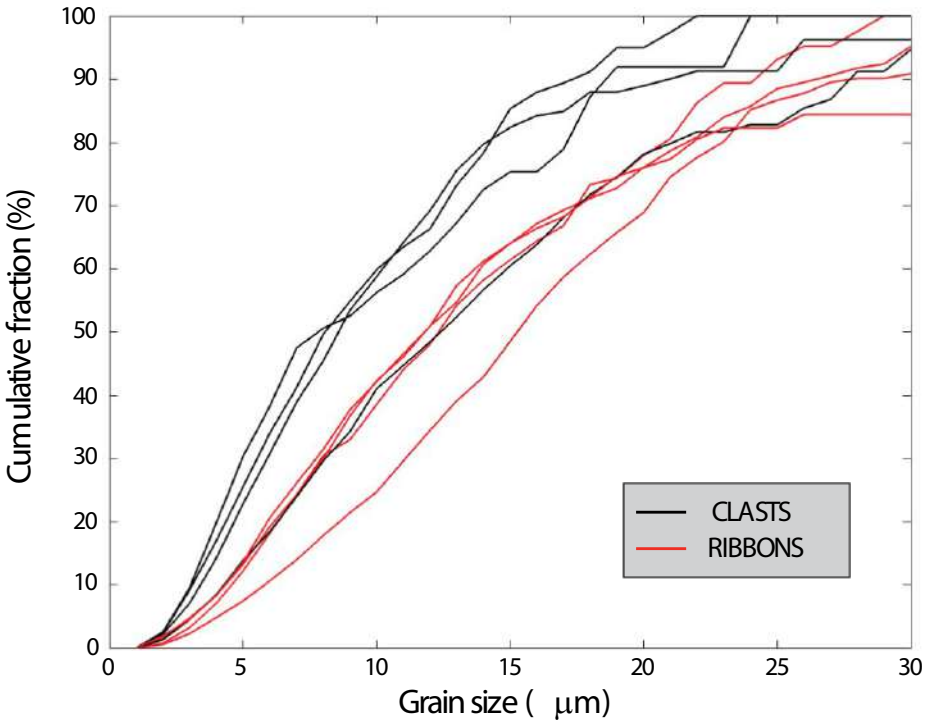
Cumulative fraction (%)
100
90
80
70
60
50
40
30
20
10
0
0
5
10
15
20
25
30
Grain size (μm)
CLASTS
RIBBONS

FIGURE S4

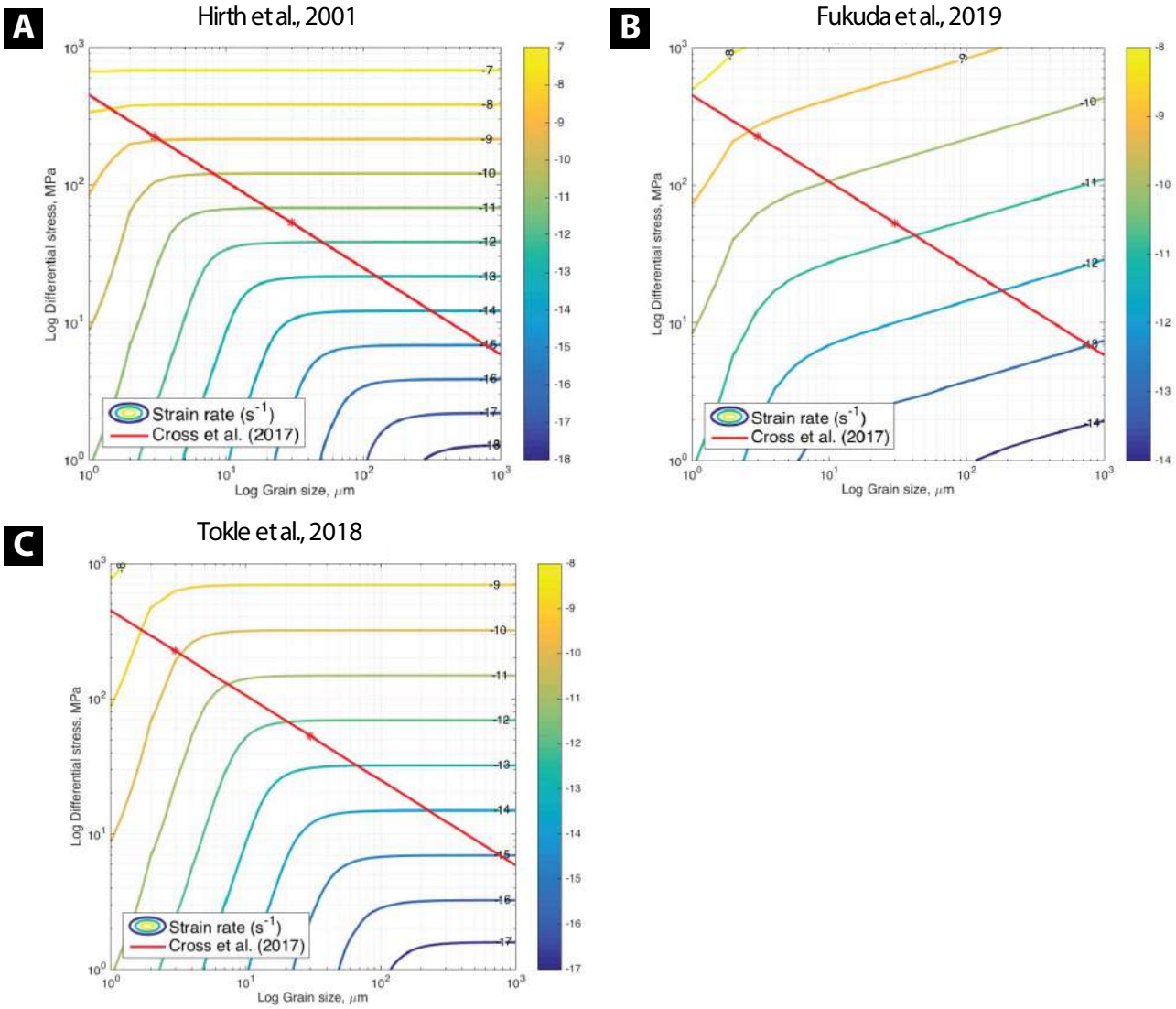
A
Hirth et al., 2001
B
Fukuda et al., 2019
C
Tokle et al., 2018
Log Differential stress, MPa
Log Grain size, μm
Strain rate (s-1)
Cross et al. (2017)

FIGURE S5

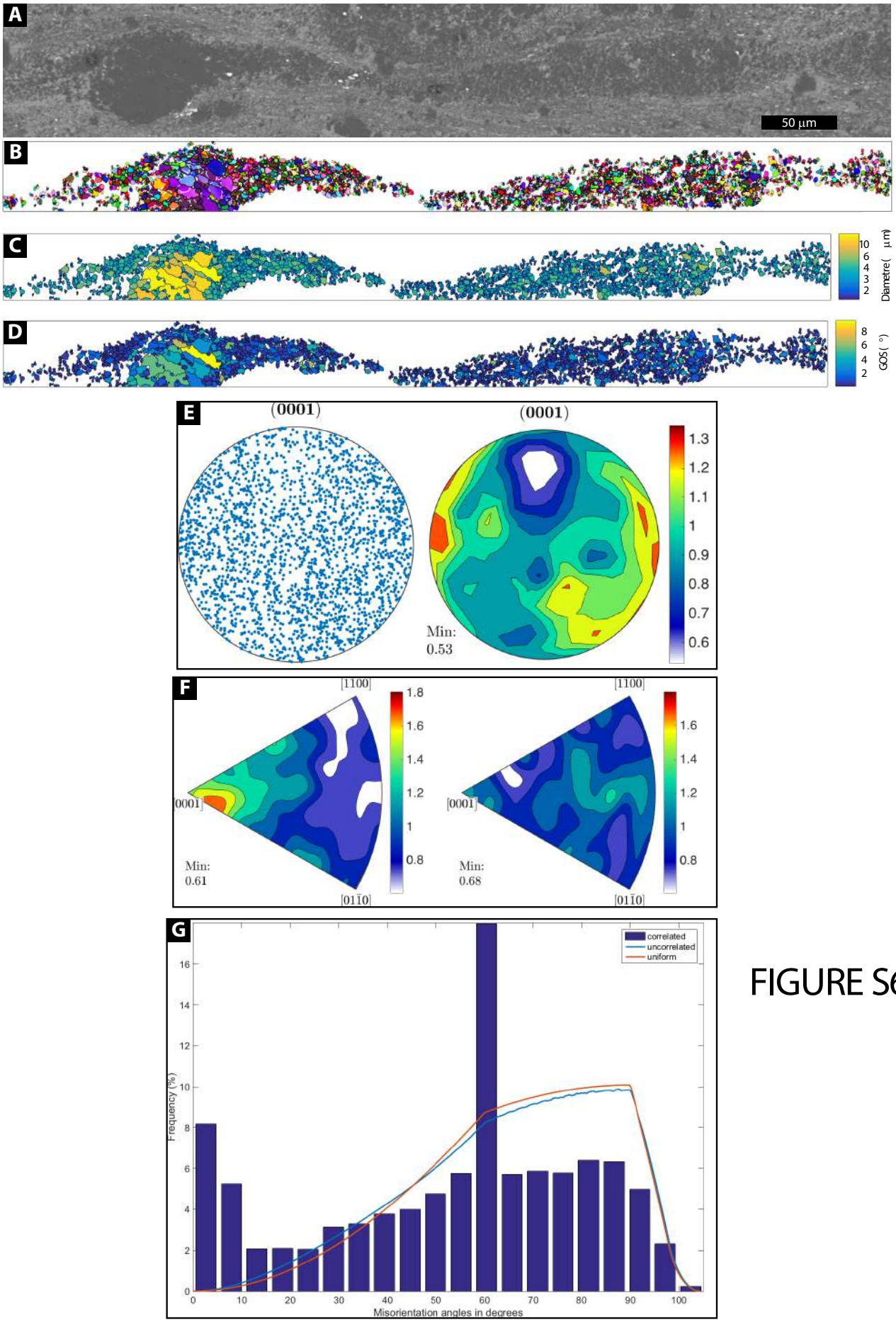
A
50 µm
B
C
10
6
4
3
2
Diametre(µm)
D
8
6
4
2
GOS(°)
E
(0001)
(0001)
1.3
1.2
1.1
1
0.9
0.8
0.7
0.6
Min:
0.53
F
[1100]
[1100]
1.8
1.6
1.4
1.2
1
0.8
[0001]
[0001]
Min:
0.61
Min:
0.68
[01$\bar{1}$0]
[01$\bar{1}$0]
G
correlated
uncorrelated
uniform
Frequency (%)
Misorientation angles in degrees

FIGURE S6

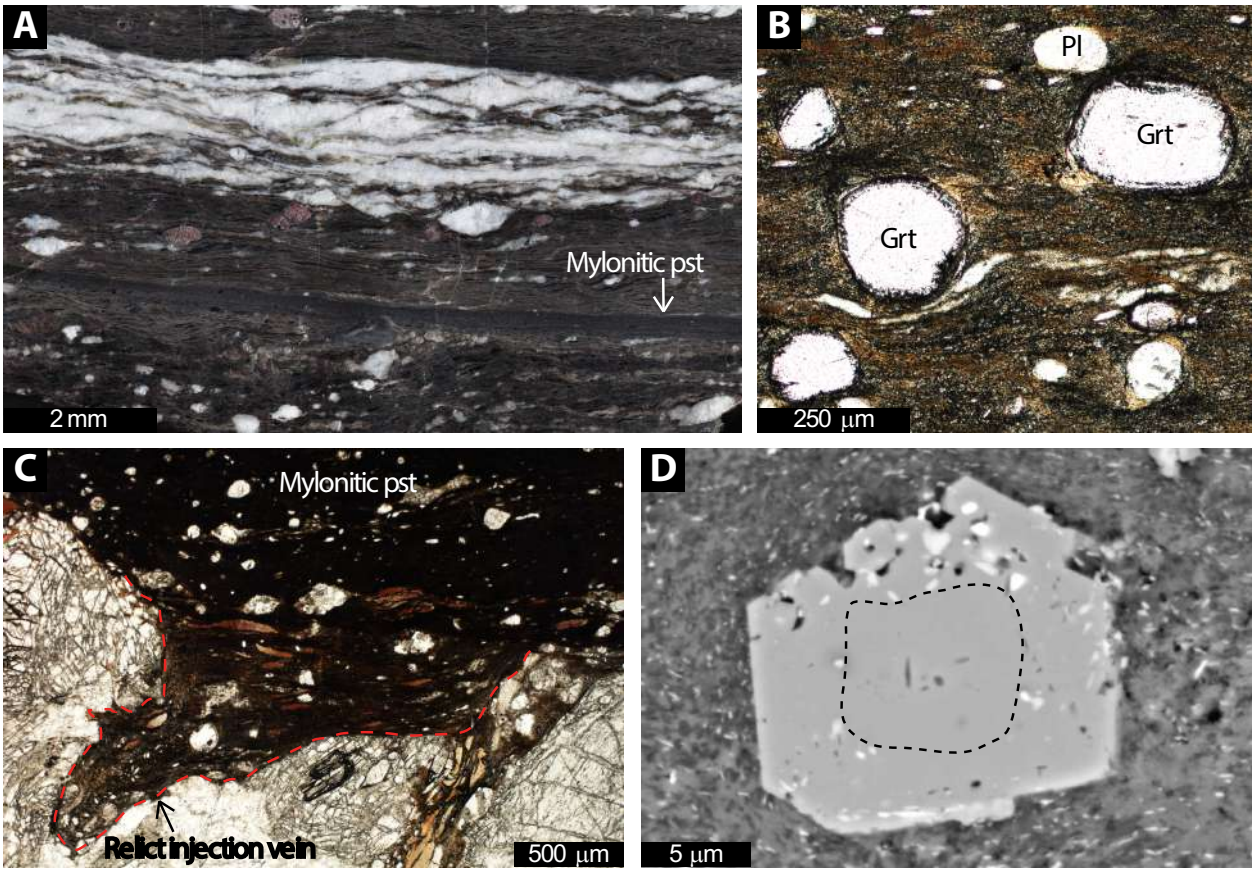
A
Mylonitic pst
2 mm
B
Pl
Grt
Grt
250 µm
C
Mylonitic pst
Relict injection vein
500 µm
D
5 µm

FIGURE S7

Figure captions

Figure S1
EBSD analysis of quartz aggregates at the boundary of pseudotachylyte. A) Inverse pole figure map colour coded with respect to the Y direction. The trace of the mylonitic foliation is horizontal. B) Plane-polarised C) EBSD maps of quartz grains colour coded according to grain size (equivalent grain diameter). Thick black lines highlight two bands of fine-grained recrystallised grains. B1)-B2)-NB) Misorientation axes distribution, (c)-axis contoured pole figures, and grain size distribution of band 1, band 2, and the whole map without the two bands, respectively.

Figure S2
EBSD analysis of quartz clast within pseudotachylyte. A) EBSD map colour coded by grain size (equivalent grain diameter). B) Misorientation axes distribution in crystal coordinates for subgrains (2-10°) and grain boundaries (10-45°). C) (c)-axis contoured pole figure for all grains. D) Grain size distribution for recrystallised ($quartz_2$), relict grains ($quartz_1$), and subgrains.

Figure S3
EBSD analysis of quartz clast within pseudotachylyte. A) Inverse pole figure map colour coded with respect to the Y direction, with location of figure 5F. B) (c)-axis contoured pole figure for all grains and misorientation axes distribution in crystal coordinates for subgrains (2-10°) and grain boundaries (10-45°).

Figure S4
Comparison of grain size distribution of clasts and recrystallised ribbons. The lines indicate the area fraction occupied by grains below a certain equivalent diametre.

Figure S5
Deformation mechanism maps calculated using the flow laws of (A) Hirth et al., 2001; (B) Fukuda et al., 2019; (C) Tokle et al., 2018 for GSI creep and the flow law of den Brok et al., (1998) for GSS creep.

Figure S6
EBSD analysis of a sheared quartz clast in a mylonitised pseudotachylyte. A) BSE image of the sheared clast. B) Inverse pole figure map colour coded with respect to the Y direction. C) EBSD map colour coded by grain size (equivalent grain diameter). D) EBSD map colour coded by Grain Orientation Spread (GOS). E) (c)-axis contoured pole figure for all grains. F) Misorientation axes distribution in crystal coordinates for subgrains (2-10°) and grain boundaries (10-45°). G) Misorientation angle distributions for correlated and uncorrelated misorientations. The red line represents the theoretical random distribution for the point group 321.

Figure S7
Microstructures of a mylonitic pseudotachylyte. A) Polished slab of a loose block of pseudotachylyte-hosting amphibolitic ultramylonite (sample SM29). The dark layer is a mylonitised pseudotachylyte. B) Rounded garnets in the mylonitic pseudotachylyte show a rim full of inclusions, while the nucleus has no inclusions. C) At the boundary of the mylonitic pseudotachylyte a relict injection vein is preserved. D) Garnet within the mylonitic pseudotachylyte shows development of crystal facets and a rim rich of sulfide (pyrite) inclusions.

Derivation of flow laws

Table S1. Parameters adopted in the rheological calculations

	Parameter	Value	Units	Ref.
P	Pressure	0.35	GPa	(1)
T	Temperature	818	K	(1)
A	Pre-exponential factor	6.30957*10^-12	$MPa^{-n}\ s^{-1}$	(2)
fh	Water fugacity	30.6	MPa	(3)
Q	Activation energy	135000	$J\ mol^{-1}$	(2)
n_{disl}	Stress exponent	4		(2)
C	Shape constant	44		(4)
ρ_f	Fluid density	419	kg/m^3	(3)
ρ_s	Solid density	2650	kg/m^3	
n_{diff}	Stress exponent	1		(4)
m	Grain size exponent	3		(4)
V	Molar volume quartz	2.269*10^7	$(\mu m^3/mol)$	
c	Solubility of solid in the fluid phase	0.0011	Molar fraction	(5)
Dw	Diffusivity of the solid in the fluid film	4.5257e-13	$\mu m2\ ^{s-1}$	(4)

The bulk strain rate ($\dot{\varepsilon}bul$) of a mineral aggregate is given by:

(1) $\dot{\varepsilon}bulk = \dot{\varepsilon}Disl + \dot{\varepsilon}Diff$

where: $\dot{\varepsilon}Disl$ and $\dot{\varepsilon}Diff$ represents the strain rates of dislocation creep and diffusion creep of mineral components, respectively.
The deformation mechanisms map of Fig. 7a has been calculated as follows.
The flow law of Hirth et al. (2001) is used to calculate the dislocation creep component of the strain rate:

(2) $\dot{\varepsilon}Disl = Af_h\sigma^n e^{(-Q/RT)}$,

where A is the pre-exponential factor ($MPa^{-n}\ s^{-1}$); f_h is the water fugacity; σ is the differential stress (MPa); n is the stress exponent; Q is the activation energy ($J\ mol^{-1}$); R is the gas constant ($J\ K^{-1}\ mol^{-1}$); and T is the temperature (K).
Considering that ductile flow is still possible at estimated differential stress of 226 MPa, the maximum fluid pressure that can be reached without hydraulic fracturing is around 90 MPa. This is a maximum value and probably an overestimation since the Mont Mary mylonites have been considered water-deficient. Water fugacity and fluid density are then calculated for this fluid pressure and T of 545°C from the Tony Withers' water fugacity calculator (https://www.esci.umn.edu/people/researchers/withe012/fugacity.htm) based on the equation of state by Pitzer and Sterner (1994) and the analytical solution presented in Sterner and Pitzer (1994).
Based on petrological observations, Pennacchioni and Cesare (1997) estimated a maximum and a minimum value for water activity in the fluid phase of 0.90-0.95 and 0.3, respectively. We assumed an intermediate value of 0.6. We applied this coefficient to the water fugacity previously calculated to obtain the final value of 30.6 MPa.

Following Platt (2015) and Ceccato et al. (2018), the flow law for thin-film pressure solution by den Brok (1998) was used to calculate the grain size sensitive (GSS) component of creep:

(3) $\dot{\varepsilon Diff} = C \frac{\rho_f}{\rho_s} \frac{\sigma^n}{d^m} \frac{VcD_w}{RT}$,

where C is a shape constant, ρ_f and ρ_s are the fluid and solid densities (kg/m^3), d is the grain size (μm), m is the grain size exponent, V is the molar volume (μm^3/mol), c is the solubility of the solid in the fluid phase (molar fraction), and D_w is the diffusivity of the solid in the grain-boundary fluid (μm^2 s^{-1}). Quartz solubility and diffusivity in the thin-film (grain boundary) fluid were calculated following Fournier and Potter (1982) and Burnham et al. (1969).

References:

Pennacchioni, G., & Cesare, B. (1997). Ductile-brittle transition in pre-Alpine amphibolite facies mylonites during evolution from water-present to water-deficient conditions (Mont Mary nappe, Italian Western Alps). *Journal of Metamorphic Geology*, *15*(6), 777-791.

Hirth, G., Teyssier, C., & Dunlap, J. W. (2001). An evaluation of quartzite flow laws based on comparisons between experimentally and naturally deformed rocks. *International Journal of Earth Sciences*, *90*(1), 77-87.

Pitzer, K. S., & Sterner, S. M. (1994). Equations of state valid continuously from zero to extreme pressures for H2O and CO2. *The Journal of chemical physics*, *101*(4), 3111-3116.

Den Brok, S. W. J. (1998). Effect of microcracking on pressure-solution strain rate: The Gratz grain-boundary model. *Geology*, *26*(10), 915-918.

Fournier, R. O., & Potter II, R. W. (1982). An equation correlating the solubility of quartz in water from 25 to 900 C at pressures up to 10,000 bars. *Geochimica et Cosmochimica Acta*, *46*(10), 1969-1973.

Sterner, S. M., & Pitzer, K. S. (1994). An equation of state for carbon dioxide valid from zero to extreme pressures. *Contributions to Mineralogy and Petrology*, *117*(4), 362-374.

Burnham, C.W., Holloway, J. R., and Davis, N. F.: Thermodynamic Properties of Water to 1000 _C and 10,000 Bars, Geol. Soc. Am. Bull., 132, 1–96, https://doi.org/10.1130/SPE132, 1969.

Ceccato, A., Menegon, L., Pennacchioni, G., & Morales, L. F. G. (2018). Myrmekite and strain weakening in granitoid mylonites. *Solid Earth*, *9*(6), 1399-1399.

Numerical model description

The numerical model used to estimate the critical parameters needed for grain size assisted thermal runaway (GSATR) is based on the model derived in Thielmann et al. (2015) and Thielmann (2018). This model essentially describes the evolution of stress, grain size and temperature in a slab which is deformed in simple shear. In the middle of the slab, a thin heterogeneity in material parameters is introduced. In this study, we assume a 1 km thick slab with a material perturbation with thickness 2 m. This values have been chosen to represent the Mont Mary mylonitic horizon (metric) in the framework of the mostly undeformed Mont Mary nappe (kilometric). Thermal runaway localises in the central part of the perturbed zone. We assume that the material deforms in a viscoelastic manner, with the viscous rheology given by a combination of thin film pressure solution (den Brok, 1998) and dislocation creep (Hirth et al. 2001). The evolution of the mean grain size d is approximated using a single phase grain growth law (Rozel et. al 2011):

$$(4)\ \dot{d} = \frac{k_0 e^{-\frac{Q_g}{RT}}}{p d^{p-1}} - \lambda \frac{F_d}{\gamma} d^2 \Psi$$

where the grain growth term depends on the activation energy for grain growth Q_g,prefactor k_0 and grain growth exponent p. Grain size reduction is described with a reduction term that depends on the energy partitioning coefficient λ, the reduction factor F_d (which depends on the properties of the grain size distribution, see Thielmann (2018)), surface tension γ and Ψ, the deformational work done in dislocation creep. In this study, we used the parameters from Fukuda et al. (2019) to describe grain growth. The partitioning coefficient λ was set to 0.1, meaning that 10% of the deformational work done in dislocation creep are used for grain size reduction and the rest of the irreversible deformational work is dissipated as heat.

The material perturbation in the middle of the slab was prescribed by multiplying both the rheological prefactors C and A with a constant prefactor f_r as well as multiplying the grain growth prefactor k_0 with a factor f_g. We explored the effect of perturbing these material parameters by running a set of simulations at a background temperature of 500°C and varying strain rates. The results of this study can be found in fig. S5. The 4 different plots correspond to 4 different values of f_g (0.001, 0.01,0.1 and 1). The axes of the individual plots correspond to the employed background strain rate (x-axis) and the rheological perturbation factor f_r (y-axis). Each symbol corresponds to a single simulations, with the color denoting the maximum temperature reached during the simulation. The maximum temperature was limited to 1600 K in the simulations, as at this temperature melting would have certainly occurred. Only simulations where thermal runaway occurred exhibit such large temperatures. The thermal runaway regime is therefore also denoted in fig. S5 with a yellow area.

We can see that varying both rheological and growth prefactors do affect the occurrence of thermal runaway. The growth prefactor does have a rather minor effect. In particular, varying the rheological prefactor may shift the critical strain rate by approximately one magnitude. We also find that there is an optimal range of the rheological prefactor, where thermal runaway occurs at the lowest background strain rates.

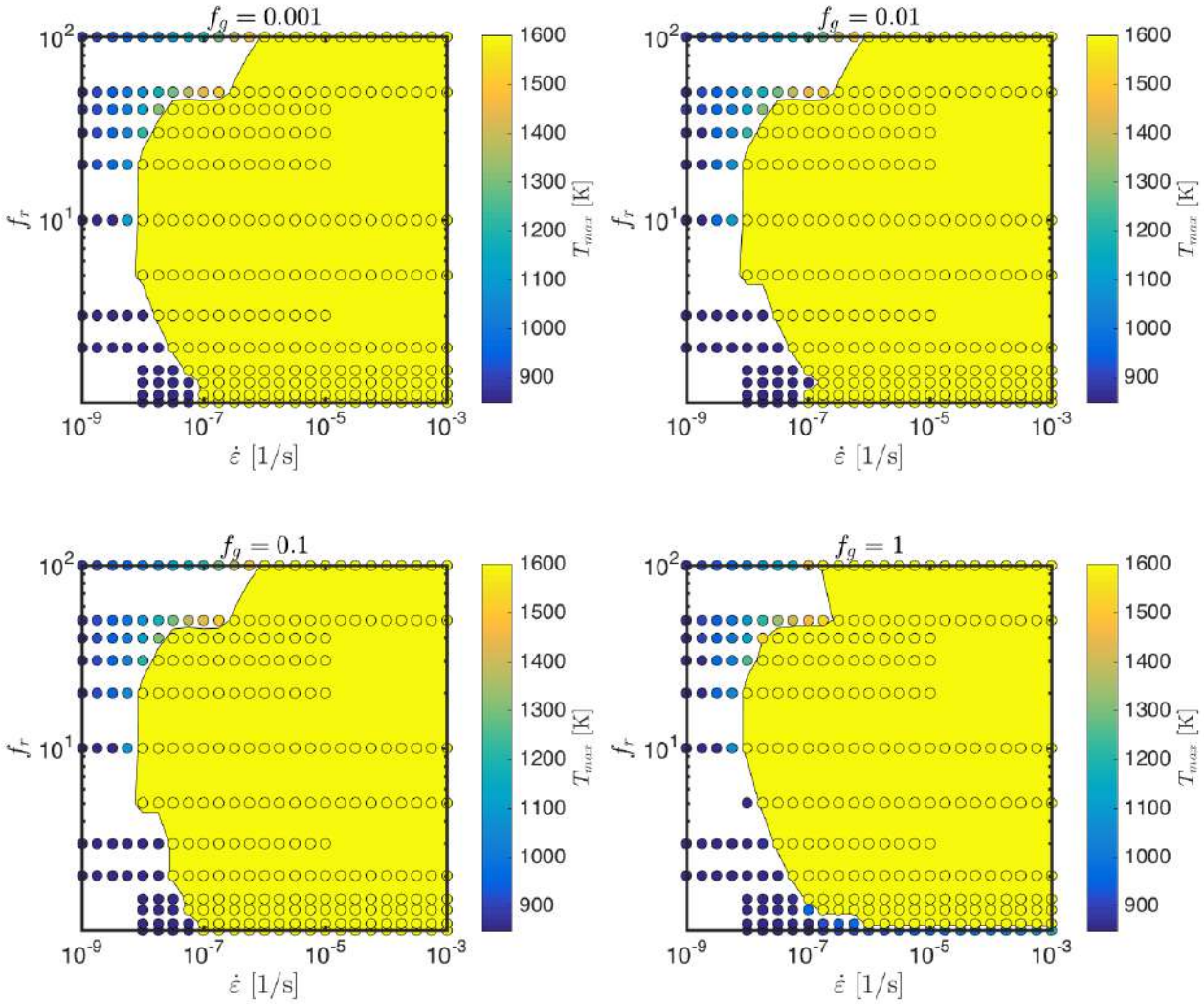

Figure S8: Effect of rheological f_r and grain growth prefactor f_g on the occurrence of thermal runaway at a temperature of 550°C. Each panel represents a simulation set where f_g was kept constant and both f_r and background strain rate $\dot{\varepsilon}$ were varied. Each circle represent a simulation, with the color denoting the maximum temperature reached in the simulation. All simulations reaching 1600 K were considered to exhibit thermal runaway. The yellow area indicates this regime.

References

Fukuda, J., H. Raimbourg, I. Shimizu, K. Neufeld, and H. Stünitz (2019), Experimental grain growth of quartz aggregates under wet conditions and its application to deformation in nature, *Solid Earth*, *10*(3), 621–636, doi:10.5194/se-10-621-2019.

Nichols, S., and S. Mackwell (1991), Grain growth in porous olivine aggregates, Physics and Chemistry of Minerals, 18(4), 269–278, doi:10.1007/BF00202580.

Rozel, A., Ricard, Y., & Bercovici, D. (2011). A thermodynamically self-consistent damage equation for grain size evolution during dynamic recrystallization. Geophysical Journal International, 184(2), 719-728.

Austin, N., and B. Evans (2007), Paleowattmeters: A scaling relation for dynamically recrystallized grain

size,, 35, 343–346, doi:10.1130/G23244A.1.

Chrysochoos, A., and F. Belmahjoub (1992), Thermographic analysis of thermomechanical couplings,, 44, 55–68.

Griggs, D. (1967), Hydrolytic Weakening of Quartz and Other Silicates*, Geophysical Journal of the Royal Astronomical Society, 19–31

Herwegh, M., J. Linckens, A. Ebert, A. Berger, and S. Brodhag (2011), The Role of Second Phases for Controlling Microstructural Evolution in Polymineralic Rocks: A review, Journal of Structural Geology, 1728–1750, doi:10.1016/j.jsg.2011.08.011.

Hirth, G., and J. Tullis (1992), Dislocation creep regimes in quartz aggregates, Journal of Structural Geology, 14(2), 145–159, doi:10.1016/0191-8141(92)90053-Y.

Kronenberg, A. K., P. Segall, and G. H. Wolf (1990), Hydrolytic Weakening and Penetrative Deformation Within a Natural Shear Zone, in The Brittle-Ductile Transition in Rocks, edited by A. G. Duba, W. B. Durham, J. W. Handin, and H. F. Wang, pp. 21–36, American Geophysical Union (AGU).

TABLE S1: Grain size data measurements, piezometry calculations and associated errors

Map	Type	Step size	Av. gs all	Av. gs qtz2	Av. gs qtz1	RMS gs qtz2	Stress	# qtz2	RMS subgrain size	# subgrains
		μm	μm	μm	μm	μm	MPa		μm	
3_1	Quartz ribbons*	0.3	4.7	4.1	10.1	5.3±3.4	158±63	725	4.2±2.5	378
7	Quartz ribbons*	0.3	6.2	5.2	12.3	6.7±4.3	136±54	1480	4.5±2.6	1117
12	Quartz ribbons*	0.4	5.4	4.4	10.8	5.2±2.7	160±53	2201	4.6±2.4	1757
8	Undeformed quartz clast	0.3	4.1	3.1	7.0	3.6±1.9	200±65	1074	3.3±1.6	875
14_1	Undeformed quartz clast	0.35	4.8	3.6	9.7	4.4±2.5	178±65	941	4.7±2.6	856
14_2	Undeformed quartz clast	0.35	4.0	3.0	7.8	3.4±1.6	207±62	583	4.4±2.2	331
4	Undeformed quartz clast	0.3	3.7	3.4	7.3	4.1±2.3	186±65	279	2.9±1.2	63
3_2	Quartz fine grained	0.3	2.8	2.5	4.4	2.8±1.2	238±64	675	2.1±0.7	318

*Only non-disaggregated grains

3 The fate of garnet during coseismic frictional heating: The role of thermal shock

Simone Papa[1], Giorgio Pennacchioni[1], Ross J Angel[2,†], Manuele Faccenda[1]

Abstract

Garnet stability in high-grade (deep-seated) pseudotachylytes may be obscured by the peculiar thermo-mechanical properties of garnet. Within garnet-rich high-grade mylonites, the supposedly coeval pseudotachylytes are commonly free or poor of garnet. Based on a study of amphibolite facies mylonite-pseudotachylyte association of the Mont Mary unit (Western Alps) we suggest a general process for garnet disappearance due to thermal shock fragmentation during coseismic frictional heating. We show that garnet has the lowest thermal shock resistance between the host-rock minerals (garnet, plagioclase, quartz, and sillimanite, in an increasing sequence of resistance), and thus underwent extreme comminution leading to total melting within the frictional melt, which was deprived of nuclei for growth of garnet microlites. Our analysis highlights the critical role of thermal shock as a general process in mineral comminution during the initial stages of co-seismic slip preceding (and promoting) extensive frictional melting, though the process remains active during these later stages. Our finding has general implications for establishing the coeval development of pseudotachylytes and mylonites and, therefore, for recognising the evidence of deep earthquakes in exhumed rocks.

3.1 Introduction

Pseudotachylytes are widely interpreted as quenched friction-induced silicate melts produced during seismic fault slip (e.g., Sibson, 1975; Spray, 1995). In the continental crust, pseudotachylytes typically develop near the brittle-ductile transition, at ~10 km depth and ambient temperatures

[1] Department of Geosciences, University of Padova, Via Gradenigo 6, 35131 Padua, Italy
[2] Department of Earth and Environmental Sciences, University of Pavia, Via Ferrata 1, 27100 Pavia, Italy
[†] now at: Istituto di Geoscienze e Georisorse, CNR, Via Gradenigo 6, 35131 Padua, Italy

lower than 300 °C, over a wide range of geological settings (Sibson and Toy, 2006). However, pseudotachylytes can also form under high-grade conditions in the middle to lower continental crust (e.g., Sibson, 1980; Moecher and Steltenpohl, 2009), in eclogite facies rocks (e.g., Austrheim and Boundy, 1994; Scambelluri et al., 2017) and in the lithospheric mantle (e.g. Ferré et al., 2017). Evidence for these deep-seated pseudotachylytes includes: (i) the association and mutual overprinting with high grade mylonites; and (ii) the stability of the same high grade metamorphic assemblages in both pseudotachylyte and mylonite (e.g., Passchier, 1982; Menegon et al., 2017).

Garnet is stable under high-grade conditions for a wide range of bulk rock compositions. Garnet was first reported in eclogite-facies pseudotachylytes within garnet-bearing granulites of the Bergen Arcs (Austrheim and Boundy, 1994) as small eclogitic new grains, euhedral to cauliflower in shape, interpreted to have crystallized from the frictional melt. Garnets with similar shapes, commonly overgrowing small garnet clasts, were reported in other high-grade pseudotachylytes (e.g., Lund and Austrheim, 2003; Steltenpohl et al., 2006; Pittarello et al., 2012).

Despite garnet being abundant and stable in high-grade mylonites, the supposedly coeval pseudotachylytes are frequently devoid of garnet, or garnet is rare. These examples of garnet-bearing pseudotachylytes are commonly associated with garnet-free veins belonging to the same set of structures. Austrheim et al. (1996) observed that the host-rock garnets showed a degree of fragmentation correlated with the distance from the pseudotachylyte within a 2–3 cm thick selvage. Fragmentation and scarcity of garnet clasts within the pseudotachylyte were initially explained by the mechanical comminution of garnet during co-seismic slip (Austrheim et al., 1996). Pulverization and co-seismic loading due to earthquake rupture propagation has also been invoked to explain extensive mineral comminution (Trepmann and Stöckhert, 2002; Reches and Dewers, 2005; Austrheim et al., 2017). However, a few authors (Spray, 1992; Hirose and Shimamoto, 2005) have proposed thermal shock as a possible cause of comminution in seismic faults, in addition to purely mechanical wearing or seismic loading, and this hypothesis has been supported by a few physical experiments (Moore and Sibson, 1978; Passelègue et al., 2016). To what extent this process is active in natural seismic faults has not been investigated.

In this chapter, we analyse the disappearance of garnet in amphibolite-facies pseudotachylytes associated with coeval garnet-rich mylonites of the Mont Mary unit, Western Alps. We show that

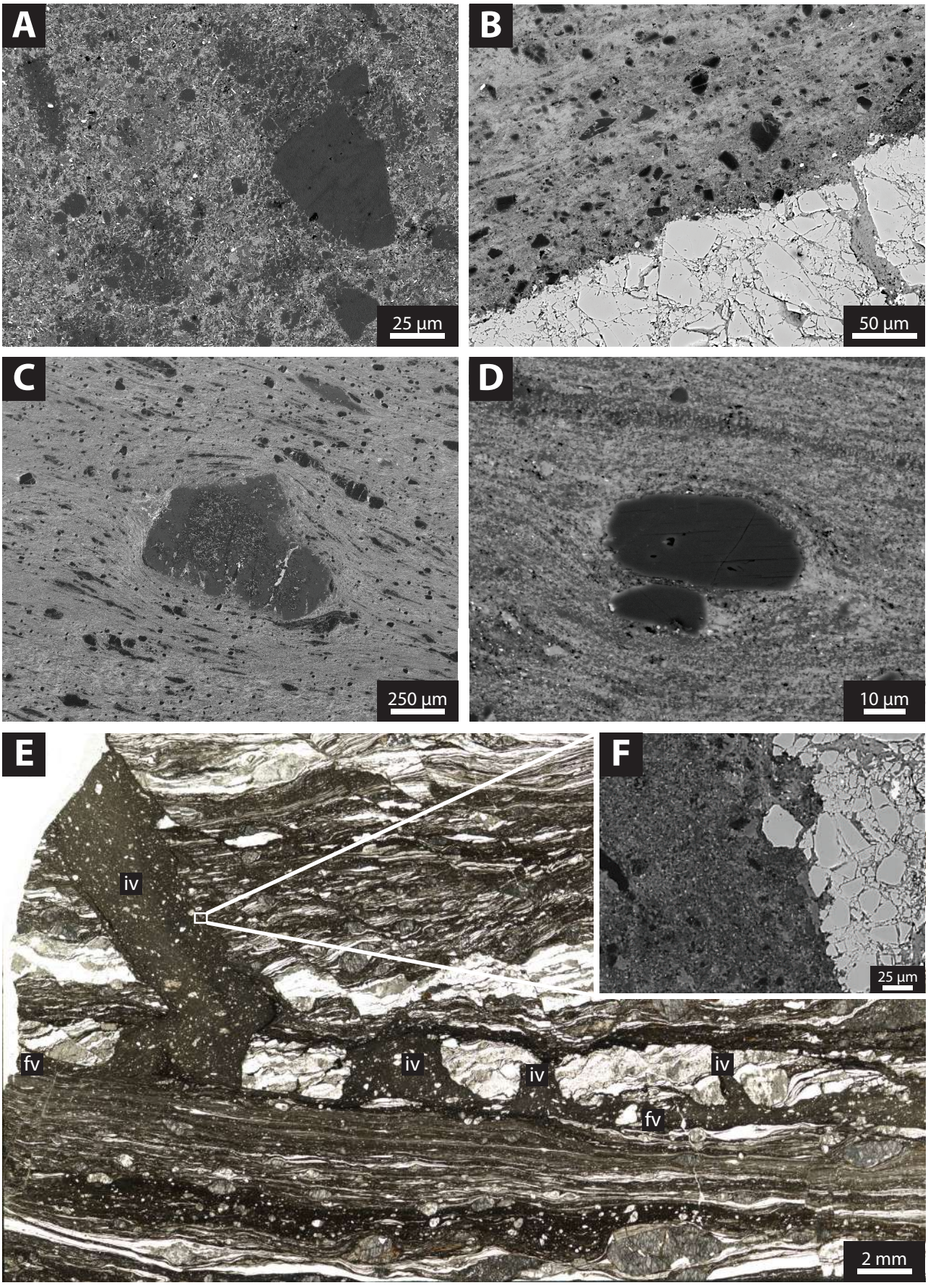
A
25 µm
B
50 µm
C
250 µm
D
10 µm
E
iv
fv
iv
iv
iv
fv
2 mm
F
25 µm

Figure 3. 1 (A) clouds of fine grained fragmented quartz (black), within the pseudotachylyte matrix, still locally surrounding larger clasts. B) In-situ fragmented garnet (lower part of the image) at the boundary of a garnet-free pseudotachylyte vein embedding abundant small clasts of quartz and sillimanite (black grains). C) Clast of plagioclase in the foliated matrix of a ductilely sheared pseudotachylyte showing clasts of sillimanite and quartz stretched into the foliation. D) Sillimanite clasts in a foliated pseudotachylyte. E) Foliation-parallel fault vein (fv) and injection veins (iv) of pseudotachylyte overprinting the amphibolite facies foliation of the quartz-biotite-plagioclase-garnet-sillimanite metapelite mylonite. The mylonite is disrupted by a network of micro-fractures (not crosscutting the pseudotachylyte) and is included as lithic clasts in the fault vein. F) In-situ fractured garnet from the wall rock of the pseudotachylyte injection vein. Note the absence of garnet clasts within the vein as in (B). All photographs are SEM backscattered images except (E) (optical image; plane parallel light).

selective preservation of the host rock minerals as clasts in the pseudotachylytes depends on differences in thermal shock resistance during frictional heating, with garnet having a very low resistance which leads to extreme comminution and total melting. The inferred mechanism of garnet disappearance can be generalized to any pseudotachylyte and, in the case of deep earthquakes, explains the commonly reported scarcity of garnet in many pseudotachylytes where it should be stable.

3.2 Mont Mary mylonites and pseudotachylytes

The pseudotachylyte-hosting mylonites of the Mont Mary unit derived from coarse grained, amphibolite facies metapelites and consist of quartz + garnet + sillimanite + biotite + plagioclase ± muscovite ± K-feldspar ± ilmenite ± graphite which record deformation at 510–580 °C and 0.25–0.45 GPa (Pennacchioni and Cesare, 1997). Garnet, plagioclase, and sillimanite occur as elliptical- to fish-shaped porphyroclasts, while quartz forms monocrystalline ribbons and fine-grained recrystallized layers. Thin (commonly a few millimeters thick) pseudotachylyte fault veins occur along the mylonitic foliation, with small sub-orthogonal injection veins (Fig. 3.1). Pseudotachylytes are everywhere hosted in garnet-bearing mylonites derived from garnet-bearing metapelites. These veins are associated with a locally pervasive network of micro-faults and thin cataclasites. The pseudotachylytes are either undeformed or overprinted by ductile strain (Fig. 3.2A). The coeval development of pseudotachylytes and mylonites is suggested by the small recrystallized grain size (2-8 μm) of quartz in mylonites, compatible with high differential stresses expected at the base of the seismogenic zone (Fitz Gerald et al., 2006), and by survival (stability) of sillimanite and andesine (An_{35}) clasts in the pseudotachylyte (Fig. 3.1C-D). Retrograde epidote and chlorite only occur as a static overprint of the high-grade minerals.

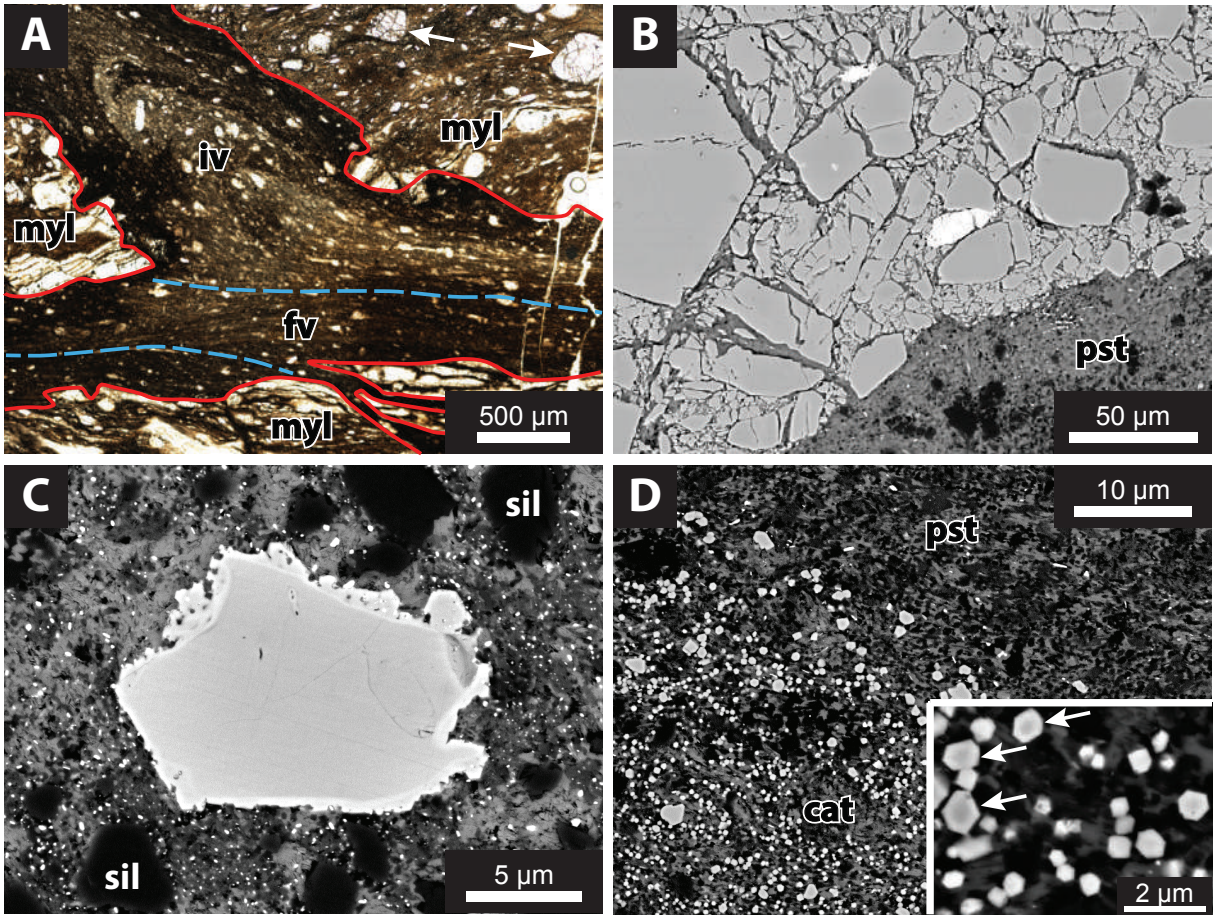

Figure 3. 2 Microstructures of the Mont Mary (western Alps) pseudotachylytes. A: Pseudotachylyte fault (fv) and injection vein (iv) (outlined by red line) within a partially cataclastic mylonite (myl). The fault vein is strongly sheared (the foliation is highlighted by the blue dashed lines), while the injection vein is only partially sheared and preserves melt flow structures and dark chilled margins. The host mylonite includes garnet porphyroclasts (white arrows), while garnet is absent in the vein. Optical microphotograph, non-polarized light. B: In situ fragmentation of a host-rock garnet in contact with pseudotachylyte (pst). The matrix between fragments consists of Ti-poor biotite. C: A rare garnet clast within pseudotachylyte overgrown by a faceted rim of a lighter colored (Mn-rich) garnet. Sillimanite clasts (sil) are common in the pseudotachylyte. D: Contact between ultra-cataclasite (cat), rich in micrometric garnet, and pseudotachylyte (pst), completely free of garnet. Inset shows that garnet in the ultra-cataclasite is euhedral and preserves a relic core (slightly darker than the rim) of the host-rock garnet (white arrows). B,C, and D are scanning electron microscopy backscattered images.

The garnet porphyroclasts of mylonites typically show a main set of fractures orthogonal to the foliation and to the garnet elongation. A different style of garnet fracturing is present near both fault and injection pseudotachylyte veins and along cataclastic bands. These garnets show extreme comminution to sub-micrometric grains even when fracturing occurred “in-situ” without any cataclastic flow (Fig. 3.2B). The minimum grain sizes, measured by FEG-SEM, are as small as 150 nm for both the in-situ fractured grains and within cataclasites.

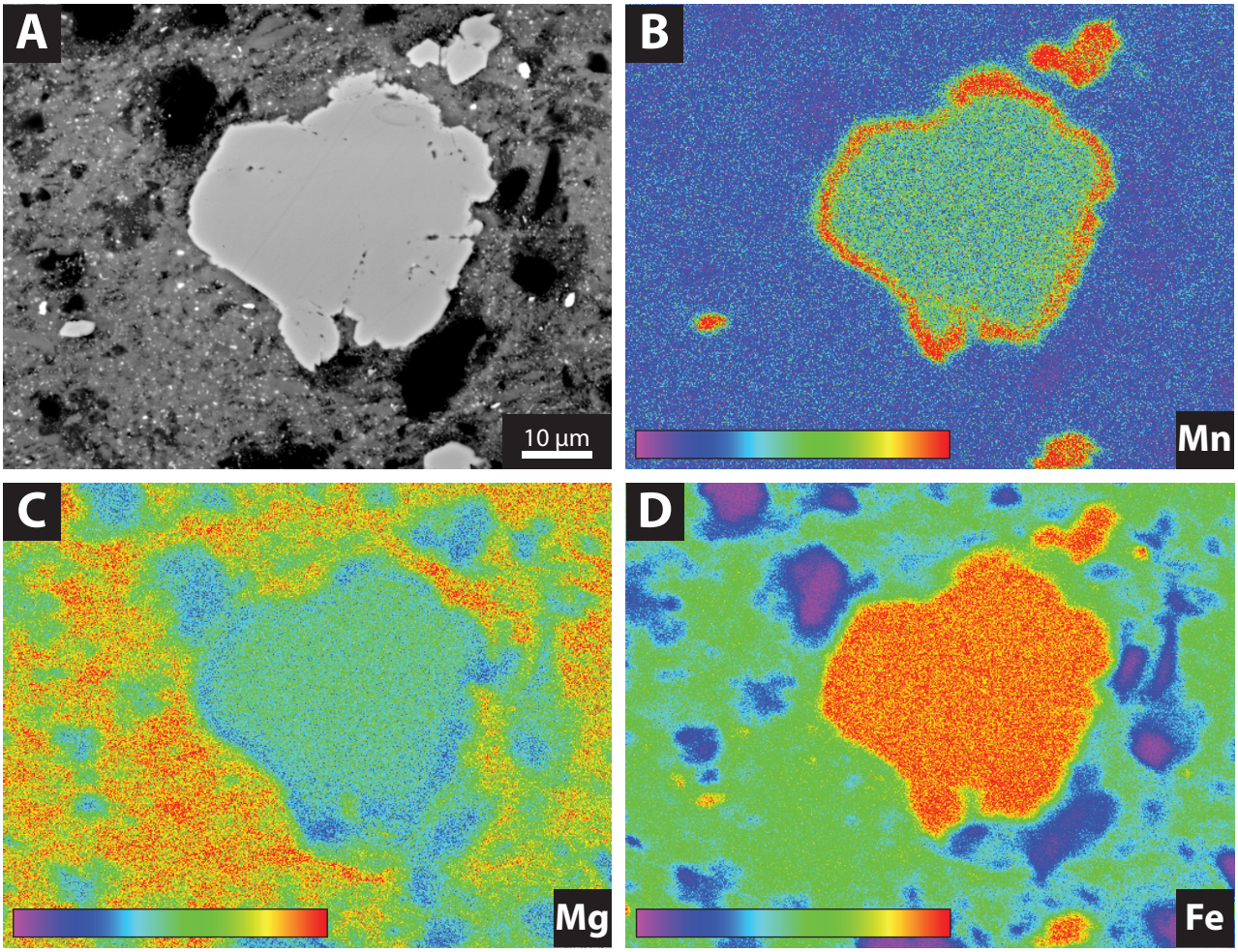

Figure 3. 3 A) BSE image of a garnet clast within the pseudotachylyte matrix showing a bright overgrowth rim. (B)-(D) EDS element maps of the area in (A) for Mn (B), Mg (C), and Fe (D). The element maps show that the garnet rim is characterized by an enrichment in Mn and depletion in Mg and Fe. EDS analysis indicates that Mn varies from 1-2 weight % in the core of the garnet clast, to as much as 5 weight % in the rim.

In the pseudotachylytes, clasts mostly consist of quartz, plagioclase, and sillimanite. Sillimanite occurs as prismatic grains apparently unaffected by fracturing in most cases. Both quartz and plagioclase clasts are usually surrounded by a cloud of fine grained small (down to ca. 1 µm) fragments (Fig. 3.1A). Garnet occurs as very rare small angular clasts, showing a thin lighter colored rim in BSE-SEM images due to Mn enrichment and Mg depletion (Fig. 3.3) associated with the development of crystal facets (Fig. 3.2C), featuring an incipient dendritic overgrowth.

Cataclasites, bounding or paralleling pseudotachylyte fault veins, are distinguished from pseudotachylyte by the presence of abundant garnet clasts (Fig. 3.1D). Adjacent to pseudotachylyte, garnet clasts in cataclasite are extremely fine grained. FEG-SEM imaging of ultra-cataclasites shows that the small (mostly in the range between 250 nm and 1 □m in size) garnets are euhedral, but still have a relict core of the host rock garnet (Fig. 3.1D).

3.3 Thermal stress

A solid suddenly heated (or cooled) at the surface, develops an internal temperature gradient resulting in thermal stress. This stress is a function of the material thermal (expansion coefficient α, conductivity *k*, and diffusivity κ) and elastic properties, of the body shape, and of the process of heat transfer (e.g., conduction, convection). In a semi-infinite medium, the highest thermal stress is compressive at the heated surface (*x-y plane*) and decreases in the direction orthogonal to the surface (*z*) (e.g., Wang et al., 2015) to vanish over a distance on the order of the thermal diffusion distance $\sqrt{\kappa t}$ (≤1 mm for common minerals at seismic heating rates). The relevant material properties for the rock-forming minerals of the high-grade metapelite considered here (quartz, plagioclase, garnet, and sillimanite) are reported in Table 3.1 for the temperature (500 °C) of mylonite and pseudotachylyte formation.

We modeled the thermal stress distribution in an elastic semi-infinite solid medium with a constant surface heat flux due to frictional heating. The temperature distribution is given by (Turcotte and Schubert, 2002: Equation 4–238):

$$\frac{\partial T}{\partial z} = -\frac{q_0}{k} erfc\left(\frac{z}{2\sqrt{\kappa t}}\right), \quad (3.1)$$

where q_0 is the heat flux at the surface given by $q_0 = u\,\tau$, being u the slip velocity and τ the seismic stress drop (Turcotte and Schubert, 2002: Equation 4–243). Equation (3.1) is solved by assuming $T(z,t) = T_i$ when $z \to \infty$, where T_i is the initial temperature. In a fully confined (constant volume) material, the temperature increase causes the pressure in the mineral to increase along its isochor, defined in terms of the volume expansivity α_V and isothermal bulk modulus K_T, as $\frac{\partial P}{\partial T} = \alpha_V K_T$. Ignoring the coherency between adjacent volumes of the material along the temperature gradient, we estimated the transient thermally-induced isotropic stress $p_{th}(z,t)$, associated with the temperature distribution $T(z,t)$, as the thermal pressure increase along the isochor from the initial conditions:

$$p_{th}(z,t) = \int_{T_i}^{T(z,t)} \alpha_V K_T dT. \quad (3.2)$$

For garnet, plagioclase and sillimanite, which have no phase transitions in the relevant temperature range, the isochors are almost linear and parallel (Fig. 3.4), so $\alpha_V K_T$ is effectively constant and Equation (2) becomes:

$$p_{th}(z,t) = \alpha_V K_T[(T(z,t) - T_i)]. \quad (3.3)$$

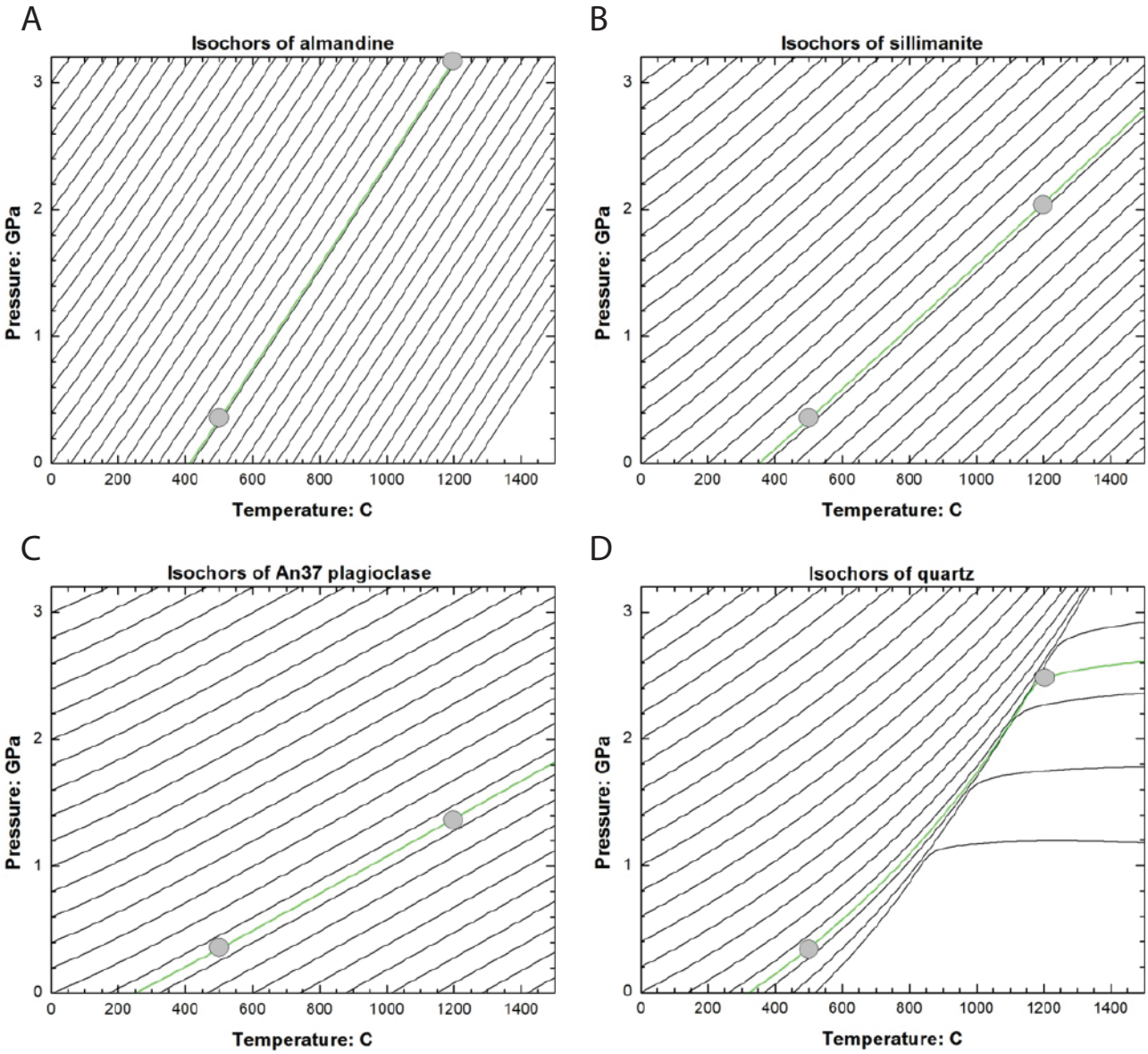

Figure 3. 4 Isochors of (A) almandine garnet, (B) An37 plagioclase, (C) sillimanite, and (D) quartz for the relevant temperature range of 500-1200 °C. The black lines are isochors drawn at 0.2 GPa intervals at 0 °C. The green line is an isochor passing through the estimated initial conditions of 0.35 GPa at 500 °C. The two grey circles illustrate how to calculate the thermal pressure due to heating at constant volume (i.e. zero strain of a completely constrained mineral). If the original conditions are 500 °C and 0.35 GPa, then shock heating to 1200 °C with no volume change raises the pressure along the isochor to about 3.15 GPa for garnet. The thermally-induced pressure change is thus 2.8 GPa. For the same starting point the thermal pressure generated by shock heating to 1200 °C at constant volume for An37 plagioclase is only 1.0 GPa, much less than garnet, because the isochors are shallower (primarily because plagioclase is much softer than garnet). The isochors of sillimanite have steeper slopes than those of plagioclase, primarily because sillimanite has a significantly higher bulk modulus. The isochors of quartz α are steeper than feldspar, but less steep than garnet, but the isochors are flat in quartz β because its thermal expansion is almost zero. As a consequence, the thermal pressure for shock heating is 2.1 GPa for our example. Data sources are listed in detail in the supplementary material.

For quartz, showing a phase transition (α to β) in the relevant temperature range, the isochors are very nonlinear (Fig. 3.4) and the integral of Equation (3.2) has to be calculated explicitly from the equation of state parameters. Calculations show that frictional heating from 500°C (taken as initial

temperature) to 1200 °C (frictional melting temperature) produces thermal stresses on the order of gigapascals over a timescale of few tens of milliseconds (Fig. 3.5). Garnet builds up the highest thermal stress by far (2.8 GPa), followed by quartz (2.1 GPa), sillimanite (1.7 GPa), and plagioclase (1.0 GPa). The timescale does not influence the peak stress, but strongly affects pressure gradients: minerals with low thermal conductivity and diffusivity build up high pressure gradients with maximum values at the surface of as much as 25 GPa/mm for garnet (Fig. 3.5B).

3.4 Thermal shock resistance

A material undergoing hot shock fails at the surface, where the maximum stress is attained. At very high strain rates the mechanical behavior of minerals is dominated by the fracture toughness (Spray, 1992) and failure occurs when the maximum stress intensity factor K_{max} attains the fracture toughness value K_C. An extensive literature has attempted at establishing representative parameters of the *resistance to thermal stress R* for any specific material. By analogy with Kingery (1955), *R* can be defined as:

$$R = k\sigma_f \frac{\Delta T}{\sigma}, \quad (3.4)$$

where σ is the stress at the surface, related to temperature increase ΔT, and σ_f represents the strength of the material, here represented by its fracture toughness K_C (e.g., Lu and Fleck, 1998). Substituting $p_{th}(z,t)$ from Equation (3) for σ into Equation (4), *R* becomes:

$$R = kK_C \frac{\Delta T(z,t)}{p_{th}(z,t)}. \quad (3.5)$$

For minerals with linear isochors, where $\alpha_V K_T$ is effectively constant over the range of temperature ΔT, *R* can be simplified as $kK_c/\alpha_V K_T$. The *resistance to thermal stress* of the above listed minerals, calculated by Equation (3.5) for a ΔT of 700 °C, is reported in Table 3.1. Garnet has the lowest resistance to thermal stress, followed by plagioclase, quartz and sillimanite in an increasing sequence of resistance.

The estimate of the thermal shock resistance by Equation (3.5) has the great advantage that, for minerals with nonlinear isochors such as quartz heated across the α-β transition (Fig. 3.4), the temperature-dependence of the elastic properties is considered in the calculation. On the other hand, our analysis includes some simplifications. One is the assumption of isotropic physical properties, which is a reasonable approximation for garnet, but not for quartz, plagioclase, and sillimanite. For strongly anisotropic materials, the thermal stress is likely higher than that calculated

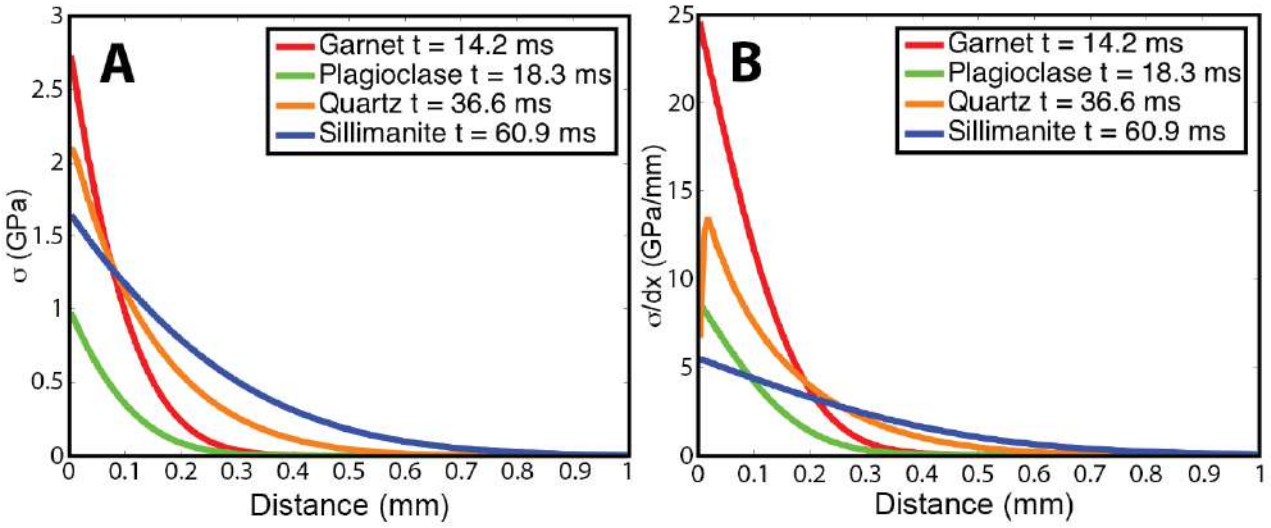

Figure 3. 5 Calculated distribution of pressure (A) and pressure gradient (B) across a 1-mm-thick section of each mineral at time t (shown in the legend) at which the surface reaches 1200 °C. The heat flux at the surface q0 is considered to be constant and equal to 10 MW m^{-2}. The complete list of input parameters and source references is given in the supplementary material.

above and the resistance is lower (Ishihara et al., 2002). Another parameter not considered here is grain size. The thermal shock resistance of materials is significantly reduced for large sizes (e.g., Wang and Li, 2013) and it has been observed that intracrystalline fracturing is dominant in the coarser grained material and intercrystalline disaggregation in the finer one (Moore and Sibson, 1978). An additional source of thermal stress, such as the thermo-mechanical mismatch between adjacent minerals (e.g., Fredrich and Wong, 1986), is also not considered in our model.

3.5 Discussion

Within the Mont Mary amphibolite facies pseudotachylytes, different minerals show different survival rates as clasts within the frictional melt. The survival of clasts of sillimanite, quartz, plagioclase, and garnet (in a decreasing sequence of abundance in the pseudotachylyte) cannot be simply explained by their melting temperature (e.g. Ferré et al., 2017) or by their mechanical properties, but reflects their thermal shock resistance. This resistance depends on the combination of thermo-elastic and mechanical properties as indicated by the model. Thermal shock resistance is critical in defining the hierarchy of frictional melting susceptibility since the most comminuted clasts preferentially disappear by total melting.

The role of thermal stresses in wear of sliding surfaces has been extensively studied in ceramics (e.g., Ting and Winer, 1989). For geological materials, Moore and Sibson (1978) proposed that

transient temperature and thermal gradients, produced during seismic slip, promote cracking as a result of thermally-induced stress. Spray (1992) included thermal shock as one of the processes that lead to comminution and predispose rocks to frictional melting, but he did not report evidence for this process in fault rocks. Studying acoustic emissions during high velocity friction experiments, Passelègue et al. (2016) inferred the occurrence of thermal cracking, but only after initiation of melting. These authors assumed, following Fredrich and Wong (1986), that thermal cracking was due to thermal expansion mismatch between adjacent minerals and did not considered the effect of thermal shock. In contrast, our model considers thermal shock during frictional heating and solid-solid heat conduction without requiring the presence of a melt. Our analysis implies that the thermal shock-induced fragmentation is highly efficient during the very incipient stages of co-seismic slip and plays a major role in comminution that precedes significant frictional melting. Thermal cracking probably also occurs after the formation of a frictional melt, as indicated by in-situ shattering of garnet in contact with pseudotachylyte injection veins (Fig. 3.1). The development of a frictional melt should, however, dramatically change the heat transfer mode and reduce the temperature gradients. High-velocity rock friction experiments conducted in rotary shear apparatus, show that melt droplets start to form at the very initial stages at stress peak after few milliseconds and small amounts of slip (Violay et al., 2014). In such a short time, thermal shock exercises the maximum effect and predisposes the rock to melt by extreme comminution and increase of reactive surface area. Our finding supports the idea that thermal fragmentation is an important process of grain-size reduction that foreruns and promotes frictional melting.

3.6 Conclusions

Thermal shock, induced by frictional heating during an earthquake, represents a major mechanism of selective comminution of rock-forming minerals during the very initial stages of co-seismic slip along a fault. In addition to minerals with low melting temperatures (e.g., biotite, hornblende) frictional melting preferentially affects minerals with low thermal shock resistance (e.g., garnet) that undergo extreme comminution. The composition and physical properties (e.g., viscosity) of frictional melts, the grain size distribution and type of survival clasts, as well as the degree of melting, therefore depend on the thermo-elastic properties of the host rock minerals of a fault and do not reflect solely either the thermal or the mechanical properties. Incorporation of these bulk

mineral properties into models of frictional heating and melting could probably better explain natural observations from pseudotachylyte-bearing faults.

SUPPLEMENTARY MATERIAL FOR CHAPTER 3

Complete list of input thermo-elastic parameters and source references

TABLE 3.1. MINERAL PROPERTIES USED FOR CALCULATIONS

Property	**Almandine**	**An37 plagioclase**	**Quartz**	**Sillimanite**
Room T, room p				
Kc (MPa m$^{1/2}$)	1.31[(1)]	0.75[(1)]	1.50[(2)]	1.60[(2)]
ρ (Kg m^{-3})	4318[(3)]	2700[(3)]	2650[(3)]	3250[(3)]
500°C, room p				
k (W m^{-1} K^{-1})	1.58[*]	1.60[(4)]	3.05[(5)]	3.64[†(6)]
κ (m^2 s^{-1} x 10^{-6})	0.68[(7)]	0.54[§]	0.98[§]	1.17[§]
C_p (J mol^{-1} K^{-1})	463[(8)]	1100[(7)]	1180[(7)]	1130[(7)]
500°C, 0.35 GPa				
K_T (GPa)	163.9[(9)]	67.0[(10,11,12)]	30.1[(13)]	160.4[(14)]
α_V (K^{-1} x 10^{-5})	2.44[(9)]	2.13[(10,11,12)]	6.81[(13)]	1.48[(14)]
p_{th} to 1200°C (GPa)	2.83[#]	1.02[#]	2.12[#]	1.70[#]

[*] Calculated from diffusivity (κ).

[†] Data of k at 500°C are not available for sillimanite. k decreases with increasing T in silicates (except for feldspars). We consider a decrease of 60% from room temperature to 500°C, similar to those of garnet and quartz.

[§] Calculated from conductivity (k).

[#] Calculations performed with EosFit7c[15].

[(1-15)] Source references: see list below

1. Tromans, D., and Meech, J. A., 2002, Fracture toughness and surface energies of minerals: theoretical estimates for oxides, sulphides, silicates and halides: *Minerals Engineering*, v. *15*, p. 1027-1041.
2. Whitney, D. L., Broz, M., and Cook, R. F., 2007, Hardness, toughness, and modulus of some common metamorphic minerals: *American Mineralogist*, v. *92*, p. 281-288.
3. Deer, W.A., Howie, R.A., Zussman, J., 1992, An introduction to the rock forming minerals. Second Edition: Longman Group UK Limited, London.
4. Birch, A. F., and Clark, H., 1940, The thermal conductivity of rocks and its dependence upon temperature and composition: American Journal of Science, v. 238, p. 529-558.
5. Kanamori, H., Fujii, N., and Mizutani, H., 1968, Thermal diffusivity measurement of rock-forming minerals from 300 to 1100 K: Journal of geophysical research, v. 73, p. 595-605.
6. Horai, K. I. (1971). Thermal conductivity of rock-forming minerals: Journal of Geophysical Research, v. 76, p. 1278-1308.

7. Robie, R. A., and Waldbaum, D. R., 1968, Thermodynamic Properties of Minerals and Related Substances at 298.15° K (25.0° C) and One Atmosphere (1013 Bars) Pressure and at Higher Temperatures: U.S. Geological Survey Bulletin, v. 1259, p. 256.
8. Bosenick, A., Geiger, C. A., and Cemič, L., 1996, Heat capacity measurements of synthetic pyrope-grossular garnets between 320 and 1000 K by differential scanning calorimetry: Geochimica et Cosmochimica Acta, v. 60, p. 3215-3227.
9. Milani, S., Nestola, F., Alvaro, M., Pasqual, D., Mazzucchelli M. L., Domeneghetti, M. C., and Geiger, C., 2015, Diamond–garnet geobarometry: The role of garnet compressibility and expansivity: Lithos, v. 227, p. 140-147.
10. Johnson, E., 2007, The Elastic Behavior of Plagioclase Feldspar at High Pressure [MSc thesis]: Blacksburg VA, Virginia Polytechnic Institute and State University, 115 p.
11. Tribaudino, M., Angel, R. J., Camara, F., Nestola, F., Pasqual, D., and Margiolaki, I., 2010, Thermal expansion of plagioclase feldspars: Contributions to Mineralogy and Petrology, v. 160, p. 899-908.
12. Tribaudino, M., Bruno, M., Nestola, F., Pasqual, D., and Angel, R. J., 2011, Thermoelastic and thermodynamic properties of plagioclase feldspars from thermal expansion measurements: American Mineralogist, v. 96, p. 992-1002.
13. Angel, R. J., Alvaro, M., Miletich, R., and Nestola, F., 2017, A simple and generalised P–T–V EoS for continuous phase transitions, implemented in EosFit and applied to quartz: Contributions to Mineralogy and Petrology, v. 172, p. 29.
14. Holland, T. J. B., and Powell, R., 2011, An improved and extended internally consistent thermodynamic dataset for phases of petrological interest, involving a new equation of state for solids: Journal of Metamorphic Geology, v. 29, p. 333-383.
15. Angel, R. J., Gonzalez-Platas, J., and Alvaro, M., 2014, EosFit-7c and a Fortran module (library) for equation of state calculations: Zeitschrift für Kristallographie, v. 229, p. 405-419.

4 Experimental frictional melting of garnet-bearing ultramylonites

Simone Papa[1], Elena Spagnuolo[2], Giorgio Pennacchioni[1], Giulio Di Toro[1], Andrea Cavallo[3]

Abstract

We performed 4 rotary-shear high-velocity frictional experiments on the Mont Mary (ultra)mylonites, at room pressure and humidity, in order to reproduce the natural pseudotachylytes studied in the previous chapters. The aims of the study were to evaluate the effects of varying slip acceleration in the experiments and to compare the relative preservation of host-rock clasts within the melt in experimental and natural pseudotachylytes. The results suggest that slip acceleration has a strong control on the peak of frictional strength at the onset of sliding, while once weakening occurs the friction drop observed is independent from initial acceleration. We observed that the experimental melt shows the same hierarchy of frictional melting susceptibilities of host-rock minerals observed in nature. The preservation of host-rock minerals is controlled by their melting temperature and thermal shock resistance.

4.1 Introduction

Pseudotachylytes are quenched friction-induced silicate melts produced during coseismic fault slip (e.g., Sibson, 1975; Spray, 1995). Frictional melt is the result of conversion of mechanical deformation to heat under adiabatic conditions, i.e. conditions in which heat is accumulated faster than it is dissipated (Spray, 2010). Experimental and natural evidence shows that the development of a continuous film of melt wetting the sliding surface can lubricate faults during earthquakes (Di Toro et al., 2006). At high slip velocity (> 0.1 ms^{-1}) frictional melting occurs in milliseconds (Violay et al., 2013), through a disequilibrium process, different from partial melting in igneous processes.

[1] Department of Geosciences, University of Padova, Via Gradenigo 6, 35131 Padua, Italy
[2] Istituto Nazionale di Geofisica e Vulcanologia, Via di Vigna Murata, Rome, Italy
[3] CERTEMA, Cinigiano (GR), Italy

Melting proceeds according to the individual melting point of minerals and complete melting of the host rock is generally not achieved (Spray, 1987; Maddock, 1992; O'Hara, 1992). It is widely accepted now that the first stage of the frictional melting process is comminution (Spray, 2010 and references therein). Comminution, by reducing particle grain size, causes growth of the surface area of particles and facilitates frictional melting. Comminution results from the processes of abrasive wear and thermal shock (Spray, 1992), and is controlled by the thermo-mechanical properties of individual minerals. Spray (1992, 2010) proposed that minerals more susceptible to comminution are those with low values of fracture toughness and resistance to thermal shock. Minerals preferentially comminuted are then more quickly removed from the frictional melt, if the temperature exceeds their melting point. Papa et al. (2018) proposed a simplified formula to estimate the thermal shock resistance of minerals and showed that the relative thermal shock resistance of host-rock minerals could explain their observed different susceptibility to frictional melting.

Rotary-shear high-velocity frictional testing machines are used to reproduce slip velocities and accelerations that occur during earthquakes (e.g. Shimamoto and Tsutsumi, 1994; Tsutsumi and Shimamoto, 1997; Di Toro et al., 2010). High-velocity frictional experiments allows the collection of mechanical data and the production of artificial pseudotachylytes whose microstructures can be compared to natural samples (e.g. Hirose and Shimamoto, 2005; Di Toro et al., 2010). Here we present preliminary results from an experimental study on (ultra)mylonitic metapelites from the alpine Mont Mary nappe. The experiments were designed to reproduce the natural pseudotachylytes studied in Papa et al. (2018) in order to (i) evaluate the effects on mechanical behaviour and microstructures of varying slip acceleration and slip duration and (ii) compare the relative preservation of host-rock clasts within the melt in experimental and natural pseudotachylytes.

4.2 Material and methods

We performed 4 friction experiments on hollow cilinders (30/50 mm internal/external diametre) of Mont Mary (ultra)mylonites at room pressure and humidity. The experiments were performed with the rotary shear apparatus SHIVA (Slow to High Velocity Apparatus) at the Istituto Nazionale di Geofisica e Vulcanologia in Rome (Di Toro et al., 2010). Mont Mary (ultra)mylonites are rocks layered at the mm scale that contain as major rock-forming minerals quartz, plagioclase, garnet,

sillimanite, and biotite (see Pennacchioni and Cesare, 1997, for an accurate description). Core samples were drilled perpendicular to the mylonitic foliation in order to maximise the chanches that the composition and mineral content of the sliding zone was representative of the bulk of the rock. Bare surfaces were ground flat with a surface grinder to ensure the smallest possible misalignment once the rock specimens are installed on SHIVA. Sample misalignment would cause spurious vibrations which alter the mechanical data or induce sample failure (Nielsen et al., 2012). Samples were then jacketed in aluminum ring and embedded in epoxy as described in Nielsen et al. (2012). Experiments were performed at target slip velocities of 3 ms^{-1}, slip acceleration of either 10 or 40 ms^{-2}, displacements of either 5 or 50 cm, and constant normal stress of 20 MPa. Actual values of normal stress σ_n, axial shortening, equivalent displacement δ, slip velocity V, and shear stress τ were acquired during the experiments at a frequency up to 250 Hz. Further details on the experimental assembly can be found in Di Toro et al. (2010), Niemeijer et al. (2011), and Passelègue et al. (2016). Thin sections cut perpendicular to the slippping zone of post-test samples were analyzed with optical microscope and energy dispersive spectrometer (EDS)–equipped field emission scanning electron microscope (FE-SEM) model MERLIN ZEISS (SEM) at CERTEMA laboratory (Cinigiano, Italy).

Table 4.1 Summary of experimental settings and results. Acronyms and symbols: *a**: target acceleration; τ *max*: peak of frictional strength; τ *min*: minimum of frictional strength; τ *drop*: frictional strength drop between peak and minimum; τ *f* frictional strength at the end of deceleration; *V max*: maximum slip velocity; δ: total slip; *t* = total duration. Normal stress σn = 20 MPa and target velocity = 3 ms^{-1} in all the experiments.

Samples	*a** (ms^{-2})	τ *max* (MPa)	τ *min* (MPa)	τ *drop* %	τ *f* (MPa)	*V max* (ms^{-1})	δ (cm)	*t* (ms)
S1768	40	9.4	5.8	38	7.8	1.97	5.7	58
S1769	10	12.3	5.6	54	6.3	2.82	46.8	320
S1770	10	12.1	6.4	47	7.5	0.94	4.9	114
S1771	40	9.8	4.3	56	7.0	2.83	43.9	215

4.3 Results

4.3.1 Mechanical data

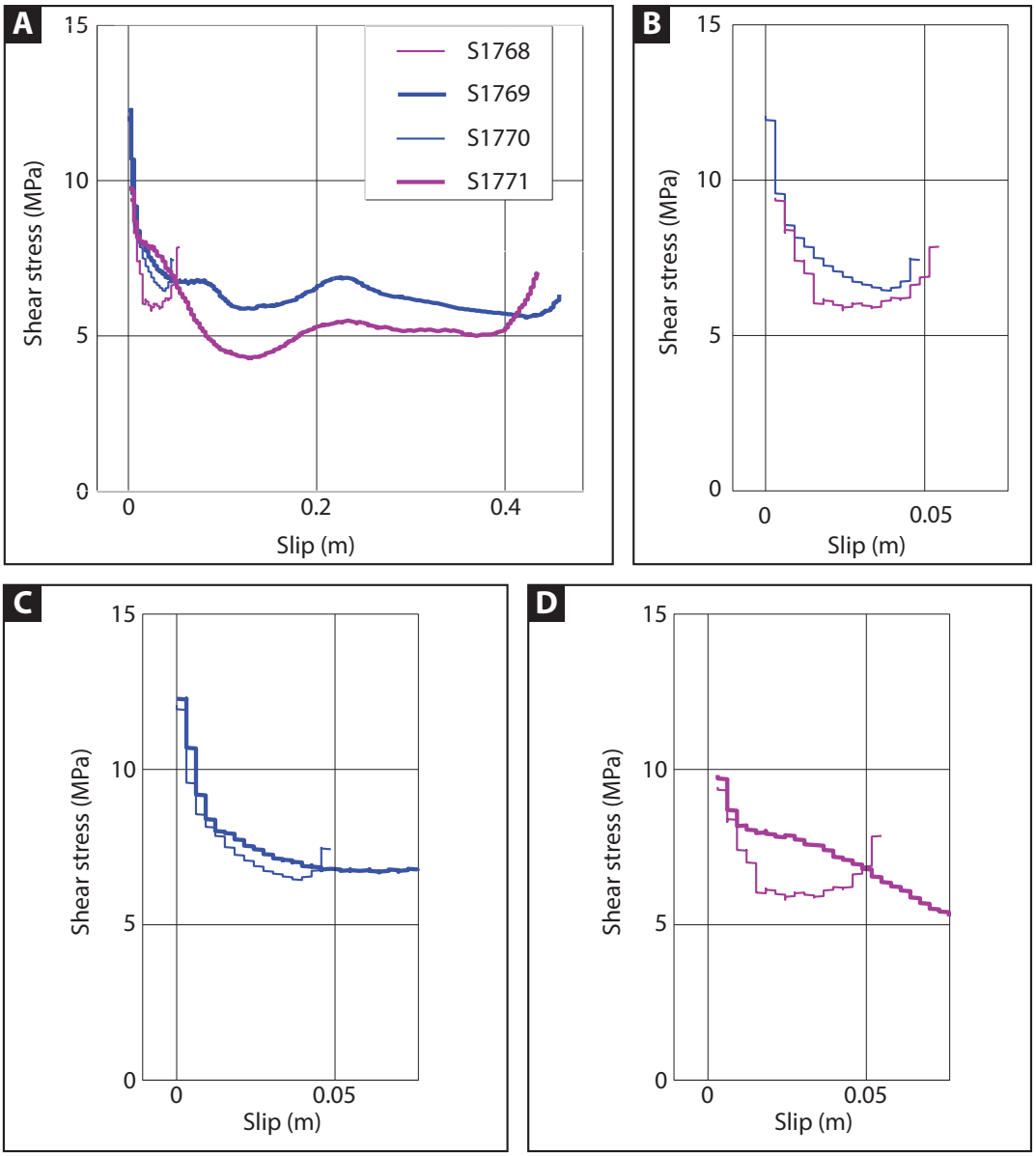

Figure 4.1 Mechanical data for shear stress τ versus slip for the Mont Mary ultramylonites. All experiments were performed at normal stress σ_n = 20 MPa and target velocity of 3 ms^{-1}. Blue lines represent high-acceleration experiments (target acceleration a = 40 ms^{-2}) and magenta lines low-acceleration ones (target acceleration a* = 10 ms^{-2}). Thick lines represent large-displacement experiments ($\delta \sim 50$ cm) and thin lines small-displacement ones ($\delta \sim 5$ cm). A) All the experiments. B) Small-displacement experiments. C) Low-acceleration experiments. D) High-acceleration experiments.*

In figure 4.1 and 4.2 we report the evolution of the shear stress τ with slip and time and the evolution of slip velocity during experiments conducted for different accelerations and total slips. A summary of the relevant mechanical data is reported in Table 4.1. The shear stress τ at constant normal stress (σ_n) approximates the frictional strength during slip. In all the experiments τ increased almost linearly, and with the same slope with respect to time (Fig. 4.2A), up to a peak value (listed in Table 4.1) at the onset of motion. Peak frictional strength depends strongly on the imposed acceleration: the higher the acceleration the lower the friction. Friction initially increases at the

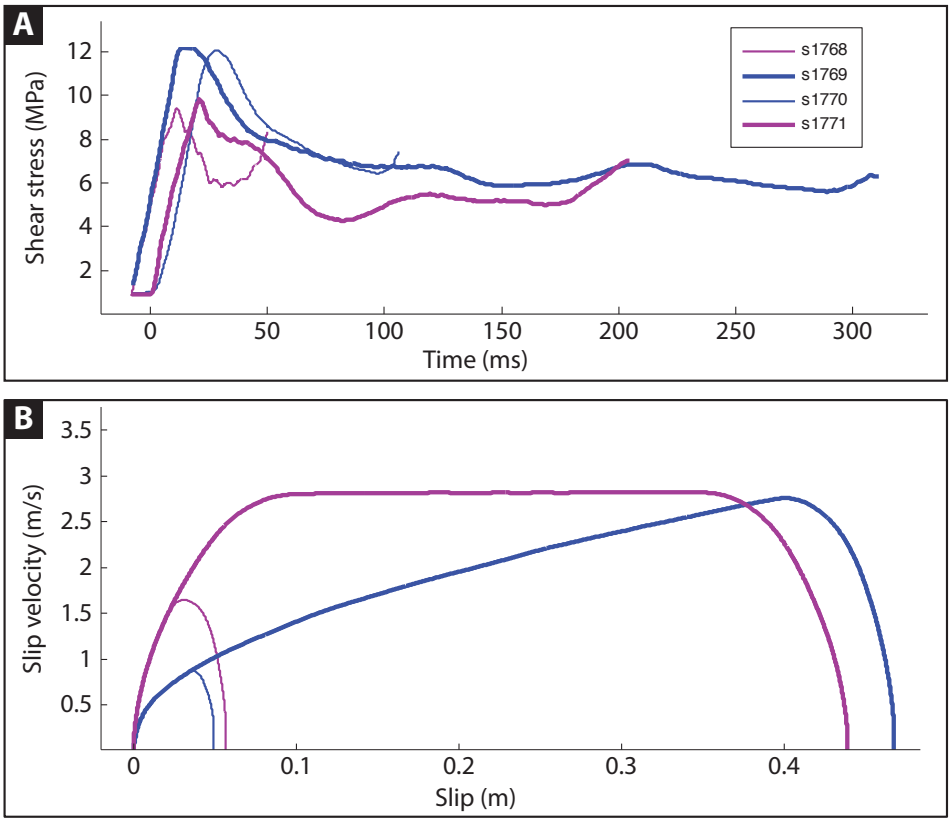

Figure 4.2 Mechanical data for the Mont Mary ultramylonites. A) Shear stress τ versus time (not all the experiments start exactly at time zero). B) Slip velocity versus slip.

same rate for all the experiments, but weakening occurs faster in high-acceleration ones (Fig. 4.2A) causing lower peak values. The couples of experiments with the same acceleration show very similar peaks, approximately 12.2 MPa for low acceleration and 9.6 MPa for high acceleration. The correspondent friction coefficients μ (ratio of shear stress τ and normal stress σ_n) are respectively around 0.6 and 0.5. Immediately after initial peak, shear stress drops abruptly in all the experiments. All experiments but one (S1771), show a friction drop of 35-40 % after circa 1 cm of slip that corresponds to circa 14 ms and 25 ms for the high-acceleration and low-acceleration experiments respectively. At this stage, after 1 cm of slip, slip velocity has reached 1 ms^{-1} and 0.5 ms^{-1}, respectively (Fig. 4.2B). In experiment S1771, after an initial sudden friction drop of 15 % in less than 10 ms, friction decrease continues at a slower rate. After this first stage of abrupt drop, in the small-displacement experiments friction keep decreasing at a slower rate reaching the lowest value before, at the onset of deceleration, it eventually increases to a similar final value of τ for both experiments (7.5-7.8 MPa). In large-displacement experiments, the friction coefficient, after the initial decay, tends to stabilise to a steady-state value after 10 cm of slip, although large oscillations occur. After 10 cm the high-acceleration experiment has already reached the target slip velocity, while the low-acceleration one has a slip velocity around 1.5 ms^{-1}. Minimum τ values are circa 1

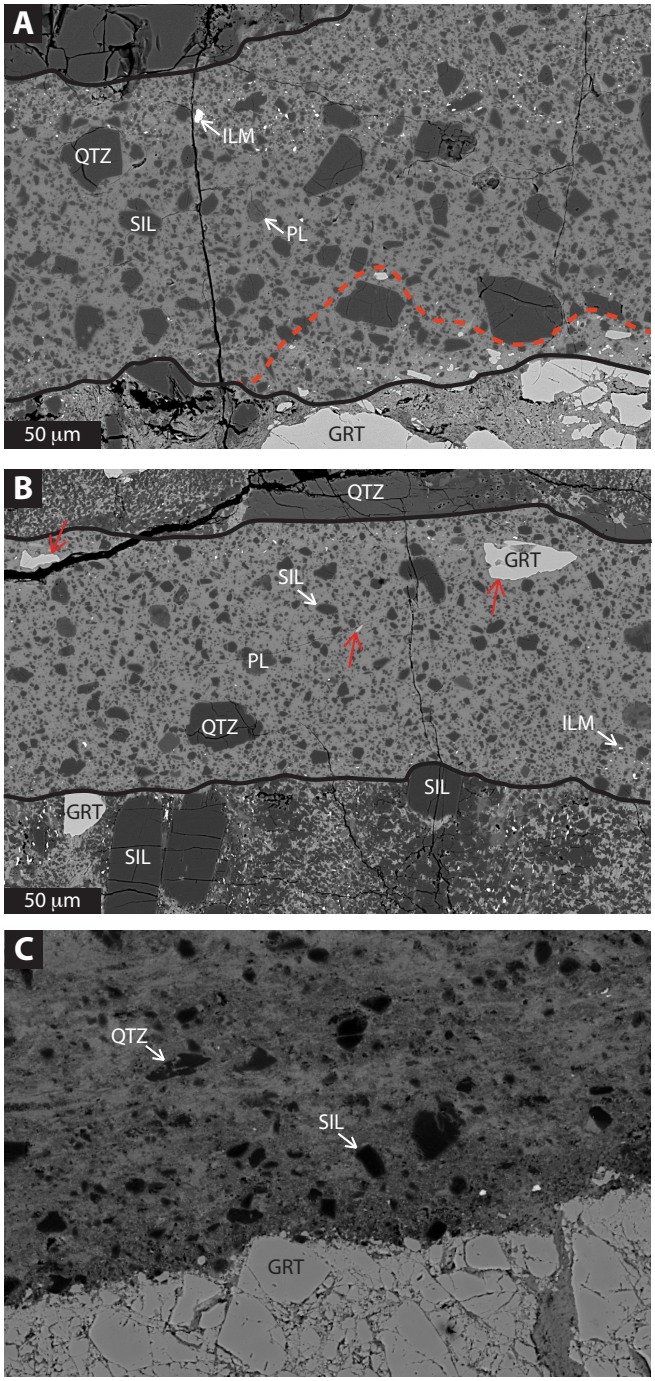

Figure 4.3 Comparison of the microstructures of A) sample S1769, B) sample S1771, and C) natural Mont Mary pseudotachylyte. Melt layers are outlined by black lines. The red dotted line in (A) indicates the area close to the host-rock garnet where small garnet clasts are present within the melt layer. Red arrows in (B) indicate garnet clasts. Note that very bright clasts of oxides (mainly ilmenite) in the experimental samples are widespread toward the border of the vein and almost absent at the centre. SEM-BSE images.

MPa smaller than in small-displacement experiments for the same acceleration. The observed maximum friction drop is the same for the two experiments (55 %), and thus the steady-state shear stress τ is lower for the high-acceleration experiment, that oscillates around 5 MPa ($\mu \sim 0.25$), than for the low-acceleration one (around 6 MPa; $\mu \sim 0.3$). Upon deceleration, τ increases toward final values that are slightly smaller than for the small-displacement experiments.

4.3.2 Microstructures

Here we report microstructures produced during the large-displacement experiments S1771 and S1769. Thin sections were cut perpendicular to the sliding surface of the rotary sides. The two experimental samples show very similar characteristics (Fig. 4.3). In both experiments the two sliding blocks were not welded together, although a continuous film of melt is present on the slip surfaces. In both cases the melt layer is 150-200 μm thick, and locally a thin (< 100 μm) layer of the opposite stationary sample is welded to the rotary sample as a result of adhesive wear (top of Fig. 4.3A-B). The melt layers contain abundant host-rock clasts embedded in a very homogeneous matrix. Percentage of clasts has been measured by image analysis on SEM-BSE images and is between 30-40 % for both samples. Approximately 95% of clasts are made

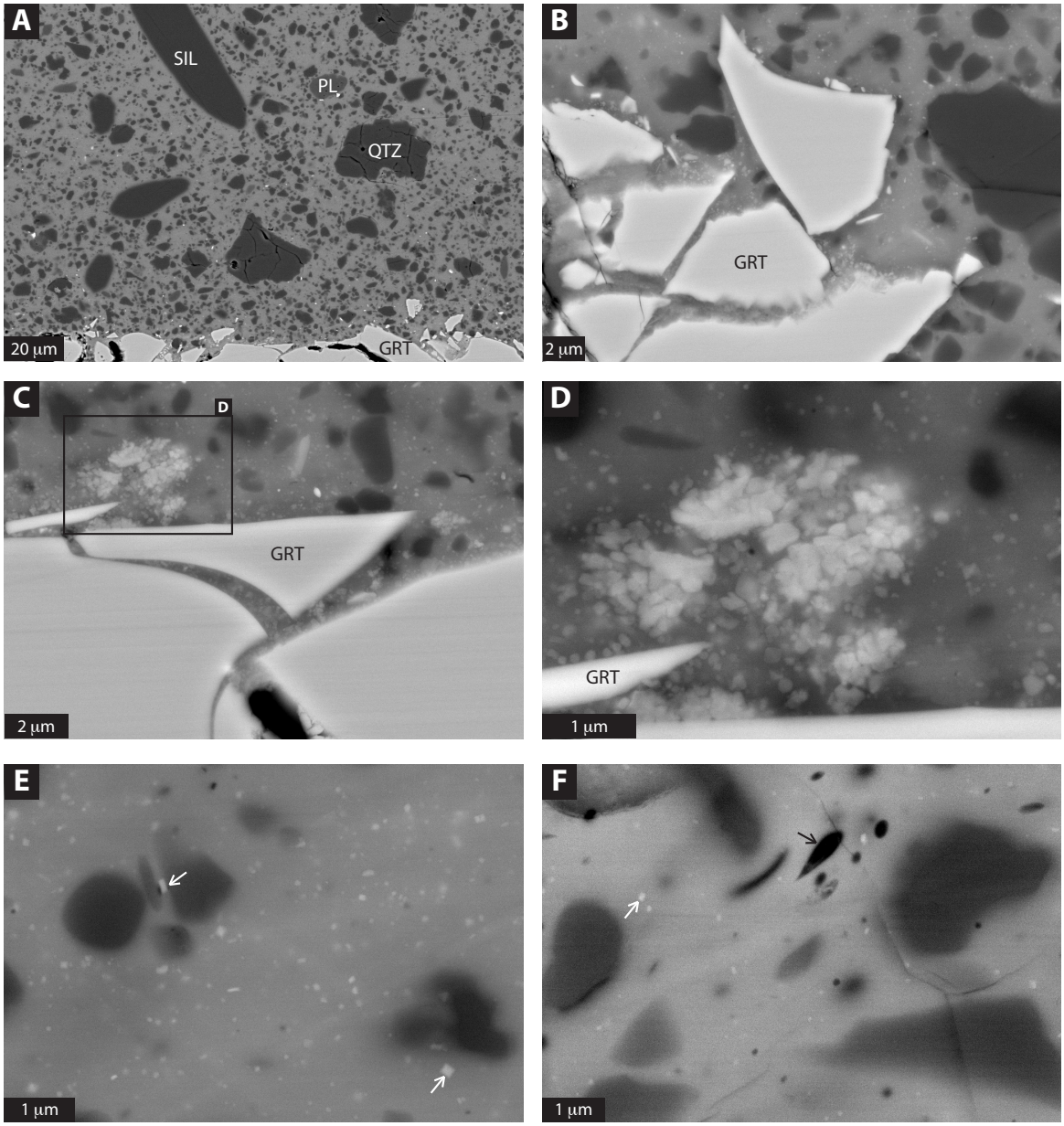

Figure 4. 4 Microstructures of experimental melt layers of sample S1771 (A-D, F) and S1769 (E). A) Melt layer with host-rock garnet at the margin. B-C-D) Details of garnet-melt interfaces. E-F) Details of the melt layer matrix. White arrows indicate microlites, the black arrow a vescicle.

of quartz (~ 55 %) and sillimanite (~ 40 %; see Item S2 in the supplementary material). The remaining consists of plagioclase, rare garnet, and oxides (mainly ilmenite). Garnet clasts can be as large as 50 µm and are generally observed near the border of the melt layer, especially when host-rock garnet is present at the margin (Fig. 4.3A; Fig. 4.4A). Host-rock garnet in contact with the melt, show fragmentation in clasts down to the micrometric scale extremely localised at the border (Fig. 4.4B-C). At the border of the vein, when in contact with host-rock garnet, clusters of clasts with dimensions of few tens or hundreds of nanometers are commonly observed (Fig. 4.4D). Because of the extremely fine grain size, a precise chemical composition of these clasts not contaminated by the surrounding matrix cannot be measured, but by means of ultra-high-resolution EDS

microanalysis we determined that their composition is similar to that of host-rock garnet but strongly depleted in Fe and enriched of Mg (Item S3). Similar to garnet, ilmenite, which is abundant in the host rock as micrometric acicular crystals, is preserved inside the melt layers only toward the boundary, while is totally absent in the centre (Fig. 4.3). The matrix of the melt layer consists mostly of a homogeneous 'glass' whose chemical composition indicates that it resulted from the preferential melting of biotite (Item S4). Vescicles and microlites are present. Microlites have a grain size that generally does not exceed few hundreds of nanometers, locally they seem to have a cubic euhedral shape (Fig. 4.4E-F) and are enriched in Mg, Fe, and Al with respect to the surrounding matrix (Item S1).

4.4 Discussion

Mechanical data show that peak frictional strength has a strong inverse correlation with slip acceleration. This is in disagreement with Niemeijer et al. (2011) that observed no systematic dependence of shear stress on acceleration. In our case, experiments repeated with the same slip acceleration on the same rock type, show a reproducible behaviour, although more experiments are needed for statistical relevance. In high-acceleration experiments, velocity increases faster and thus heat is dissipated in a shorter time causing steeper thermal gradients. After peak shear stress, friction decreases dramatically in all the experiments. Most of total friction drop is already achieved after 1 cm of slip. Violay et al. (2013) observed patches of ropy-like glass features covering the slip surfaces of microgabbro after 5 mm of slip interpreted as the result of flash heating of asperities (Archard, 1959; Rice, 2006). Flash melting of asperities can cause extreme weakening at the onset of slip (Rempel and Weaver, 2008; Brown and Fialko, 2012) and is likely responsible for the initial friction drop in our experiments. The total amount of weakening is not correlated with slip acceleration, since friction drop is similar for all the experiments. After 50 cm of slip the difference in frictional strength in the two experiments with different slip acceleration is not fully recovered yet. The high-acceleration experiment has a "steady-state" friction slightly lower than the low-acceleration one, although no relevant difference in microstructure (e.g. percentage of clasts) was observed.

The hierarchy of frictional melting susceptibilities of host-rock minerals in the experimental samples corresponds to what is observed in nature (Papa et al., 2018). The absence of garnet as well as oxide

clasts in the centre of the melt layer indicates that clasts tend to preferentially melt in the inner part of the veins (e.g. Bizzarri, 2014), where the highest temperatures are attained. The silica content of the glass is much higher than that of biotite and garnet that melted almost completely, suggesting that also quartz (melting point 1730°C; Spray, 2010) experienced melting, at least partially. However, because of the short duration of the heat pulse and low thermal conductivity of minerals, coarse clasts where heated only at the surface and therefore they did not melt completely (Ray, 1999). This highlights the strong influence of selective comminution in melting susceptibilities of minerals.

Extreme comminution of garnet correlated to the distance from pseudotachylyte veins, has been reported by several authors (Austrheim et al., 1996; Austrheim et al., 2017; Papa et al., 2018; Hawemann et al., 2019b; Petley-Ragan et al., 2019). This comminution has been referred to seismic loading (Austrheim et al., 2017; Trepmann and Stöckhert, 2002), dynamic propagation of seismic rupture (Petley-Ragan et al., 2019), or thermal shock (Papa et al., 2018). In the rotary shear experiments neither seismic loading nor dynamic rupture can be invoked and indeed intense wall-rock garnet fragmentation is not observed, except very locally at the host rock/melt vein interface. However, at the experimental conditions (room pressure and room humidity) it has to be expected that heat is dissipated very efficiently and temperature gradients away from the sliding surface are negligible. Along the sliding surface, comminution prior to frictional melting is then due to abrasive wear and thermal shock (Spray, 1992) and preferential disappearance of garnet within the frictional melt can be explained by its low thermal shock resistance (Papa et al., 2018).

Our microstructural analysis is still in a partial state for the lack of observations of the sliding surfaces of small-displacement experiments. The analysis of the product of comminution before extensive melting took place, will help to shed more light on the pathway to frictional melting and on the importance of selective comminution to explain the formation of frictional melts.

4.5 Conclusions

Peak of frictional strength in rotary-shear high-velocity friction experiments strongly depends on slip acceleration. Once friction begins to drop as a result of melting at asperity contacts (flash weakening) the following evolution is largely independent by the initial slip acceleration and, after 50 cm of slip, both microstructures and “steady-state” frictional strength tend to correspond. Within

the frictional melt, the selective preservation of host-rock clasts shows the same hierarchy observed in nature. Minerals that are selectively preserved are those with high melting temperature and high thermal shock resistance (sillimanite and quartz). Minerals with the lowest thermal shock resistance and melting temperature (biotite and garnet) are preferentially comminuted and fused to form the melt.

SUPPLEMENTARY MATERIAL FOR CHAPTER 4

ITEM S1

Semi-quantitative EDS chemical transect of spinel (?) microlite – sample S1771
Microlite enriched in Al-Mg-Fe

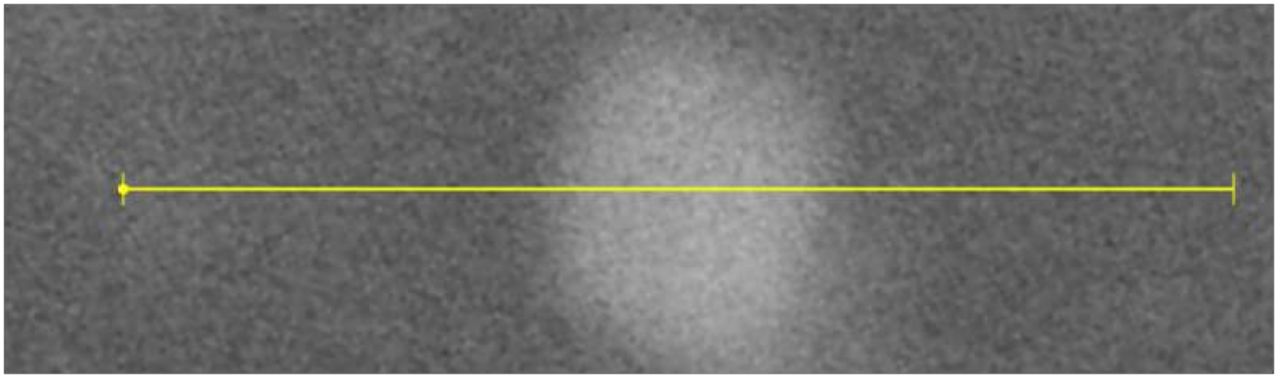

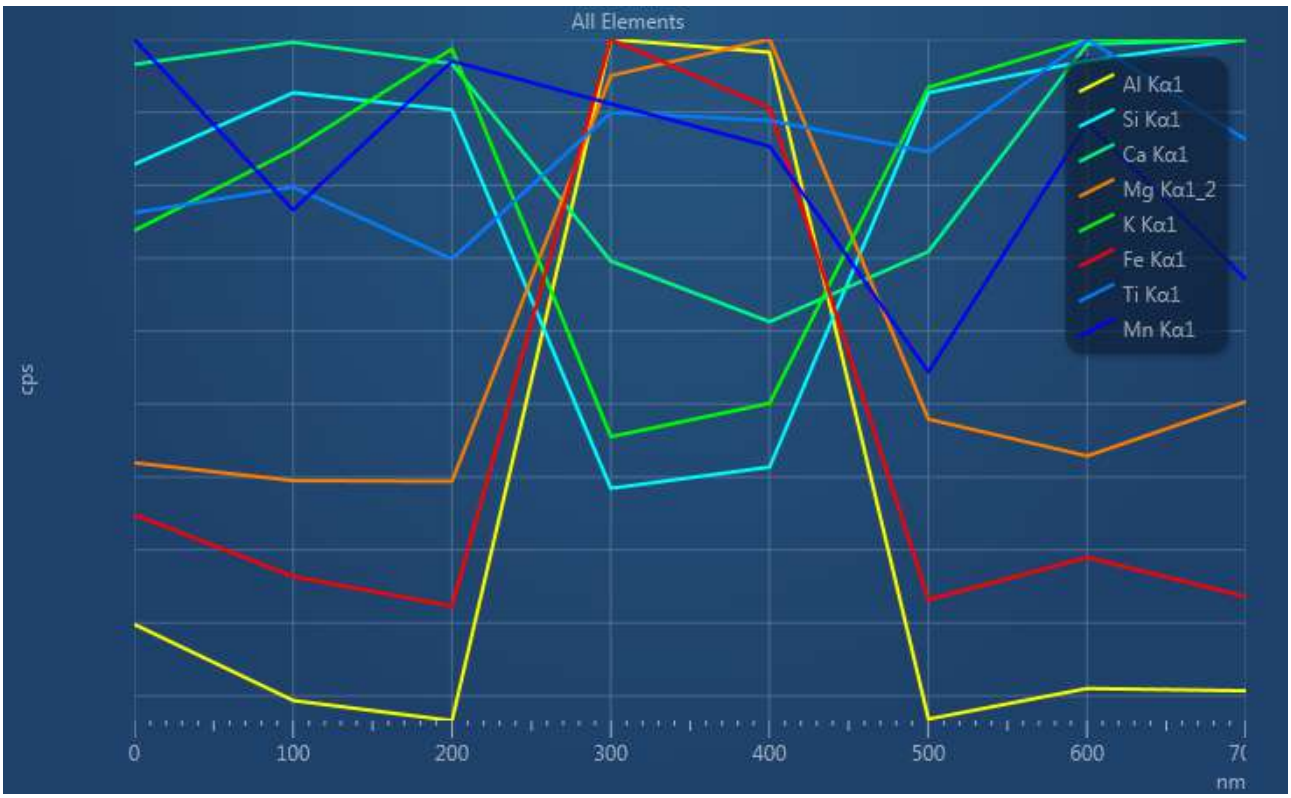

ITEM S2

EDS chemical map of pseudotachylyte S1771 - Map data 2
Bright clasts are: quartz in Si map; sillimanite in Al map; plagioclase in Na map; garnet in Fe map; ilmenite in Ti map.

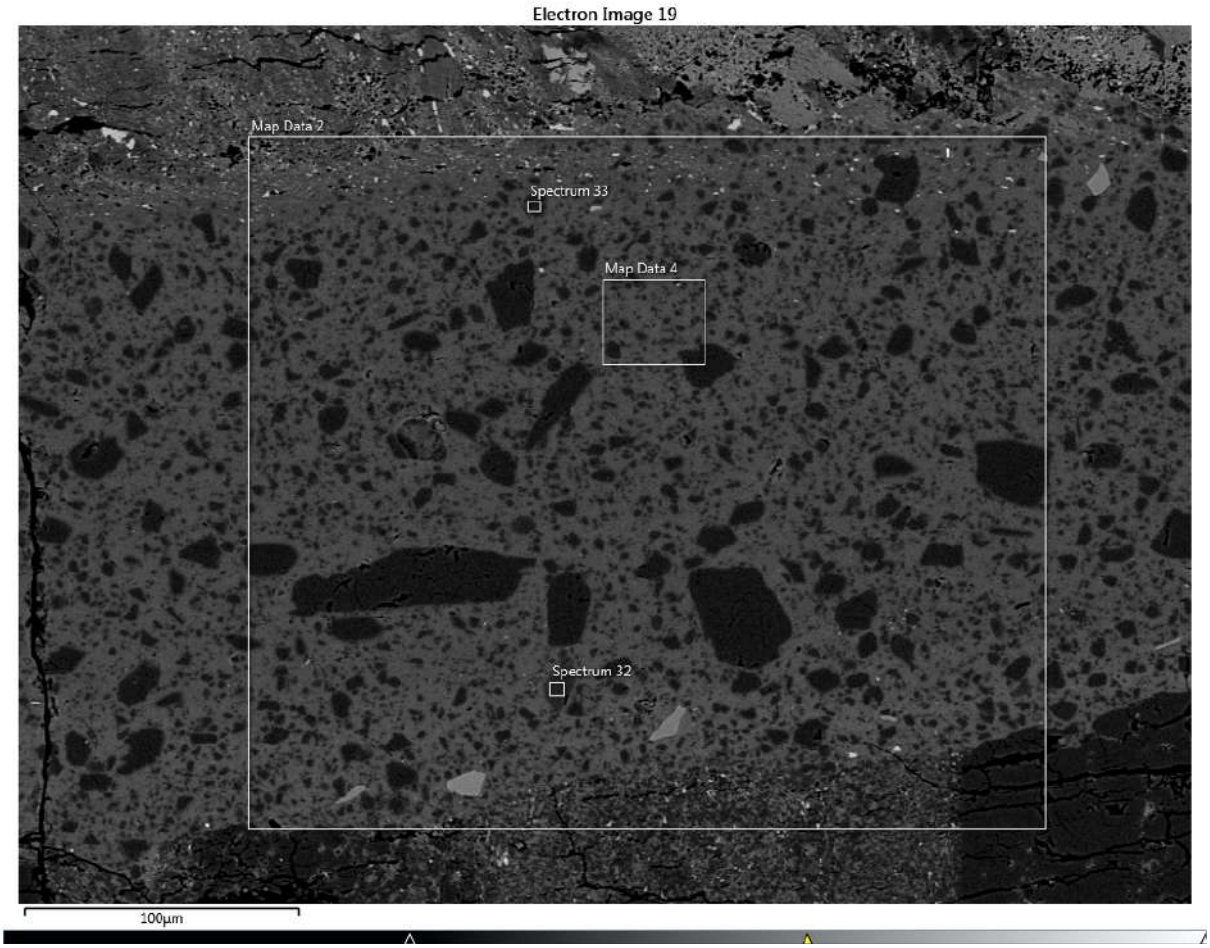

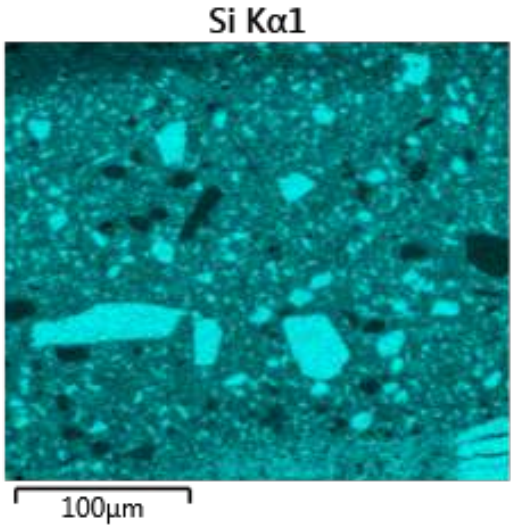

Quartz clasts

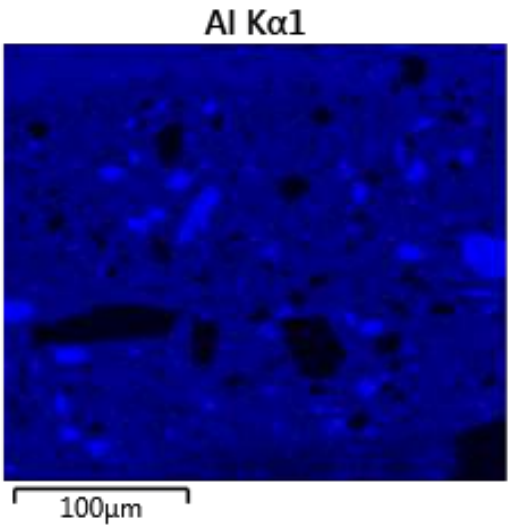

Sillimanite clasts

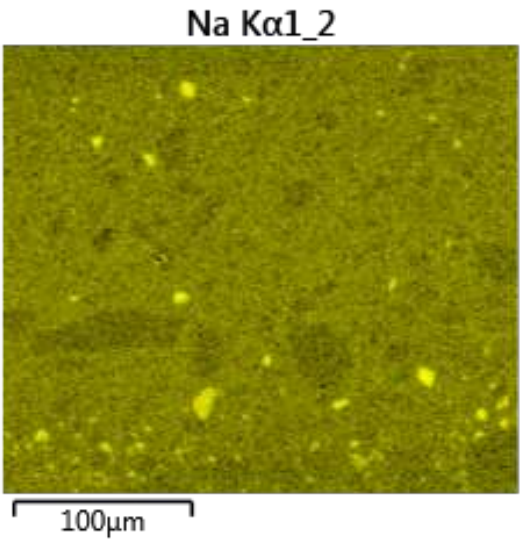

Plagioclase clasts

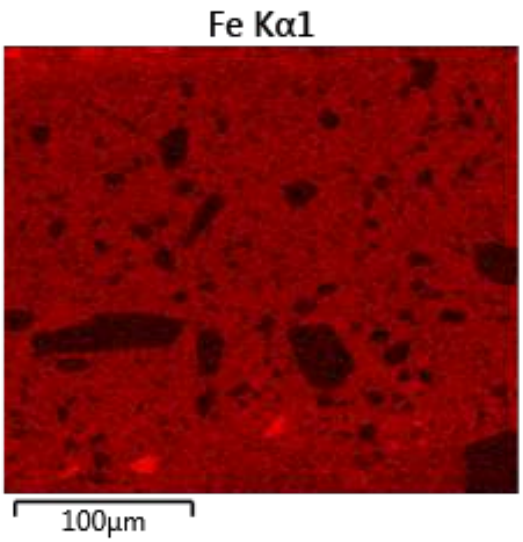

Garnet clasts

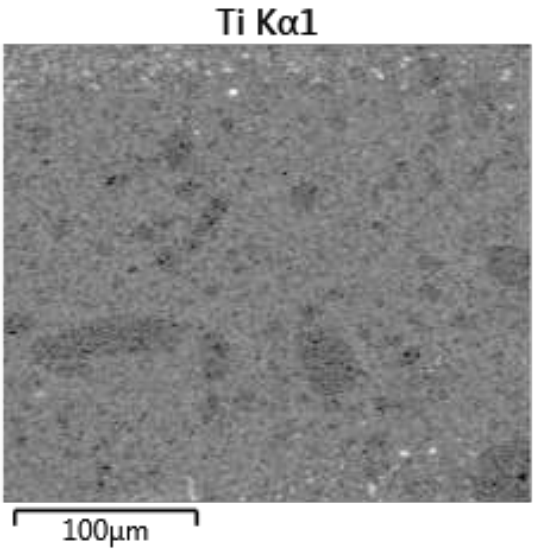

Ilmenite clasts

ITEM S3 – EDS semi-quantitative point analyses in the area of fig. 4.4D – sample S1771

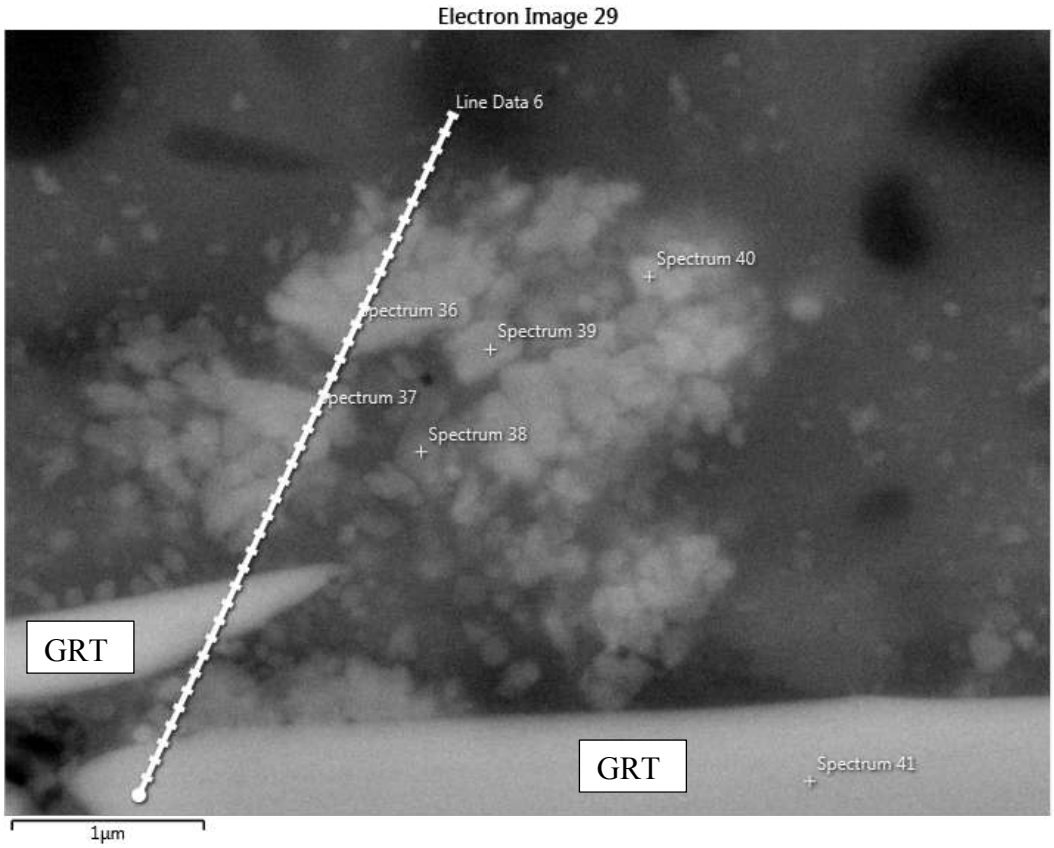

% ox	36-grt?	37-grt?	38-grt?	39-grt?	40-grt?	41-hr-grt
SiO2	48.8	48.4	35.5	33.2	36.5	36.3
FeO	20.0	19.1	23.4	25.7	23.8	33.7
Al2O3	15.5	16.8	24.2	20.4	21.5	22.6
K2O	1.9	2.2	2.3	1.4	1.7	0.7
MgO	13.1	12.6	13.8	18.9	15.6	4.6
TiO2	0.3	0.5	0.5	0.0	0.5	0.0
CaO	0.3	0.4	0.4	0.3	0.4	1.3
MnO	0.0	0.0	0.0	0.0	0.0	0.8

Line Data 6

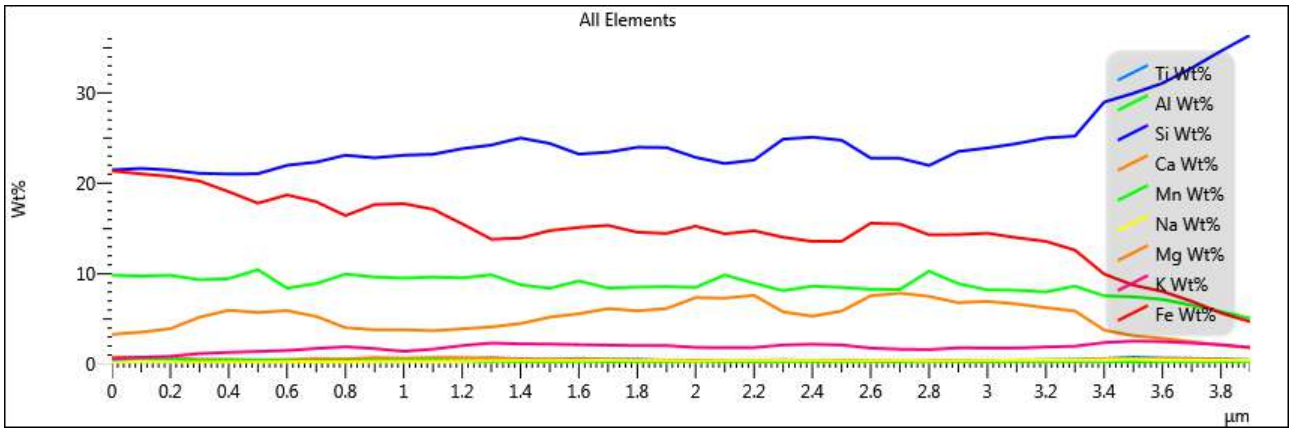

ITEM S4

EDS semi-quantitative point analyses in the area of fig. 4.4E – sample S1769

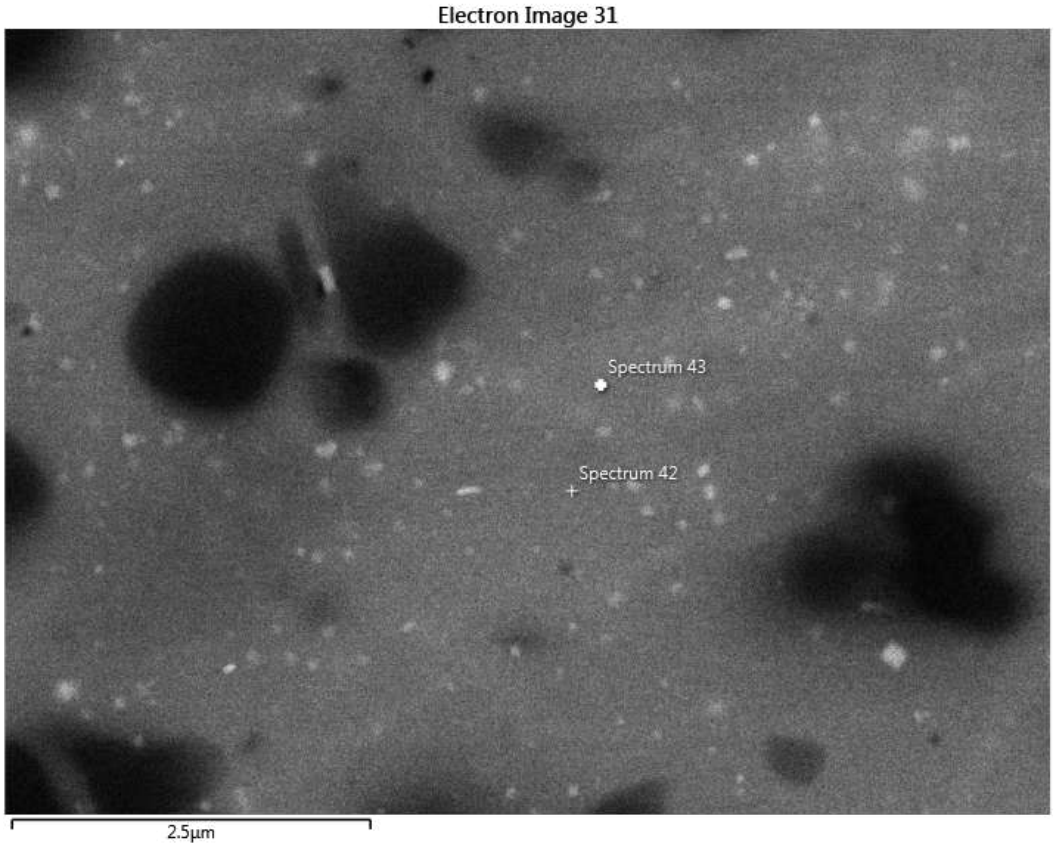

% ox	42-Glass	43-Glass
SiO2	56.0	58.1
FeO	12.1	12.0
Al2O3	20.0	18.8
K2O	3.7	3.5
MgO	3.8	3.7
TiO2	1.5	1.3
CaO	1.7	1.5
Na2O	1.2	1.1

5 Pseudotachylytes and pseudotachylyte/mylonite associations in the Calabrian lower crust

Simone Papa[1], Giorgio Pennacchioni[1], Alberto Ceccato[2], Andrea Cavallo[3]

Abstract

The Calabrian Serre Massif in Southern Italy was subjected to granulitic metamorphism during the late Hercynian Orogeny and contains huge volumes of pseudotachylyte. These pseudotachylytes generally crosscut low-strain felsic and mafic granulite-facies rocks and are either pristine with microlitic texture or foliated and recrystallised. A pristine pseudotachylyte within strongly-foliated lower-crustal migmatitic paragneisses has a peraluminous composition that allows very uncommon crystallisation of sillimanite microlites. This pseudotachylyte likely developed under low p-high T conditions based on the growth of cordierite, biotite, and Ca-rich plagioclase as result of devitrification. Within mafic granulites, foliated pseudotachylytes are crosscut by younger pseudotachylytes, reflecting an interplay of seismic failure and post- to inter-seismic ductile creep. Growth of new garnet in younger pseudotachylytes is interpreted as evidence that repeated transient seismic behaviour occurred under lower crustal conditions. We conclude that Calabrian pseudotachylytes formed after the Hercynian metamorphic events during exhumation of the lower crust and locally were overprinted by ductile shear under the same conditions. Owing to water-deficient conditions of the exhuming lower crust, pseudotachylytes were not affected by Alpine and Apenninic deformation and preserved their original textures.

5.1 Introduction

[1] Department of Geosciences, University of Padova, Italy
[2] Department of Biological, Geological and Environmental Sciences, University of Bologna, Italy
[3] CERTEMA, Cinigiano (Gr), Italy

There is increasing evidence that ductile deformation and metamorphic re-equilibration of lower crustal dry rocks are associated with precursory seismic failure (Jamtveit et al., 2018; Menegon et al., 2017; Hawemann et al., 2019), that produces a discrete zone of fragmented rock (Reches and Dewers, 2005; Petley-Ragan, 2019) and pseudotachylyte veins. The presence of a tabular rheological heterogeneity represents a viscosity perturbation that allows ductile shear zones to localise in the weak layer, or alternatively at the boundary of a strong layer (Pennacchioni and Mancktelow, 2018 and references therein). Wall rock fragmentation promotes fluid influx and fluid-driven metamorphism that represents an additional weakening process causing strain localisation in a larger volume than just the pseudotachylyte vein itself (Jamtveit et al., 2019 and references therein). It is now widely accepted that large portions of the continental lower crust are effectively dry (Yardley and Valley, 1994; Jamtveit et al., 2016), and consequently high-strength and seismicity in the lower crust should be the rule rather than the exception. However, the preservation of deep crustal pseudotachylytes through the entire exhumation process is critical (Kirkpatrick and Rowe, 2013; Price et al., 2012; Phillips et al., 2019), and only few localities worldwide are known where lower crustal pseudotachylytes and associated mylonites are preserved (e.g. Woodroffe Thrust, Central Australia; Bergen Arcs, Western Norway; Lofoten, Northern Norway; Ivrea Zone, Western Alps).

One of these fortunate localities is the Calabrian Arc in Southern Italy, where the occurrence of extremely well-preserved lower crustal pseudotachylytes has been documented by Altenberger et al. (2011; 2013). In this chapter we report field, microstructural, and petrological observations for pseudotachylytes collected from a locality described by Altenberger et al. (2013), and from a new one. We show how huge volumes of pseudotachylytes in the Hercynian lower crust exposed in Calabria testify very intense seismic activity in granulite-facies rocks. Pseudotachylytes are hosted in undeformed lower crustal rocks and provide the necessary weak planar precursors for ductile strain localisation. We present microstructural evidence for cyclic pseudotachylyte development interposed by localised ductile deformation and document the first finding of cordierite-bearing, peraluminous pseudotachylytes featuring sillimanite microlites crystallised directly from the melt. This is a preliminary study that aims at paving the way to a further in-depth analysis of Calabrian pseudotachylytes that represent a unique information source about the rheology of the granulitic continental lower crust.

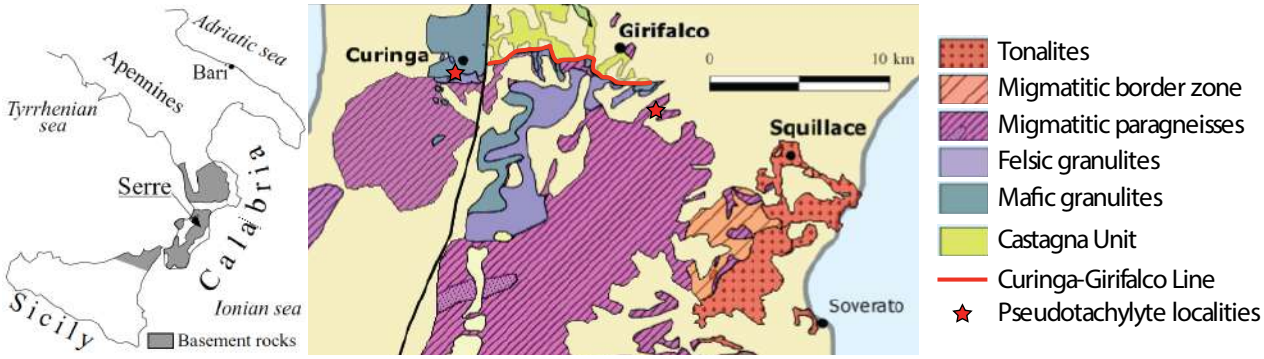

Figure 5.1 Location of the Serre Massif in Calabria and geological sketch map of the northern Serre Massif (modified from Borsi et al., 1976; Fornelli et al., 1994; Grässner and Schenk, 1999; Rottura et al., 1991; Caggianelli et al., 2013; Acquafredda et al., 2006).

5.2 Geological setting

In the Serre Massif of Calabria a circa 23-km-thick, almost complete, cross-section of the Hercynian continental crust is exposed from the upper to the lower levels (Schenk, 1980). This crustal section, based on the lithological sequence and radiometric dates, has been correlated to the Ivrea Zone of the Western Alps, with wich it shares large similarities (Moresi et al., 1978; Schenk, 1981). The granulitic lower portion of the crust (circa 7 km thick) was subdivided by Schenk (1984) in a *granulite-piryclasite unit* at the bottom in the NW, and a *metapelite unit* at the top in the SE (Fig. 5.1). The *granulite-piryclasite unit* consists of mafic granulites (mostly two-pyroxene metagabbroes ± garnet ± amphibole) and felsic granulites together with minor bodies of metapelite and spinel peridotite. They are overlaid by the *metapelite unit* that is maily constituted by migmatitic aluminous paragneisses. The migmatitic metapelites show a mineral assemblage defined by variable amounts of biotite, sillimanite, plagioclase, quartz, garnet, cordierite, K-feldspar and ilmenite/rutile (Festa et al., 2012). At peak conditions the metapelites underwent widespread partial melting with a maximum

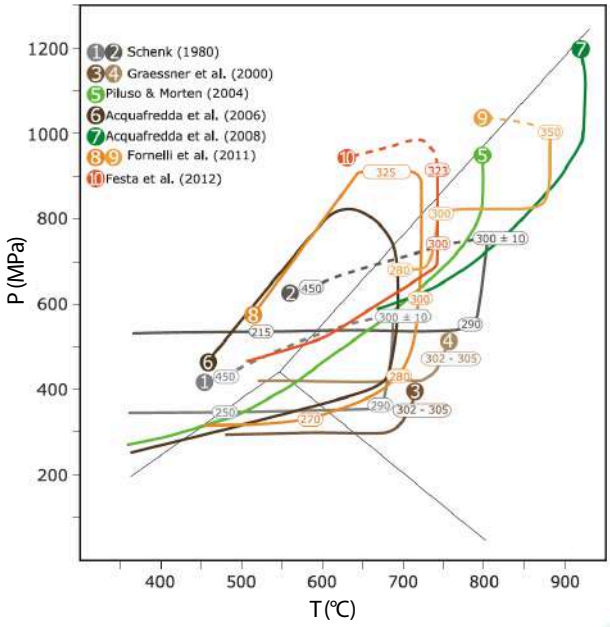

Figure 5.2 Compilation of available p-T-t paths for the Serre and Sila lower crust (from Caggianelli et al., 2013)

degree of melting of 50-60% (Caggianelli et al., 1991). Restites are massive rocks with high content of garnet and sillimanite or garnet and cordierite. Toward SE, the *metapelite unit* overlays the granitoids of the Serre Batholith emplaced in the middle crust. The contact is transitional and characterised by the so called *migmatitic border zone* (Clarke and Rottura, 1994). Toward N, the *granulite-piryclasite unit* is thrusted over the Hercynian amphibolite-facies granitoid orthogneisses of the Castagna Unit, that experienced a greenschist facies overprint of Alpine age (Schenk, 1980). This contact, that mainly consists of mylonites of Alpine age (Langone et al., 2006), is called *Curinga-Girifalco Line* and was compared by Schenk (1981) to a segment of the Insubric Line that in the western Alps separates the Ivrea zone, unaffected by the Alpine event, from the Sesia-Lanzo zone, overprinted by intense Alpine metamorphism.

The main metamorphism in the Calabrian basement occurred at 299–304 Ma, during the late stages of the Hercynian orogeny (Grässner et al., 2000; Langone et al., 2010), roughly synchronous with the emplacement of granitoids in the middle crust. Peak metamorphism during the Late Hercynian phase reached a T of 790 °C and a P of 750 MPa, according to Schenk (1989). More recently, several authors have estimated for the lower crust peak temperatures between 700-900°C and pressures above 600 MPa (Fig. 5.2; Grässner et al., 2000; Piluso and Morten, 2004; Acquafredda et al., 2006; Acquafredda et al., 2008; Fornelli et al., 2011; Festa et al., 2012). Most of the published P-T-t paths show that after peak metamorphism the lower crust underwent a fast, nearly isothermal decompression followed by a slow isobaric cooling (Fig. 5.2).

The whole lower crust, together with the deepest late-Hercynian granitoids that overlays it, shows a metamorphic foliation that dips constantly toward SE, with an average dip of about 40° (Kruhl and Huntemann, 1991). This is related to the crustal-scale tilting during Oligocene-Miocene (about 35 to 15 Ma) exhumation connected with extension and erosion (Thomson, 1994).

5.3 Turrina quarry pseudotachylytes

The Turrina quarry, SW of Curinga (Fig. 5.1), reveals the best exposition of the lowermost crustal levels in the Serre Massif (Caggianelli et al., 2013). The quarry is located within the *granulite-pyriclasite unit* (sensu Schenk, 1984), and shows an alternation of felsic granulites and mafic granulites with minor spinel-peridotite bodies. Acquafredda et al. (2008) estimated peak metamorphic conditions of 900°C and 1.1 GPa for the mafic granulites. All rocks show an evident

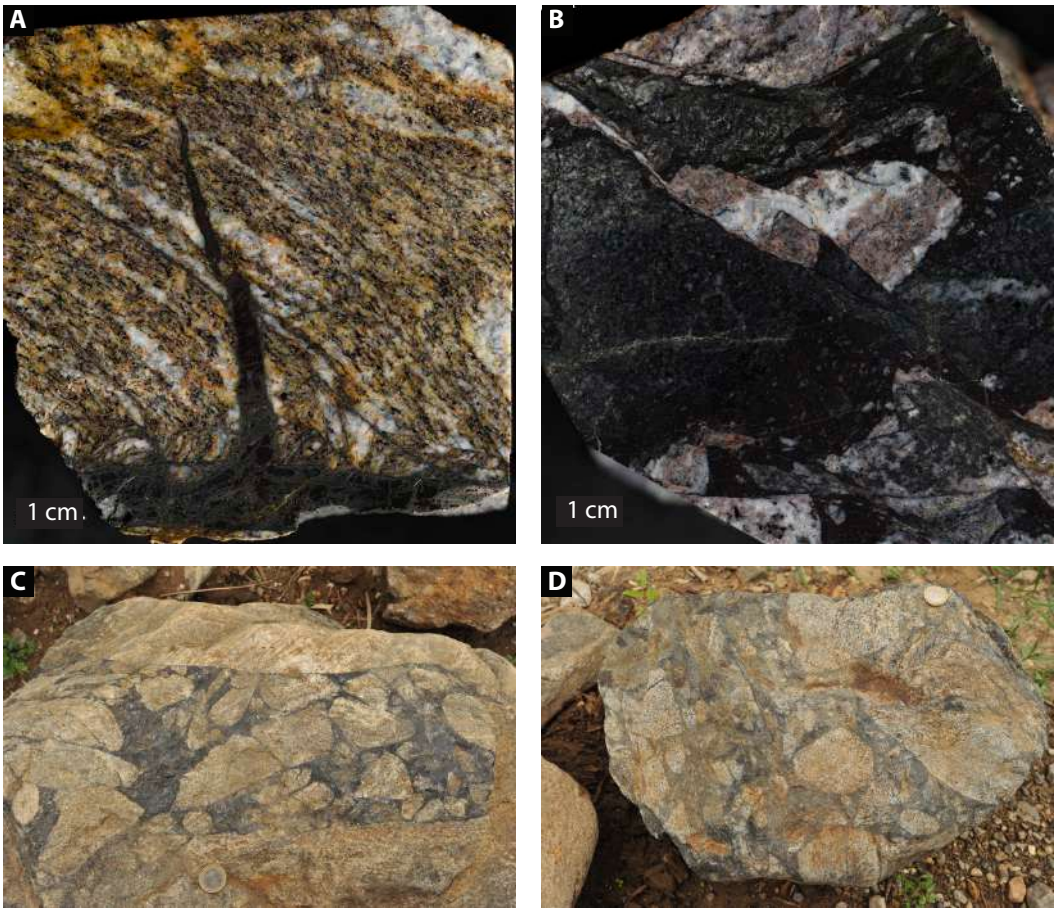

Figure 5.3 Hand samples of pseudotachylytes in felsic granulites at Turrina quarry. A) A biotite-garnet-sillimanite felsic granulite showing a thin foliation parallel pseudotachylyte vein crosscut by thick pseudotachylyte vein with an orthogonal injection vein. B) Garnet-rich felsic granulite showing several superimposed generations of pseudotachylytes veins. C-D) Loose blocks showing massive pseudotachylyte breccias within felsic granulites. 1 € coin for scale.

foliation, which is parallel to the boundary between mafic and felsic granulites, and to the general foliation of the Serre Massif (~ 40° toward SE). Pseudotachylytes in the Turrina quarry have been first reported by Altenberger et al. (2011; 2013). Altenberger et al. (2013) estimated that pseudotachylytes originated at deep crustal conditions (> 0.85 GPa) based on the simultaneous growth of orthopyroxene and plagioclase as well as almandine. Here we report microstructures and mineral assemblages for pseudotachylytes from felsic and mafic granulites.

5.3.1 Felsic granulites

Felsic granulites are made up of quartz, feldspars, garnet, and biotite, they show a clear foliation outlined by compositional variation and preferred orientation of biotite, that is sharply crosscut by thick (up to several cm) pseudotachylyte veins (Fig. 5.3). Only locally, very thin pseudotachylyte veins parallel to the granulite foliation are crosscut by thicker veins that developed oblique to the

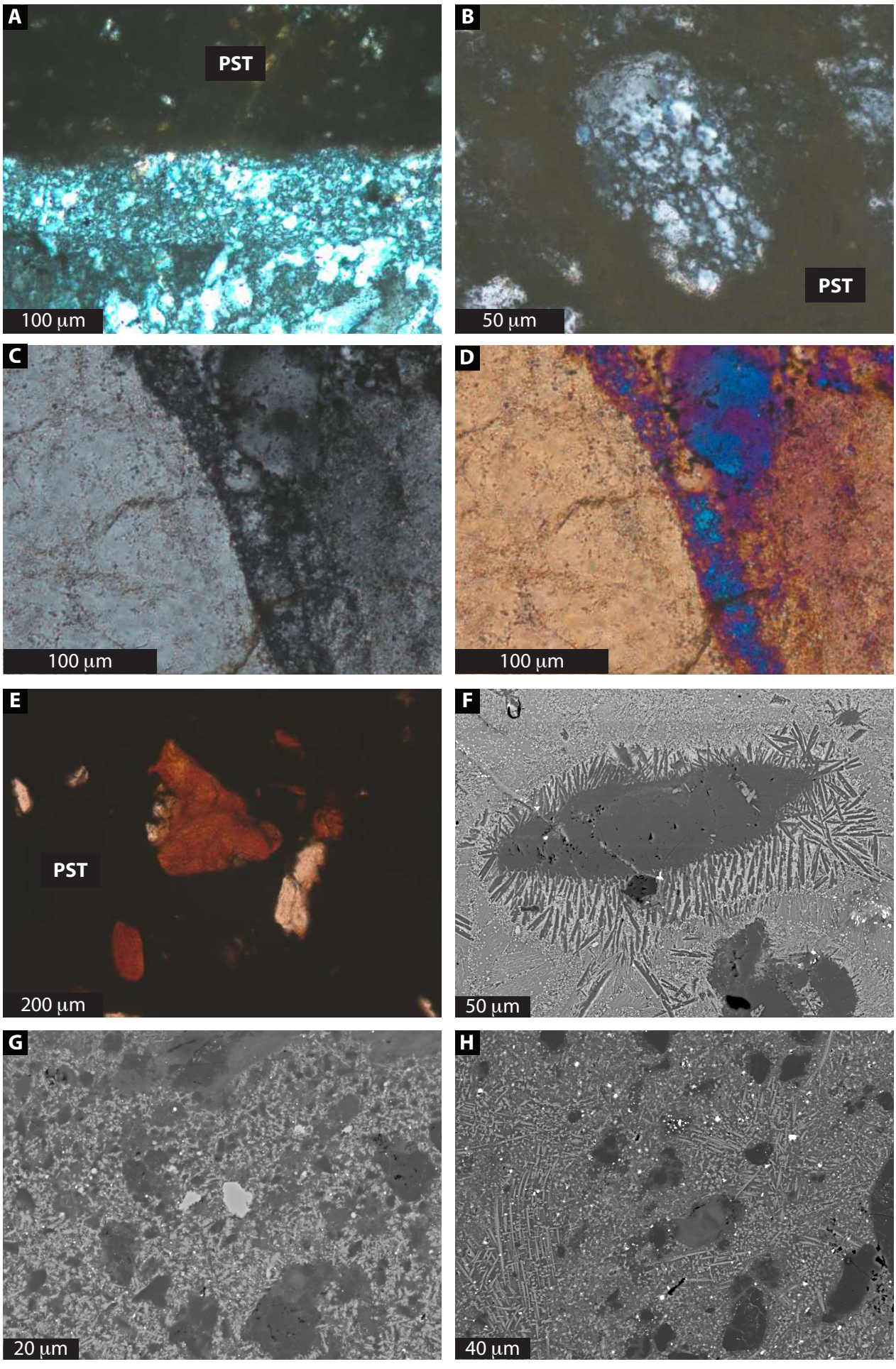
A
PST
100 μm
B
PST
50 μm
C
100 μm
D
100 μm
E
PST
200 μm
F
50 μm
G
20 μm
H
40 μm

Figure 5.4 Microstructures of pseudotachylytes within felsic granulites at Turrina quarry. A) Band of finely recrystallised plagioclase in the host rock at the boundary with pseudotachylyte. B) Recrystallised quartz clast in undeformed pseudotachylyte. C) Band of recrystallised grains in host-rock feldspar, close to pseudotachylyte. D) Same area as in (C) with gypsum plate inserted to highlight the recrystallised band. E) Biotite clasts within black isotropic matrix of pseudotachylyte breccia. F) Skeletal and lath-like plagioclase microlites crystallised orthogonal to a plagioclase clast. G) Garnet clasts showing an incipient development of crystal facets. The matrix is made up of a fine intergrowth of biotite and plagioclase. H) Pseudotachylyte matrix dominated by skeletal and lath-like biotite microlites. Photomicrograph with crossed nicols: A-D; Photomicrograph with parallel nicols: E; SEM-BSE images: F-H

foliation (Fig. 5.3A). A significant dragging of the foliation is observed at the border of large veins (Fig. 5.3A). In some cases several generations of pseudotachylytes crosscut each other forming complex patterns (Fig. 5.3B). In felsic granulites, the frequency of pseudotachylyte veins is remarkable and huge amount of melt is hosted in outstanding pseudotachylyte breccias up to tens of centimeters thick that are relatively common in the felsic granulites in the Turrina quarry area (Fig. 5.3C-D). No macroscopically detectable development of ductile shear zones is observed associated to pseudotachylyte veins or in their host rock. Under the microscope, quartz and feldspars in the host rock at the boundary of the pseudotachylytes commonly show bands of very small recrystallised grains (Fig. 5.4A-D). These bands of recrystallised grains, from few tens to hundreds of micron thick, are observed both along fault veins and injection veins and can be either parallel to the vein boundary (Fig. 5.4A) or along discrete fractures at high angle to the vein boundary (Fig. 5.4C). Very fine recrystallisation is generally present in quartz and feldspar clasts within pseudotachylytes (Fig. 5.4B). These features are not observed in the host rock minerals at a distance of few mm from the veins.

Pseudotachylytes commonly preserve a pristine microlitic texture, clearly indicating that they were not overprinted by post-seismic deformation. Skeletal plagioclase and biotite microlites are widespread and can reach hundreds of microns in length (Fig. 5.4F,H). Smaller hercynite euhedral microlites are locally present. Unmelted host rock clasts within the veins are mostly feldspars and quartz, although locally garnet clasts can occur. When preserved, garnet clasts show the development of crystal facets and a chemical composition slightly different than the host-rock garnet (lower in Mg, higher in Fe and Mn; Fig. 5.4G). Pseudotachylyte breccias are characterised by the unusual preservation of biotite and garnet clasts (5.4E). The fine-grained matrix in pseudotachylytes hosted in felsic granulites is formed by an intimate intergrowth of feldspars, quartz, biotite, and oxides. No development of secondary, low-T minerals has been observed.

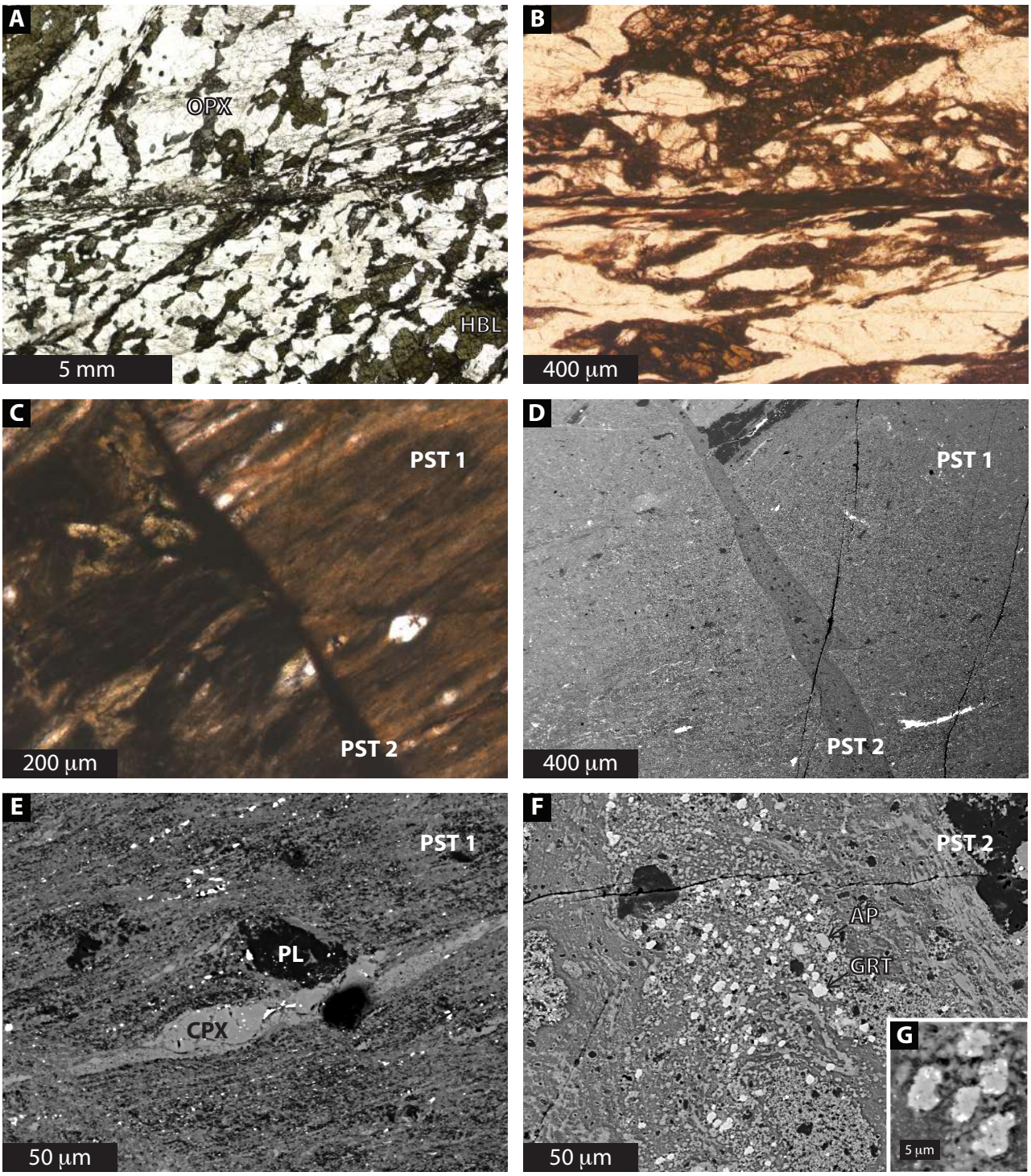

Figure 5.5 Microstructures of pseudotachylytes within mafic granulites at Turrina quarry. A) A thin pseudotachylyte vein with associated damage zone crosscut the foliation of a hornblende-rich metagabbro. B) Blow-up of A showing dextral mylonitic reactivation of pseudotachylyte and associated damage zone. C) Optical microphotograph showing crosscutting relationship between a mylonitic pseudotachylyte (PST1) with dextral oblique foliation (pseudotachylyte boundary horizontal) and a black isotropic vein crosscutting it at a high angle (PST2). D)SEM-BSE image of the same area as in (C). E) Detail of the matrix of the mylonitic pseudotachylyte (PST1). Orthopyroxene clasts are stretched and elongated parallel to the foliation. F) Cluster of 'cauliflower' garnet within the pristine matrix of PST2. Note how development of new garnet grains is limited to a portion of the vein that probably has a different chemical composition with respect to the surrounding areas. G) Detail of 'cauliflower' garnet. (A-C) Optical microphotographs – parallel nicols. (D-E) SEM-BSE images.

5.3.2 Mafic granulites

Mafic granulites mostly consist of metagabbroes made up of plagioclase, orthopyroxene, clinopyroxene, and amphibole with accessory apatite and ilmenite. Pseudotachylyte veins sharply crosscut the foliation of mafic granulites and locally act as precursors for shear zone nucleation. In an amphibole-rich metagabbro a very thin pseudotachylyte vein and the associated damage zone localised shear as indicated by development of a foliation marked by rotation and elongation of minerals (Fig. 5.5A-B). No synkinematic metamorphic reaction indicated by development of new minerals or breakdown of host rock minerals can be observed in the thin mylonite.

One mafic granulite sample shows evidence of at least two distinct generations of pseudotachylyte veins crosscutting each other (Fig. 5.5C-D). A first generation of veins crosscuts the foliation of the two-pyroxene metagabbro and shows a clear oblique foliation indicated by the preferred orientation of elongated clasts (Fig. 5.5E). The matrix of sheared pseudotachylyte is made by an intergrowth of clinopyroxene and plagioclase and elongated orthopyroxene, plagioclase, and apatite clasts are common. In table S5-1 in the supplementary material, EDS semi-quantitative chemical compositions of clinopyroxene and orthopyroxene in the host rock and within the pseudotachylyte are listed. Pyroxenes in the sheared pseudotachylyte matrix are slightly enriched in Mg, but overall the granulitic assemblage of the host rock is stable during mylonitisation. The second generation is represented by fault veins localised at the boundary of the sheared pseudotachylyte with injection veins that sharply truncate the foliation of the older vein. Injection veins have a pristine texture with preservation of flow structures and no preferential orientation of clasts. Locally, clusters of new garnet grains are locally present in these second generation veins. Garnet neoblasts have a typical “cauliflower” morphology (Pittarello et al., 2012; Pittarello et al., 2015; Lund and Austrheim, 2003; Lund et al., 2004; Hawemann et al., 2018; Altenberger et al., 2013) with abundant inclusions including minerals that are very bright in BSE images (probably sulfides). “Cauliflower” garnet have an Fe-rich composition (56% Almandine – 18% Grossular – 15% Pyrope – 8% Spessartine – 3 % Andradite) and a rather constant grain size around 5 μm. Growth of new garnet was observed only locally in a few injection veins, but is absent in most of the veins belonging to the same set. This is probably due to local changes in the chemical composition of the pseudotachylyte matrix. No garnet is present in the host mafic granulite.

Figure 5.6 Outcrop view of pseudotachylytes (roughly outlined by the black line) in the migmatitic paragneisses at Amaroni. Fault veins are only discontinuously decorated by melt as most of it was injected into the host rock in large injection veins. 1 € coin for scale.

5.4 Amaroni pseudotachylytes

We collected one sample of pseudotachylyte from a new locality located near the village of Amaroni, SW of Girifalco (Fig. 5.1; N 38° 46' 43"; E 16° 25' 41"). In this area the migmatitic paragneisses of the *metapelite unit* are in contact with mafic granulites of the *granulite/piryclasite unit*. The boundary between the two unit is marked by a tectonic contact striking NE-SW steeply dipping toward the NW, discordant to the dominant granulitic foliation that in the whole calabrian lower crust dips rather costantly and shallowly toward the SE (Paglionico and Festa, ?). The tectonic overprint is strongly partitioned in the migmatitic paragneisses that lie at the footwall of the contact in an area up to 800 m thick. This overprint is mylonitic of high-grade in the area of interest and grades to mainly cataclastic moving toward the SW. The mylonitic foliation is generally concordant with the tectonic contact. CPOs of the (c) axes for quartz dinamically recrystallised in the leucosomes of migmatitic paragneisses show peripheral maxima subparallel to the lineation that have been interpreted as result of activity of the prism<c> slip system and thus as evidence of deformation at high-T (unpublished B.Sc. theses: Carluccio, 2013; Inama, 2013; Tacchetto, 2014).

Pseudotachylytes from the Amaroni outcrop are hosted in lower crustal migmatitic paragneisses made up of garnet + biotite + sillimanite + plagioclase + K-feldspar + quartz ± cordierite. Feldspars and quartz are mainly contained in the leucosomes that form anastomosing pattern around the garnet-biotite-sillimanite melanosomes (Fig. 5.6). Garnet porphyroclasts can reach remarkable dimensions of tens of cm. The mylonitic foliation is sharply crosscut by dark grey pseudotachylyte veins. Pseudotachylyte generation surfaces are discontinuosly decorated by melt, most of which is injected within the host rock. At the outcrop scale no clear evidence of ductile reactivation of pseudotachylytes could be recognised (Fig. 5.6).

The pseudotachylyte contains a rather large percentage (> 40% volume) of relict host-rock clasts (mainly of quartz and sillimanite) embedded in a matrix rich of microlites of various shapes (see Lin (2008) for a review on microlite morphologies). No garnet clasts have been observed, and no garnet has been detected by X-ray powder diffraction, although the host rock is mostly made of large garnet crystals. Host-rock garnet in contact with the pseudotachylyte vein show the intense fragmentation that is usually observed when pseudotachylyte are hosted in garnet-bearing rocks (Austrheim et al. 2017; Papa et al., 2018). Preservation of microlites and flow structures defined by

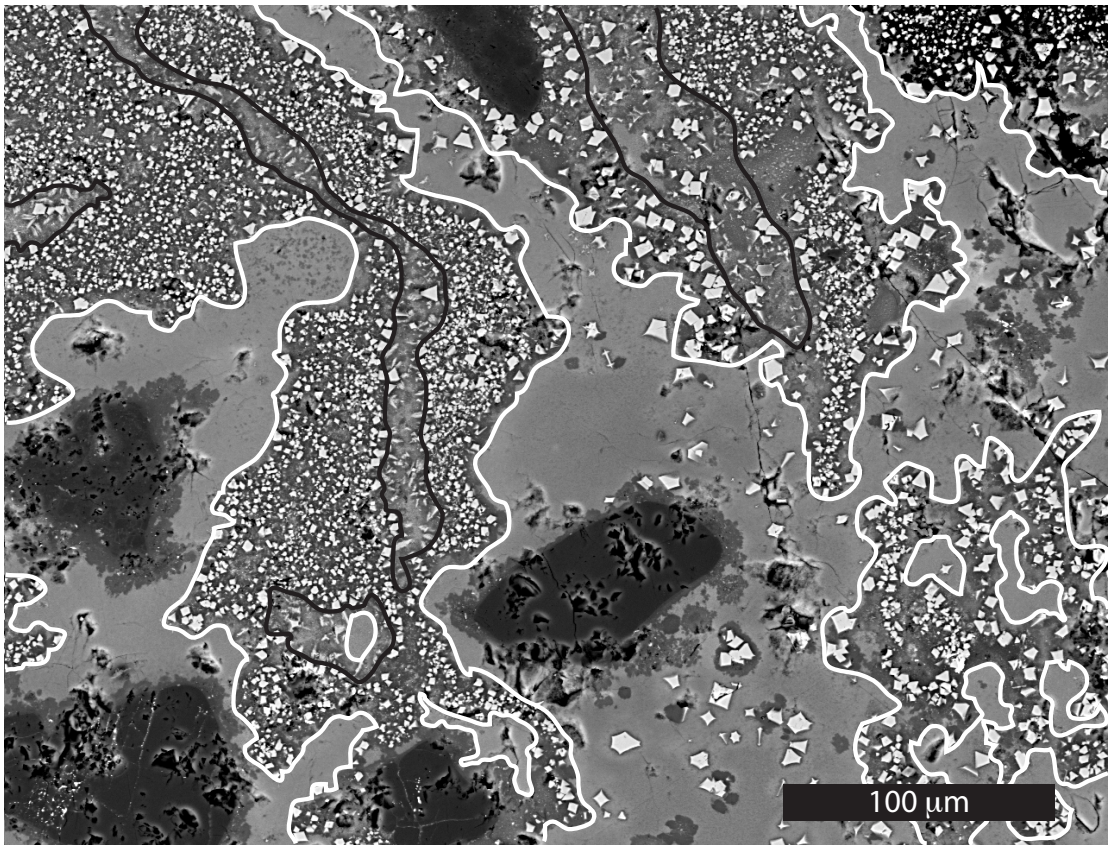

Figure 5.7 Microstructures of pseudotachylytes within migmatitic paragneisses at Amaroni. The white lines encircle areas rich of hercynite microlites, the black line areas where Fe-gedrite microlites are present. Outside the white lines, microlites are sparsely distributed and an homogeneous matrix is preserved. SEM-BSE image.

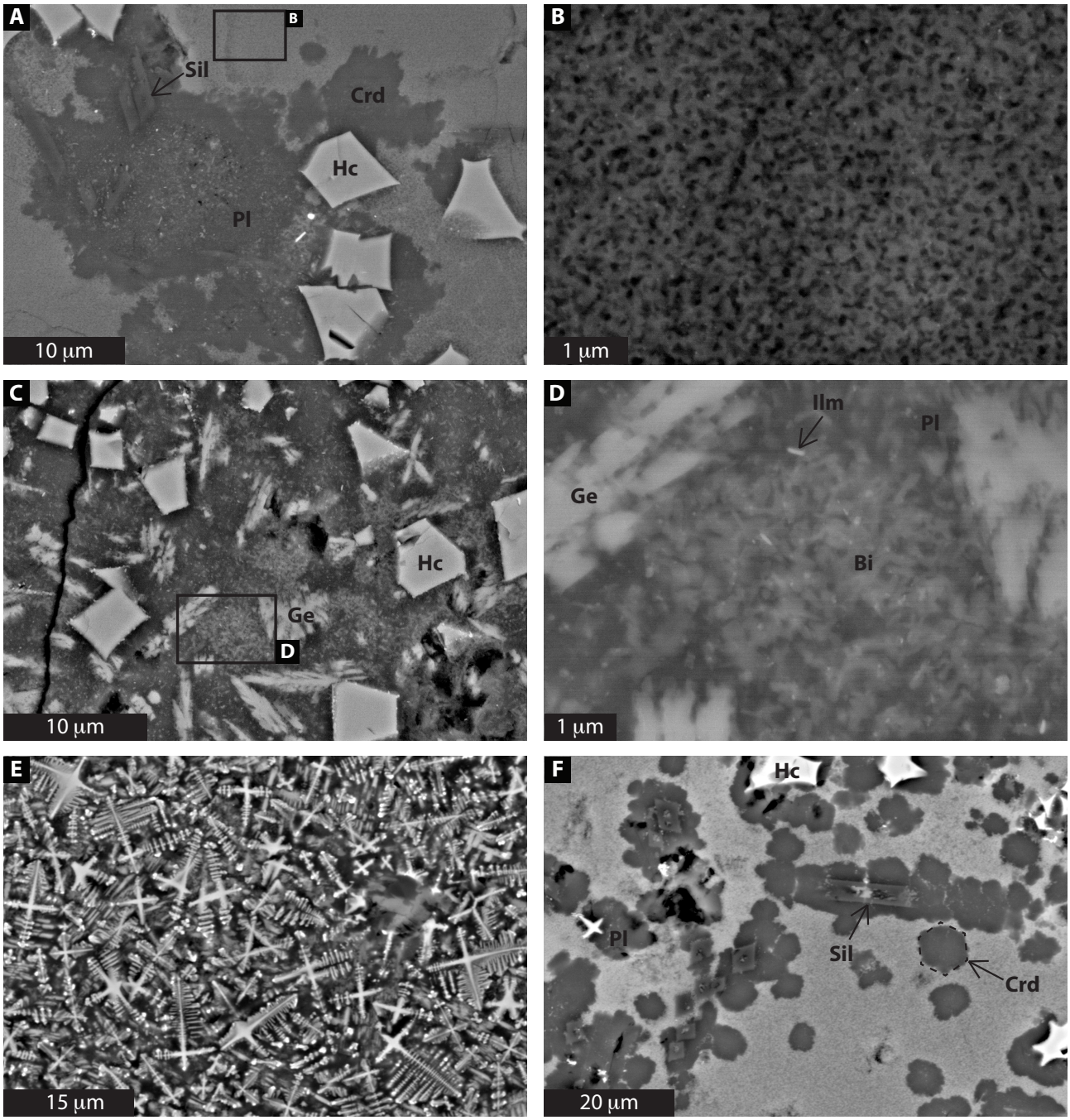

Figure 5.8 Microstructures of pseudotachylytes within migmatitic paragneisses at Amaroni. A) Cordierite and plagioclase growing on lath-like sillimanite and granular hercynite microlites, surrounded by a homogeneous matrix. Plagioclase shows plenty of inclusions of tiny biotite and ilmenite needles. B) Enlargement of the matrix in (A), made of tiny quartz crystals in a rather homogeneous groundmass. C) Granular hercynite and dendritic Fe-gedrite microlites. D) Groundmass of (C) is made up of an intimate intergrowth of plagioclase, biotite, and ilmenite. E) Dendritic and cross-shaped hercynite microlites. F) Cordierite and plagioclase growing on lath-like and box sillimanite and granular and cross-shaped hercynite microlites, surrounded by a homogeneous matrix. Note the hexagonal outline of cordierite crystals growing within the homogeneous matrix. SEM-BSE images.

layers of contrasting colour, indicate that the pseudotachylyte is pristine and was not overprinted by post-seismic deformation.

Most of the pseudotachylyte is made up of a matrix dark and isotropic in optical microscopy, characterised by tightly packed, granular to dendritic hercynite microlites (Fig. 5.7; Fig. 5.8E).

Locally, dendritic microlites of a Fe-Al-Mg silicate occur within the hercynite rich areas (Fig. 5.7; Fig. 5.8C). These microlites are very similar in shape and chemical composition to ferrogedrite (orthoamphibole) microlites reported by Ray (2004) in pseudotachylytes within biotite gneisses and sillimanite- and garnet-bearing schists. The matrix between hercynite and ferrogedrite microlites is made up of a very fine intergrowth of plagioclase, biotite, and ilmenite (Fig. 5.8D). EDS semi-quantitative analyses for these phases are reported in the supplementary material. As these minerals are tightly intergrowth at a scale which is smaller than the spot size of high-resolution EDS (300 nm), all the compositions for matrix phases show a certain degree of contamination.

In flow bands brownish in optical microscopy, hercynite microlites are more sparsely distributed (Fig. 5.7. In these areas we observed lath-like to box-shaped Al_2SiO_5 microlites (Fig. 5.8A,F; Fig. 5.9). Given that microlites crystallised directly from the melt and therefore record high-temperature conditions, we conclude that they are likely sillimanite microlites. Furthermore, X-ray powder diffraction analysis has detected no andalusite or kyanite within pseudotachylytes (supplementary). Microlites are surrounded by intergrowing plagioclase (~An 40), rich of tiny inclusions, and cordierite (Fig. 5.8A,F; Fig. 5.9). Cordierite has a roughly hexagonal outline and rather constant grain size of about 10 μm. The matrix in which microlites, and plagioclase and cordierite crystals are embedded is rather homogeneous and it is characterised by tiny nanometric quartz crystals in a homogeneous 'glassy' groundmass enriched in K, and completely devoid of Ca and Na, consumed by plagioclase crystallisation (Fig. 5.8B; chemical analysis in the supplementary material).

X-ray powder diffraction analysis of the pseudotachylyte has detected quartz (39 %), hercynite (19 %), plagioclase (19 %), cordierite (11 %), biotite (6 %), sillimanite (6 %), and ilmenite (1 %). Ferrogedrite was not measured, probably because its content is below detection limit.

5.5 Discussion and conclusions

5.3.1 P-T conditions of Amaroni pseudotachylytes

Estimating p-T conditions of formation of pseudotachylytes is very controversial given that they represent quenched melts whose mineral content was not formed at equilibrium. If

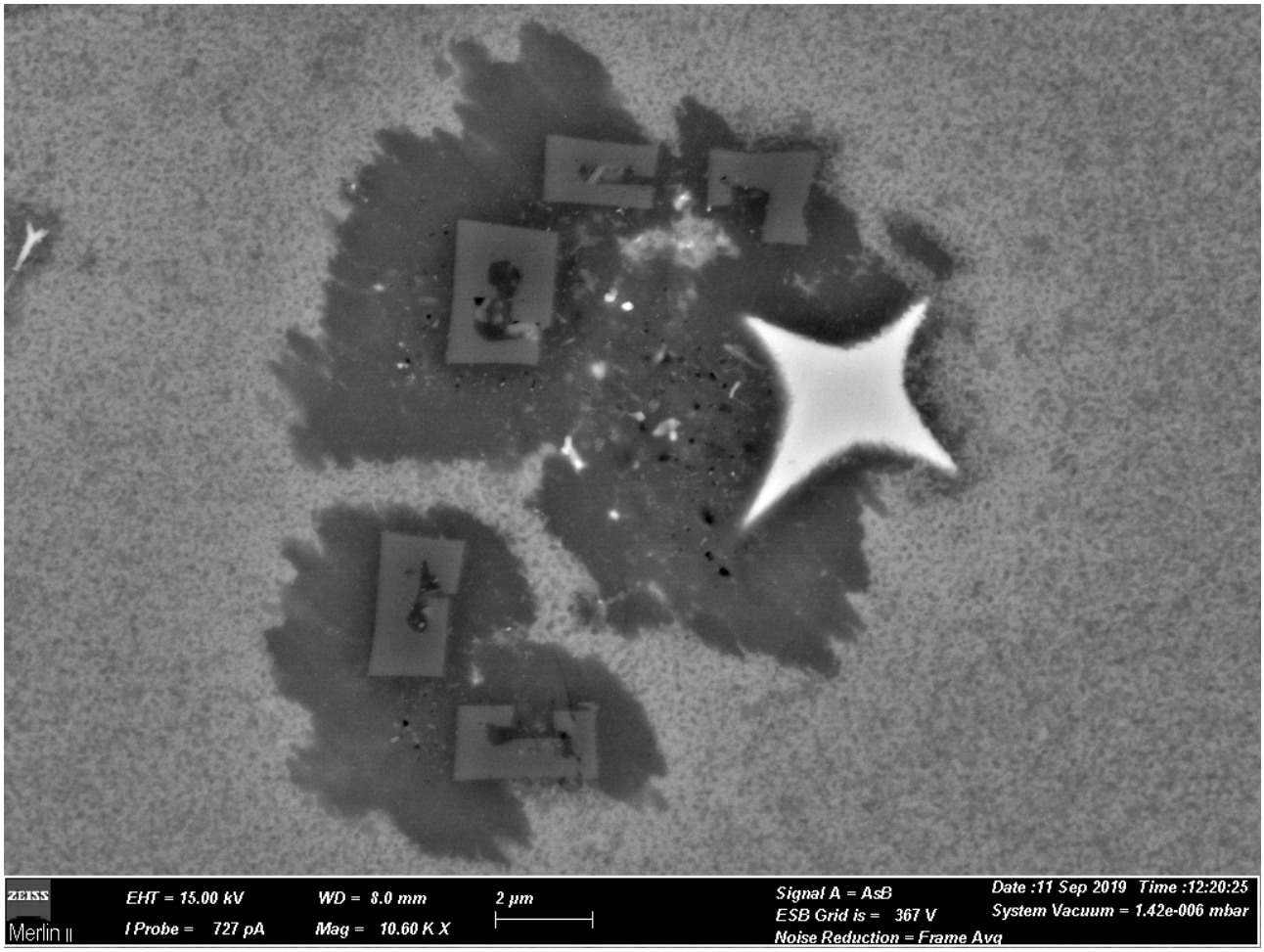

Figure 5.9 Hercynite and sillimanite microlites surrounded by plagioclase in the Amaroni pseudotachylyte.

pseudotachylytes are overprinted by ductile deformation, the equilibrium paragenesis of the mylonite can be used to estimate the p-T conditions of mylonitisation (e.g. Moecher and Steltenpohl, 2009), but these may not be representative of conditions of pseudotachylyte formation. Amaroni pseudotachylytes have very pristine microstructures with preservation of delicate microlitic textures. Therefore they were not overprinted by ductile deformation nor affected by retrograde metamorphic reactions after pseudotachylyte formation. Microlites are hercynite, sillimanite, and ferrogedrite. Microlites can be recognised by their morphology and textural relationship with the matrix (Lin, 2008); they represent primary crystals that crystallised directly from the melt during quenching (e.g., Sibson, 1975; Allen, 1979; Maddock, 1983; Spray, 1988; Toyoshima, 1990; Lin, 1994a, b; Magloughlin and Spray, 1992). Thus, microlites are high-T, 'magmatic' phases, that are not representative of the p-T conditions of the host rock at the time of pseudotachylyte formation. Crystallisation of microlites is strongly influenced by the local composition of melt as indicated by their dishomogeneous distribution within the pseudotachylyte.

Hercynite and ferrogedrite have commonly been observed as microlites in pseudotachylytes resulting from the melting of metapelites (Magloughlin, 1989; Magloughlin, 2005; Ray, 2004; Glikson and Mernaghl, 1990; Menant et al., 2018) while, to the best of our knowledge, sillimanite microlites had never been documented before.

Textural relationships indicate that plagioclase, biotite, and cordierite, that make up most of the pseudotachylyte matrix, invariably crystallised after microlite formation. If microlite are primary crystals that formed from the melt during quenching; immediately after pseudotachylyte solidification they should have been embedded in a glassy matrix. Glass is metastable and cannot be preserved in deep-seated pseudotachylytes in rocks that host even trace amounts of water (Scambelluri et al., 2017). The aggregates of plagioclase, biotite, and cordierite are thus the result of devitrification and are representative of the metamorphic conditions of the host rock at the time of pseudotachylyte formation. This suggests that post-cooling recrystallisation of the frictional melt occurred in the stability field of cordierite for metapelitic systems (low-p and temperature > 500°C; e.g. Tinkham et al., 2001). A precise thermodynamic modelling of the pseudotachylyte matrix is not possible given the extreme heterogeneity of chemical compositions, but a tentatively attempt shows that cordierite, plagioclase, biotite, quartz, and ilmenite (plus K-feldspar, not observed in our sample) can be stable in a large p-T field that goes from very low pressures up to more than 500 MPa and temperatures above 550°C (supplementary material). Considering the p-T-t paths that have been proposed for the Calabrian lower crust (Fig. 5.2), this suggests pseudotachylyte formation after the isothermal decompression phase dated at 300-280 Ma. The absence of fluid infiltration has then allowed the preservation of delicate microlite texture and metastable high temperature assemblages during the whole Alpine and Apenninic evolution.

5.5.2 Mechanism of pseudotachylyte development

Pseudotachylytes in the calabrian lower crust are hosted in foliated rocks that show no evidence of localisation of viscous flow in ductile shear zones. However, there is evidence that pseudotachylyte formation is associated with fine-grained recrystallisation of quartz and feldspars in vein-parallel bands and in microfractures close to the pseudotachylyte boundary and within survivor clasts. This may suggest the presence of a ductile precursor that could have evolved into a pseudotachylyte as result of thermal runaway ductile instability (e.g. Kelemen and Hirth, 2007). However, the observed microstructures are consistent with the model of recrystallisation within microfractures through

grain size insensitive creep within the time frame of pseudotachylyte formation put forward by Bestmann et al. (2012) for quartz and Petley-Ragan et al. (2018) for feldspars. The favoured mechanism to explain lower crustal pseudotachylytes in the calabrian lower crust is thus brittle failure. According to Altenberger et al. (2011; 2013), failure propagation may have been assisted by the presence of fluid that originated from the breakdown of hydrous minerals. However, the granulite-facies mineral assemblage is preserved within pseudotachylytes and in associated damage zones, although with subtle variation in chemical composition and no evidence of development of new hydrate minerals was observed. The absence of clear indicators of hydration associated with pseudotachylyte development suggests that brittle fracture was not triggered by fluids infiltration.

There is evidence in the mafic granulites that pseudotachylyte developed by brittle failure locally acted as precursors for localisation of subsequent ductile shearing. This is in agreement with the observations of Menegon et al. (2017) that pseudotachylytes are orders of magnitude weaker than their granulitic plagioclase-rich host rock. The observation of new garnet growing within injection veins crosscutting a sheared pseudotachylyte is an evidence of repeated cycles of seismic failure and shearing at high-T conditions.

The observed cyclicity between fracture (pseudotachylyte formation) and ductile flow (mylonitisation) in the Calabrian lower crust can either be the result of downward propagation of seismic ruptures (e.g. Moecher and Steltenpohl, 2009) or earthquakes locally triggered in the dry lower continental crust (e.g. Hawemann et al., 2018). Downward propagation of seismic ruptures is expected to cause a transient increase in stress and strain rate (Ellen and Stöckhert, 2004a) that can represent the trigger for lower crustal seismicity (e.g. Wex et al., 2019).

SUPPLEMENTARY MATERIAL FOR CHAPTER 5

CHEMISTRY PST ST-10 within mafic granulite

EDS semi-quantitative analysis (oxide wt%)

	OPX				CPX		GRT
	HOST ROCK	CLASTS (N = 3)	DAMAGE ZONE	SHEARED CLASTS (N = 2)	HOST ROCK (N = 2)	PST MATRIX	NEOBLAST (N = 2)
SiO2	46.7	49.6	45.7	47.9	49.0	50.3	35.6
FeO	40.5	35.6	35.1	36.1	15.8	12.9	29.2
MgO	12.8	14.8	13.5	14.3	8.9	10.4	3.6
Al2O3	/	/	3.2	/	2.8	2.5	21.2
CaO	/	/	1	/	23.6	23.9	7
MnO	/	/	1.6	1.7	/	/	3.4
XMg	0.42	0.49	0.47	0.48	0.56	0.65	-

XRD PST 18-06 within migmatitic paragneiss

X-Ray diffraction semi-quantitative analysis of pseudotachylyte (clasts included)

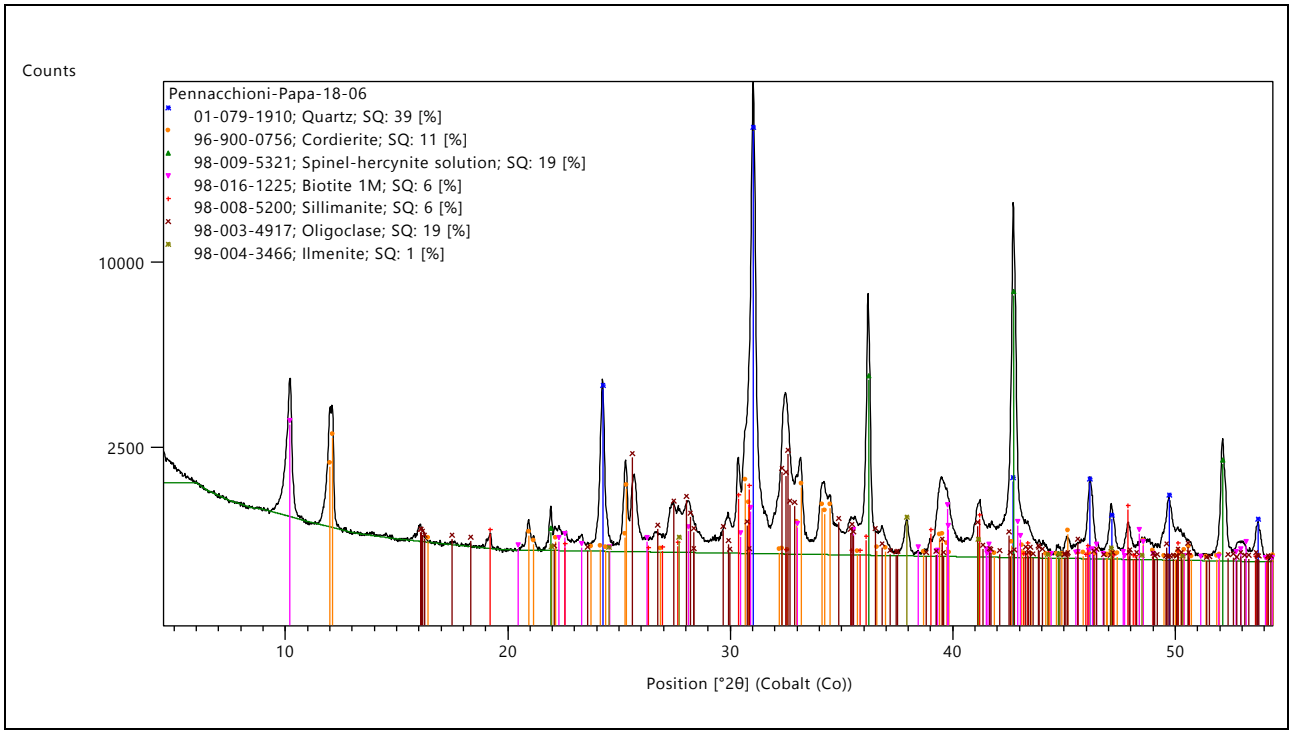

CHEMISTRY PST 18-06 within migmatitic paragneiss

EDS semi-quantitative analysis (oxide wt%)

MICROLITES:

	SILLIMANITE		HERCYNITE		FE-GEDRITE	
	(N = 5)	HR (N = 3)	(N = 7)	Literature*	(N = 13)	Literature**
SiO_2	34.1	34.6	1.2	/	45.5	45.3
FeO	1.0	0.4	34.0	38	21.9	24.4
Al_2O_3	60.9	65.0	59.8	58	16.0	15.9
K_2O	0.6	/	/	/	1.6	1.9
MgO	0.8	/	4.7	4.2	11.0	9.5
TiO_2	1.2	/	/	/	2.4	1.2
CaO	0.7	/	/	/	0.5	0.5
Na_2O	0.7	/	0.1	/	0.4	0.3
MnO	/	/	0.2	/	0.6	0.3

MATRIX

	PLAGIOCLASE	CORDIERITE	"BIOTITE"	"GLASS"
	(N = 16)	(N = 2)	(N = 6)	(N=8)
SiO_2	57.4	52.0	53.6	49.9
FeO	2.5	6.8	10.2	13.2
Al_2O_3	26.6	32.2	18.8	20.5
K_2O	1.8	0.0	5.7	6.7
MgO	1.0	8.6	4.8	7.1
TiO_2	1.5	0.0	4.2	2.7
CaO	4.9	0.3	1.4	0.0
Na_2O	4.3	0.0	1.3	0.0
MnO	/	0.0	0.0	0.0
%An	0.38	-	-	-

*Andreozzi and Lucchesi, 2002
**Ray, 2004

EDS CHEMICAL MAPS PST 18-06 within migmatitic paragneiss

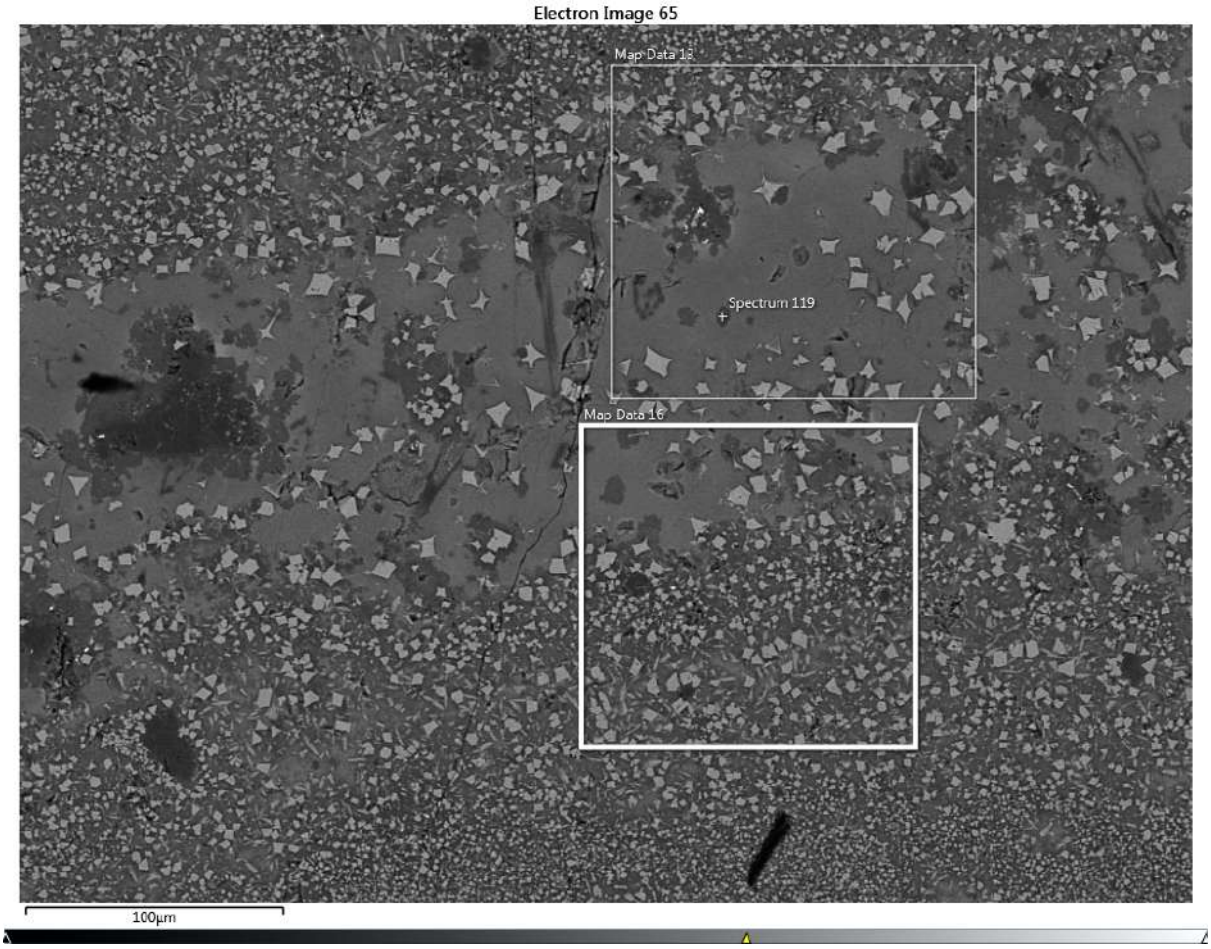

Cumulative oxide wt%

	Map 13	Map 16
SiO_2	48.4	49.3
FeO	11.6	11.9
Al_2O_3	25.9	25.1
K_2O	4.9	3.4
MgO	4.8	4.3
TiO_2	1.8	2.0
CaO	1.3	1.7
Na_2O	1.1	2.2
MnO	0.1	0.1

EDS Layered Image 16

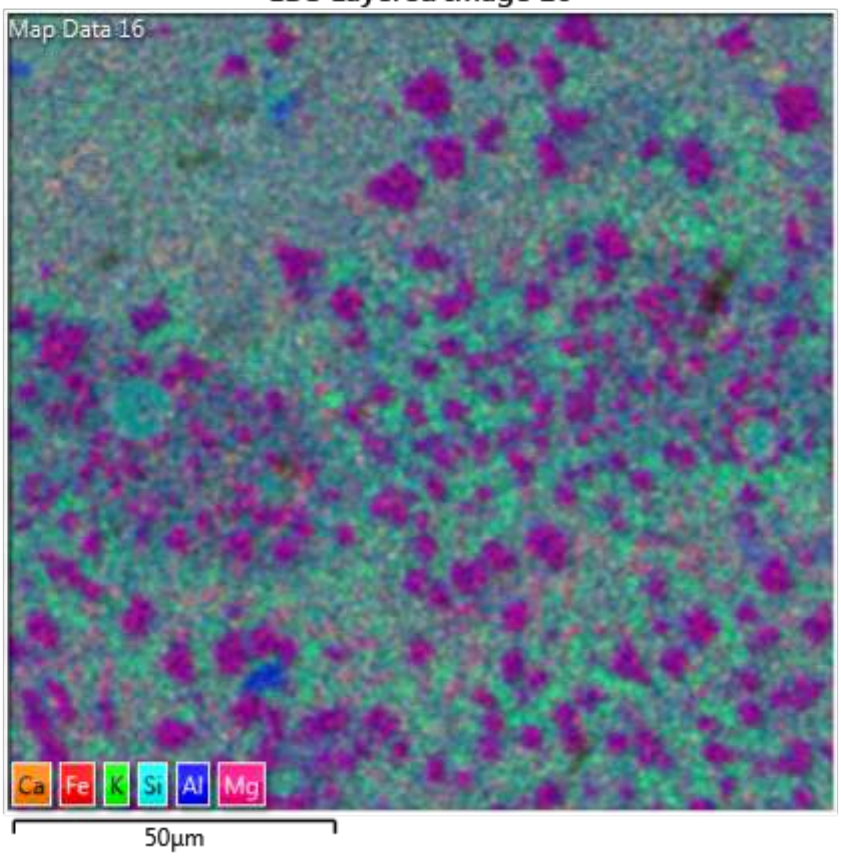

Si Kα1

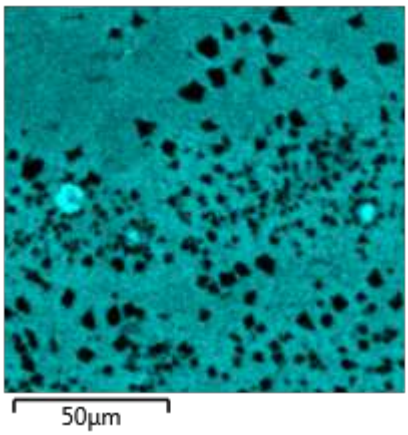

Al Kα1

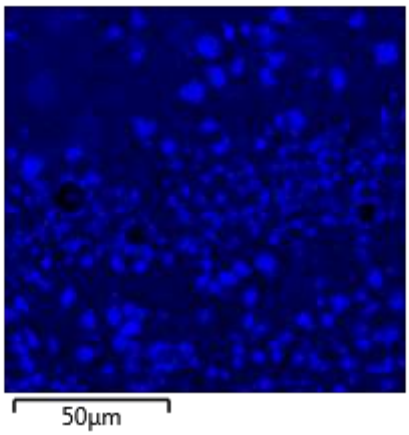

Mg Kα1_2

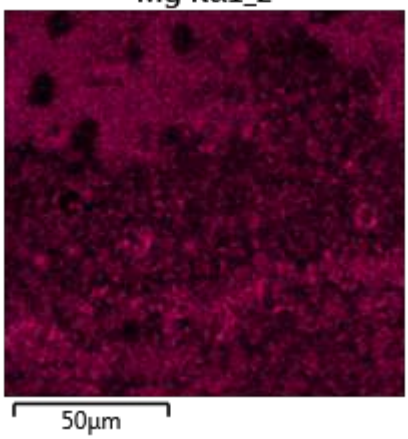

Fe Kα1

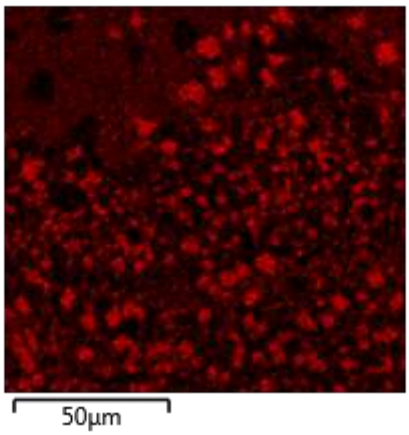

K Kα1

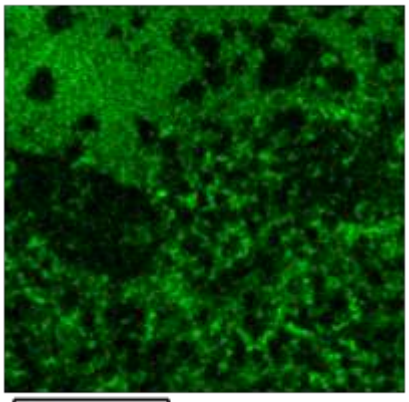

Na Kα1_2

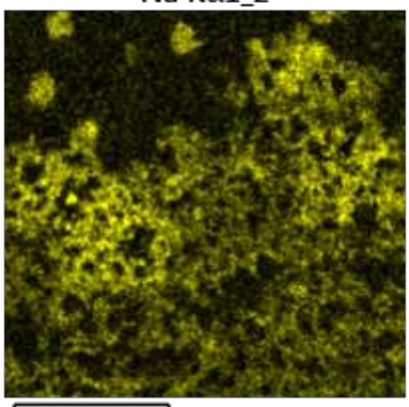

Ca Kα1

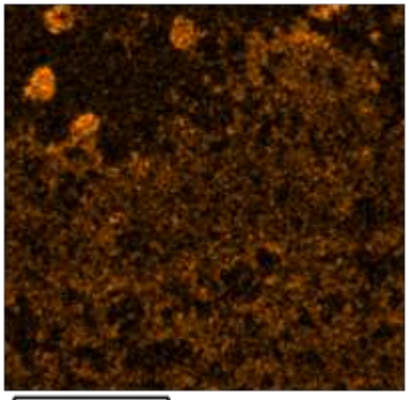

EDS Layered Image 13

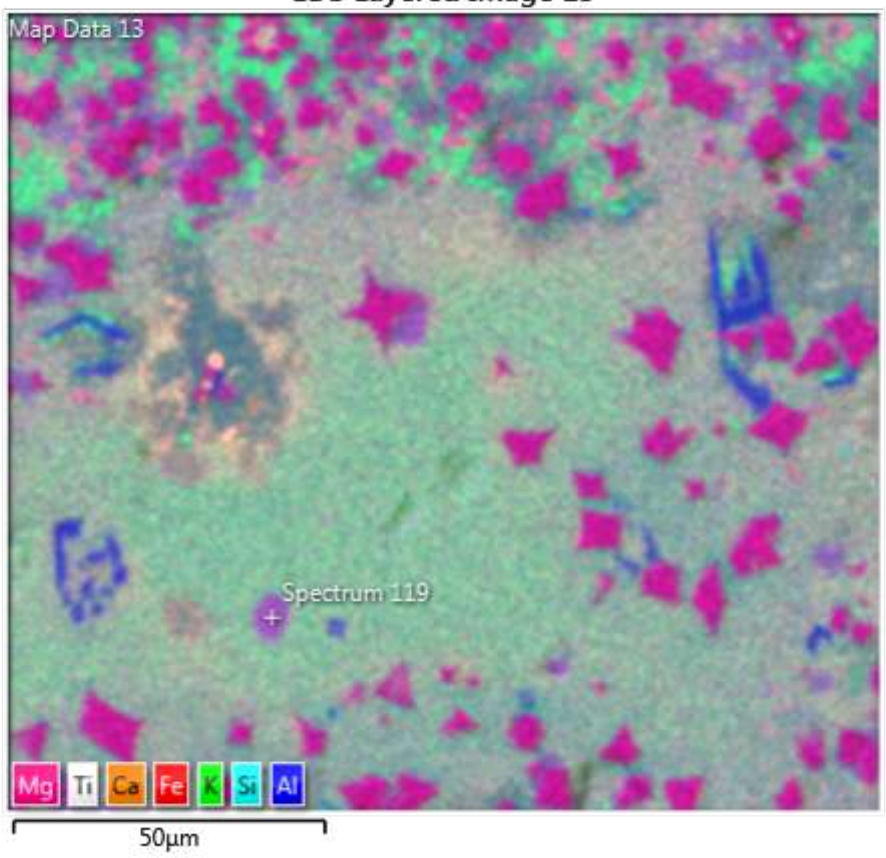

Si Kα1

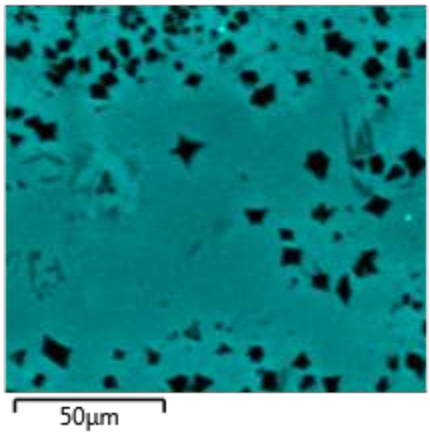

Al Kα1

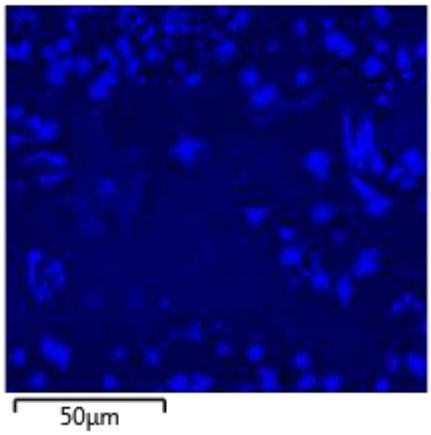

Fe Kα1

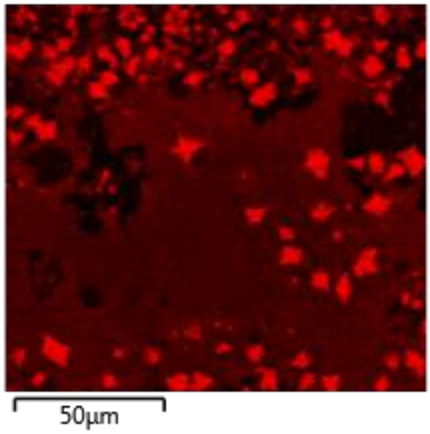

Mg Kα1_2

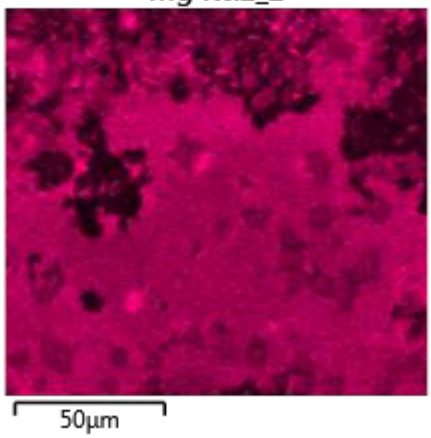

K Kα1

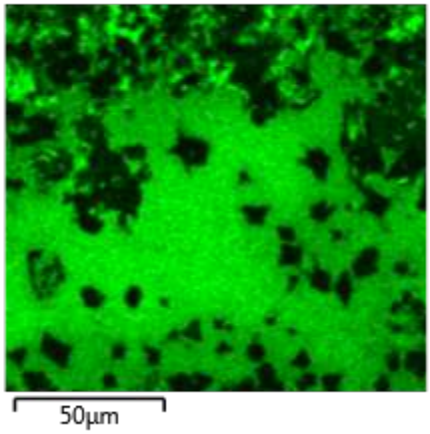

Ca Kα1

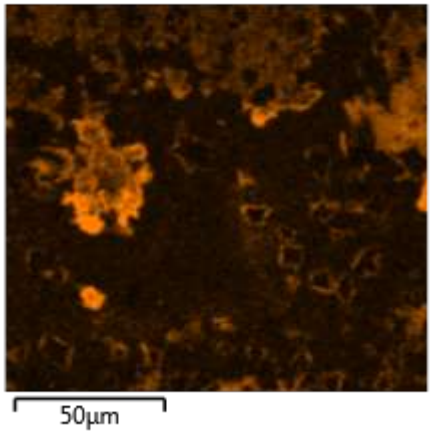

STABILITY FIELD OF CORDIERITE IN THE PSEUDOTACHYLYTE MATRIX

PST 18-06 within migmatitic paragneiss

Pseudosection calculated for the cumulative composition of map 13 after removal of 9% of hercynite, measured by image analysis. In this way, we approximate the local composition of the glass after microlite crystallisation and therefore removal from the chemical system. Calculated for conditions water saturated. Red shaded area is the field in which cordierite can be stable.

	Map 13
SiO_2	53.1
FeO	9.4
Al_2O_3	22.6
K_2O	5.4
MgO	4.8
TiO_2	2.0
CaO	1.4
Na_2O	1.2

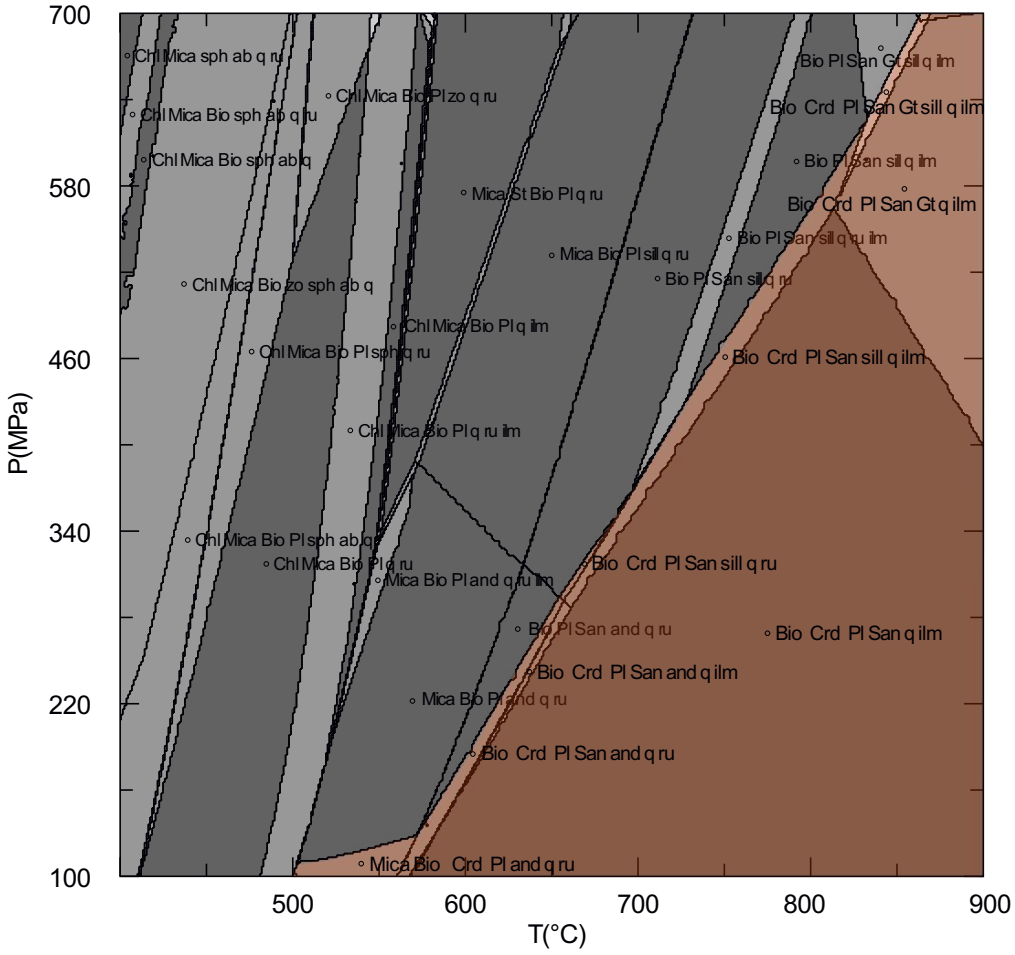

6 Conclusions and outlook

In the present thesis, the broad subject of the interplay between seismic fracture and ductile flow below the long-term brittle/ductile transition was tackled through the study of pseudotachylyte/mylonite associations in exhumed lower crustal rocks.

We have thoroughly documented the case of Mont Mary pseudotachylyte/mylonite association in which high-stress creep in the ductile crust preceded coseismic rupturing in amphibolite-facies ultramylonite. High stresses were transient and not associated to any change in temperature conditions, thus are interpreted as transients of accelerated creep induced by seismic loading of the ductile crust. Seismic ruptures could either propagate for kilometers below the brittle/ductile transition, exploiting the foliation of the mylonitic zone, or nucleate as aftershocks within the viscously flowing mylonites because of the transient downward deflection of the brittle/ductile transition caused by earthquakes in the upper crust. We showed that the latter interpretation is consistent with the observed microstructures and supported by rheological calculations. Development of Mont Mary pseudotachylytes as ductile instabilities is not supported by microstructural study, although numerical modeling shows that thermal runaway could be a viable mechanisms for earthquake nucleation in the middle to lower crust for quartz rheology at strain rates not much higher than those we estimated for the studied ultramylonites. Therefore, the question whether simultaneous development of ultramylonites and pseudotachylytes outside the classic seismogenic regime can result from ductile instabilities remains a matter of dispute. Unambiguous microstructural evidence for this process is hard to be demonstrated, since the highest-strain portions of the ultramylonite that eventually evolved into pseudotachylyte are lost during melting. Further microstructural, experimental, and modelling studies, as well as detailed field study of geometries of pseudotachylyte/mylonite associations, whose lack is a big limitation in our study, are still needed to cast more light on this phenomenon.

Whatever the mechanism of earthquake nucleation may be, propagation of seismic ruptures and frictional sliding along the slip surface cause huge modifications in the rocks crossed by, namely comminution and frictional melting. The preservation of host-rock minerals as clasts in the frictional melt is hugely influenced by their degree of comminution and their melting temperature. We showed, based on the study of natural and experimental pseudotachylytes, that thermal shock induced by frictional heating represents a major mechanism of selective comminution of rock-

forming minerals and that frictional melting preferentially affects minerals with low thermal shock resistance as garnet. We proposed an easy way to determine thermal shock resistance of minerals based on thermal pressure calculations that can easily be calculated when equation of state of minerals are known. However a huge limitation is that very little is known about other parameters, such as fracture toughness of minerals at high temperature and pression and melting point of minerals during flash melting. Moreover, to better understand the pathway that leads to frictional melting we need to characterise the comminuted material before melting. One way to do so is to study the sliding surfaces of small-displacement rotary-shear experiments.

In the present thesis we have shown how seismic ruptures can nucleate in shear zones below the long-term brittle/ductile transition along a pre-existing mylonitic foliation as a result of strain rate and stress oscillations. More enigmatic remains how seismic failure can nucleate in the lower crust within undeformed rocks. Pseudotachylytes of the Calabrian lower crust are a good example of this. In this thesis we have shown how they make no exception to the newly established paradigms of localisation of ductile shear on pre-existing pseudotachylytes and cyclicity of seismic and ductile deformation in the lower crust. A huge limiting factor for the study of Calabrian pseudotachylytes is the scarcity of good field exposures, however a thorough microstructural study of pseudotachylyte samples and particularly of their relatively unreacted wall rocks can help to shed light on the mechanisms of nucleation and propagation of seismic ruptures in the dry lower crust.

Acknowledgments

This Ph.D. was financially supported from the University of Padova:

- BIRD175145/17: “the geological record of deep earthquakes: the association pseudotachylyte mylonite” awarded to Giorgio Pennacchioni;
- Grant for long stay abroad by Foundation Ing. Aldo Gini awarded to the author;
- GRANT CPDA140255: “Tertiary pegmatites of the Central Alps: mineralogy, geochemistry, structural characters, and crystallization ages” awarded to Luciano Secco.

The staff at University of Plymouth Electron Microscopy Centre is thanked for assistance during EBSD data acquisition. Alberto Ceccato is thanked for help with rheological calculations and Channel5, and for countless discussions. Luiz Grafulha Morales and Giovanni Toffol are thanked for help with MTEX. Leonardo Tauro is thanked for thin sections preparation, Federico Zorzi for XRPD analysis, Stefano Castelli for photographs. Håkon Austrheim, Eric Ferrè, and John Spray are acknowledged for their reviews to an earlier version of chapter 3. Bernardo Cesare and Francesco Giuntoli are thanked for advice on petrology. All the coauthors (Ross J. Angel, Manuele Faccenda, Marcel Thielmann, Elena Spagnuolo, Giulio Di Toro, Andrea Cavallo, and Alberto Ceccato) are thanked for their contribution. Richard Spiess and Vincenzo Festa are thanked for introducing the author to the Amaroni outcrops in Calabria. Daniele Giuliani is thanked for good company during fieldwork in Aosta Valley.

On a personal note, I wish to thank warmly Giorgio, Luca, and Alberto for their full and wholehearted support. Thanks to my parents and girlfriend for their patience and understanding.

This dissertation is dedicated to Luca B., whose strength is an inexhaustible source of inspiration.

Bibliography

Acquafredda, P., Fornelli, A., Paglionico, A., and Piccarreta, G., 2006, Petrological evidence for crustal thickening and extension in the Serre granulite terrane (Calabria, southern Italy): Geological Magazine, v. 143(2), p. 145-163.

Acquafredda, P., Fornelli, A., Piccarreta, G., and Pascazio, A., 2008, Multi-stage dehydration–decompression in the metagabbros from the lower crustal rocks of the Serre (southern Calabria, Italy): Geological magazine, v. 145(3), p. 397-411.

Allen, A. R., 1979, Mechanism of frictional fusion in fault zones: Journal of Structural Geology, v. 1(3), p. 231-243.

Altenberger, U., Prosser, G., Ruggiero, M., and Günter, C., 2011, Microstructure and petrology of a Calabrian garnet-bearing pseudotachylyte–a link to lower-crustal seismicity: Geological Society, London, Special Publications, v. 359(1), p. 153-168.

Altenberger, U., Prosser, G., Grande, A., Günter, C., and Langone, A., 2013, A seismogenic zone in the deep crust indicated by pseudotachylytes and ultramylonites in granulite-facies rocks of Calabria (Southern Italy): Contributions to Mineralogy and Petrology, v. 166(4), p. 975-994.

Archard, J. F., 1959, The temperature of rubbing surfaces: Wear, v. 2(6), p. 438-455.

Argand, E., 1906, Sur la tectonique du Massif de la Dent Blanche: Comptes Rendus de l'Acade´mie des Sciences Paris, v. 142, p. 527–530.

Austrheim, H., 1987, Eclogitization of lower crustal granulites by fluid migration through shear zones: Earth and Planetary Science Letters, v. 81(2-3), p. 221-232.

Austrheim, H., and Boundy, T.M., 1994, Pseudotachylytes generated during seismic faulting and eclogitization of the deep crust: Science, v. 265, p. 82–83, https://doi.org/10.1126/science.265.5168.82.

Austrheim, H., Erambert, M., and Boundy, T.M., 1996, Garnets recording deep crustal earthquakes: Earth and Planetary Science Letters, v. 139, p. 223–238, https://doi.org/10.1016/0012-821X(95)00232-2.

Austrheim, H., Erambert, M., and Engvik, A. K., 1997, Processing of crust in the root of the Caledonian continental collision zone: the role of eclogitisation: Tectonophysics, v. 273(1-2), p. 129-153.

Austrheim, H., 2013, Fluid and deformation induced metamorphic processes around Moho beneath continent collision zones: Examples from the exposed root zone of the Caledonian mountain belt, W-Norway: Tectonophysics, v. 609, p. 620-635.

Austrheim, H., Dunkel, K.G., Plümper, O., Ildefonse, B., Liu, Y., and Jamtveit, B, 2017: Fragmentation of wall rock garnets during deep crustal earthquakes. Science Advances, v. 3, e1602067, DOI: 10.1126/sciadv.1602067.

Behrmann, J. H., and Mainprice, D., 1987, Deformation mechanisms in a high-temperature quartz-feldspar mylonite: evidence for superplastic flow in the lower continental crust: Tectonophysics, v. 140(2-4), p. 297-305, https://doi.org/10.1016/0040-1951(87)90236-8.

Bestmann, M., Prior, D. J., and Grasemann, B., 2006, Characterisation of deformation and flow mechanics around porphyroclasts in a calcite marble ultramylonite by means of EBSD analysis: Tectonophysics, v. 413, p. 185-200, DOI: 10.1016/j.tecto.2005.10.044.

Bestmann, M., Pennacchioni, G., Frank, G., Göken, M., and De Wall, H., 2011, Pseudotachylyte in muscovite-bearing quartzite: Coseismic friction-induced melting and plastic deformation of quartz: Journal of Structural Geology, v. 33(2), p. 169-186, https://doi.org/10.1016/j.jsg.2010.10.009.

Bizzarri, A., 2014, The destiny of a clast within a molten pseudotachylyte vein: Bulletin of the Seismological Society of America, v. 104(5), p. 2399-2411.

Borsi S., Hieke Merlin O., Lorenzoni S., Paglionico A., Zanettin B., Lorenzoni E., 1976, Stilo unit and “dioritic-kinzigitic” unit in Le Serre (Calabria, Italy). Geological, petrological, geochronological characters: Boll. Soc. Geol. It., v. 95, p. 219-244.

Brace, W. F., and Kohlstedt, D. L., 1980, Limits on lithospheric stress imposed by laboratory experiments: Journal of Geophysical Research: Solid Earth, v. 85(B11), p. 6248-6252.

Braeck, S., and Podladchikov, Y. Y., 2007, Spontaneous thermal runaway as an ultimate failure mechanism of materials: Physical Review Letters, v. 98, p. 095504(1-4), DOI: 10.1103/PhysRevLett.98.095504.

Brown, K.M., and Fialko, Y., 2012, ‘Melt welt’ mechanism of extreme weakening of gabbro at seismic slip rates: Nature, v. 488, p. 638–641, doi:10.1038/nature11370.

Burov, E. B., and Watts, A. B., 2006, The long-term strength of continental lithosphere:" jelly sandwich" or" crème brûlée"?: GSA today, v. 16(1), p. 4.

Caggianelli, A., Del Moro, A., Paglionico, A., Piccarreta, G., Pinarelli, L., and Rottura, A., 1991, Lower crustal granite genesis connected with chemical fractionation in the continental crust of Calabria (Southern Italy): European Journal of Mineralogy, v. 3(1), p. 159-180.

Caggianelli, A., Prosser, G., Festa, V., Langone, A., and Spiess, R., 2013, From the upper to the lower continental crust exposed in Calabria: Geol. Field Trips, v. 5(1/2), p. 49.

Camacho, A., Vernon, R. H., and Fitz Gerald, J., 1995, Large volumes of anhydrous pseudotachylyte in the Woodroffe Thrust, eastern Musgrave Ranges, Australia: Journal of Structural Geology, v. 17(3), p. 371-383.

Campbell, L., and Menegon, L., 2019, Transient high strain rate during localised viscous creep in the dry lower continental crust (Lofoten, Norway): Journal of Geophysical Research (accepted).

Canepa, M., Castelletto, M., Cesare, B., Martin, S., and Zaggia, L., 1990, The Austroalpine Mont Mary Nappe (Italian Western Alps): Memorie di Scienze Geologiche, v. 42, p. 1-17.

Carluccio, R., 2013, Study of the quartz c-axis preferred orientation in a granulite facies mylonite of the Calabria basement (in italian), unpublished B.Sc. thesis, University of Padova.

Ceccato, A., Pennacchioni, G., Menegon, L., and Bestmann, M., 2017, Crystallographic control and texture inheritance during mylonitization of coarse grained quartz veins: Lithos, v. 290, p. 210-227, DOI: 10.1016/j.lithos.2017.08.005.

Chen, W. P., and Molnar, P., 1983, Focal depths of intracontinental and intraplate earthquakes and their implications for the thermal and mechanical properties of the lithosphere: Journal of Geophysical Research: Solid Earth, v. 88(B5), p. 4183-4214.

Clarke, G. L., and Norman, A. R., 1993, Generation of pseudotachylite under granulite facies conditions, and its preservation during cooling: Journal of Metamorphic Geology, v. 11(3), p. 319-335.

Clarke, D. B., and Rottura, A., 1994, Garnet-forming and garnet-eliminating reactions in a quartz diorite intrusion at Capo Vaticano, Calabria, Italy: The Canadian Mineralogist, v. 32(3), p. 623-635.

Compagnoni, R., Dal Piaz, G. V., Hunziker, J. C., Gosso, G., Lombardo, B., and Williams, P. F., 1977, The Sesia–Lanzo Zone: a slice of continental crust, with alpine HP-LT assemblages in the Western Italian Alps: Rendiconti della Società Italiana di Mineralogia e Petrologia, v. 33.

Cross, A. J., Prior, D. J., Stipp, M., and Kidder, S., 2017, The recrystallized grain size piezometer for quartz: An EBSD-based calibration. Geophysical Research Letters, v. 44(13), p. 6667-6674, doi:10.1002/2017GL073836.

Cross, A. J., Kidder, S., and Prior, D. J., 2015, Using microstructures and TitaniQ thermobarometry of quartz sheared around garnet porphyroclasts to evaluate microstructural evolution and constrain an Alpine Fault Zone geotherm: Journal of Structural Geology, v. 75, p. 17-31, http://dx.doi.org/10.1016/j.jsg.2015.02.012.

Dal Piaz, G. V., 1993, Evolution of Austro-Alpine and Upper Penninic basement in the northwestern Alps from Variscan convergence to post-Variscan extension: Pre-Mesozoic geology in the Alps (pp. 327-344). Springer, Berlin, Heidelberg.

Dal Piaz, G. V., Gianotti, F., Monopoli, B., Pennacchioni, G., Tartarotti, P., and Schiavo, A., 2010, Note illustrative della Carta Geologica d'Italia alla scala 1:50.000, Foglio 091 Chatillon. Servizio Geologico d'Italia, Foglio, 091, 5–152.

Deichmann, N., and Rybach, L., 1989, Earthquakes and temperatures in the lower crust below the northern Alpine foreland of Switzerland: Properties and processes of earth's lower crust, v. 51, p. 197-213.

Den Brok, S. W. J., 1998, Effect of microcracking on pressure-solution strain rate: The Gratz grain-boundary model: Geology, v. 26(10), p. 915-918, https://doi.org/10.1130/0091-7613(1998)026<0915:EOMOPS>2.3.CO;2.

Di Toro, G., Hirose, T., Nielsen, S., Pennacchioni, G., and Shimamoto, T., 2006, Natural and experimental evidence of melt lubrication of faults during earthquakes: Science, v. 311(5761), p. 647-649.

Di Toro, G., Niemeijer, A., Tripoli, A., Nielsen, S., Di Felice, F., Scarlato, P., and Smith, S., 2010, From field geology to earthquake simulation: a new state-of-the-art tool to investigate rock friction during the seismic cycle (SHIVA): Rendiconti Lincei, v. 21(1), p. 95-114.

Ellis, S., and Stöckhert, B., 2004a, Elevated stresses and creep rates beneath the brittle-ductile transition caused by seismic faulting in the upper crust: Journal of Geophysical Research: Solid Earth, v. 109(B5), B05407, doi:10.1029/2003JB002744.

Ellis, S., and Stöckhert, B., 2004b, Imposed strain localization in the lower crust on seismic timescales: Earth, planets and space, v. 56(12), p. 1103-1109.

Engvik, A. K., Austrheim, H., and Erambert, M., 2001, Interaction between fluid flow, fracturing and mineral growth during eclogitization, an example from the Sunnfjord area, Western Gneiss Region, Norway: Lithos, v. 57(2-3), p. 111-141.

Fagereng, Å., and Biggs, J., 2019, New perspectives on 'geological strain rates' calculated from both naturally deformed and actively deforming rocks: Journal of Structural Geology, v. 125, p. 100-110, https://doi.org/10.1016/j.jsg.2018.10.004.

Ferré, E. C., Meado, A.L., Geissman, J.W., Di Toro, G., Spagnuolo, E., Ueda, T., Ashwal, L.D., Deseta, N., Andersen, T.B., Filiberto, J., and Conder, J.A., 2017, Earthquakes in the mantle? Insights from rock magnetism of pseudotachylytes: Journal of Geophysical Research: Solid Earth, v. 122, p. 8769-8785, doi: 10.1002/2017JB014618.

Festa, V., Fornelli, A., Paglionico, A., Pascazio, A., Piccarreta, G., and Spiess, R., 2012, Asynchronous extension of the late-Hercynian crust in Calabria: Tectonophysics, v. 518, p. 29-43.

Fitz Gerald, J. D. F., Mancktelow, N. S., Pennacchioni, G., and Kunze, K., 2006, Ultrafine-grained quartz mylonites from high-grade shear zones: Evidence for strong dry middle to lower crust: Geology, v. 34(5), p. 369-372, https://doi.org/10.1130/G22099.1.

Fornelli, A., Caggianelli, A., Del Moro, A., Bargossi, G. M., Paglionico, A., Piccarreta, G., and Rottura, A., 1994, Petrology and evolution of the central Serre granitoids (Southern Calabria–Italy): Periodico di Mineralogia, v. 63, p. 53-70.

Fornelli, A., Langone, A., Micheletti, F., and Piccarreta, G., 2011, Time and duration of Variscan high-temperature metamorphic processes in the south European Variscides: constraints from U-Pb chronology and trace element chemistry of zircon: Mineralogy and Petrology, v. 103(1-4), p. 101-122.

Fredrich, J.T., and Wong, T.F., 1986, Micromechanics of thermally induced cracking in three crustal rocks: Journal of Geophysical Research. Solid Earth, v. 91, p. 12743–12764, https://doi.org/10.1029/JB091iB12p12743.

Fusseis, F., Regenauer-Lieb, K., Liu, J., Hough, R. M., and De Carlo, F., 2009, Creep cavitation can establish a dynamic granular fluid pump in ductile shear zones: Nature, v. 459(7249), p. 974. 10.1038/nature08051.

Fukuda, J. I., Holyoke III, C. W., and Kronenberg, A. K., 2018, Deformation of fine-grained quartz aggregates by mixed diffusion and dislocation creep: Journal of Geophysical Research: Solid Earth, v. 123(6), p. 4676-4696, 10.1029/2017JB015133.

Gilgannon, J., Fusseis, F., Menegon, L., Regenauer-Lieb, K., and Buckman, J., 2017, Hierarchical creep cavity formation in an ultramylonite and implications for phase mixing: Solid Earth, v. 8(6), p. 1193.

Glikson, A. Y., and Mernagh, T. P., 1990 Significance of pseudotachylite vein systems, Giles basic/ultrabasic complex, Tomkinson Ranges, western Musgrave block, central Australia: Journal of Australian Geology and Geophysics, v. 11, p. 509-519.

Goetze, C., and Evans, B., 1979, Stress and temperature in the bending lithosphere as constrained by experimental rock mechanics: Geophysical Journal International, v. 59(3), p. 463-478.

Graessner, T., and Schenk, V., 1999, Low-pressure metamorphism of Palaeozoic pelites in the Aspromonte, southern Calabria: constraints for the thermal evolution in the Calabrian crustal cross-section during the Hercynian orogeny: Journal of metamorphic Geology, v. 17, p. 157-172.

Graessner, T., Schenk, V., Bröcker, M., and Mezger, K., 2000, Geochronological constraints on the timing of granitoid magmatism, metamorphism and post-metamorphic cooling in the Hercynian crustal cross-section of Calabria: Journal of metamorphic Geology, v. 18(4), p. 409-421.

Green, H. W., and Houston, H., 1995, The mechanics of deep earthquakes: Annual Review of Earth and Planetary Sciences, v. 23(1), p. 169-213.

Guermani, A., and Pennacchioni, G., 1998, Brittle precursors of plastic deformation in a granite: an example from the Mont Blanc massif (Helvetic, western Alps): Journal of Structural Geology, v. 20(2-3), p. 135-148.

Hacker, B. R., Peacock, S. M., Abers, G. A., and Holloway, S. D., 2003, Subduction factory 2. Are intermediate-depth earthquakes in subducting slabs linked to metamorphic dehydration reactions?: Journal of Geophysical Research: Solid Earth, v. 108(B1).

Handy, M. R., and Brun, J. P., 2004, Seismicity, structure and strength of the continental lithosphere: Earth and Planetary Science Letters, v. 223(3-4), p. 427-441.

Hawemann, F., Mancktelow, N. S., Wex, S., Camacho, A., and Pennacchioni, G., 2018, Pseudotachylyte as field evidence for lower-crustal earthquakes during the intracontinental Petermann Orogeny (Musgrave Block, Central Australia): Solid Earth, v. 9(3), p. 629-648, https://doi.org/10.5194/se-9-629-2018.

Hawemann, F., Mancktelow, N. S., Pennacchioni, G., Wex, S., and Camacho, A., 2019a, Weak and slow, strong and fast: How shear zones evolve in a dry continental crust (Musgrave Ranges, Central Australia): Journal of Geophysical Research: Solid Earth, v. 124(1), p. 219-240.

Hawemann, F., Mancktelow, N., Wex, S., Pennacchioni, G., and Camacho, A., 2019b, Fracturing and crystal plasticity of garnet under seismic stress in the dry lower continental crust (Musgrave Ranges, Central Australia). Pre-print.

Hirose, T., and Shimamoto, T., 2005, Growth of molten zone as a mechanism of slip weakening of simulated faults in gabbro during frictional melting: Journal of Geophysical Research. Solid Earth, v. 110, p. B05202, 10.1029/2004JB003207.

Hirth, G., Teyssier, C., and Dunlap, J. W., 2001, An evaluation of quartzite flow laws based on comparisons between experimentally and naturally deformed rocks: International Journal of Earth Sciences, v. 90(1), p. 77-87, https://doi.org/10.1007/s005310000152.

Hobbs, B. E., Ord, A., and Teyssier, C., 1986, Earthquakes in the ductile regime?: Pure and Applied Geophysics, v. 124(1-2), p. 309-336, https://doi.org/10.1007/BF00875730.

Hollister, L. S., 1969, Contact metamorphism in the Kwoiek area of British Columbia: an end member of the metamorphic process: Geological Society of America Bulletin, v. 80(12), p. 2465-2494.

Inama, I., 2013, Evidence of primastic c-direction slip in a granulite shear zone (in italian), unpublished B.Sc. thesis, University of Padova.

Incel, S., Labrousse, L., Hilairet, N., John, T., Gasc, J., Shi, F., and Schubnel, A., 2019, Reaction-induced embrittlement of the lower continental crust: Geology, v. 47(3), p. 235-238.

Ishihara, S., Goshima, T., Iwawaki, S., Shimizu, M., and Kamiya, S., 2002, Evaluation of thermal stresses induced in anisotropic material during thermal shock: Journal of Thermal Stresses, v. 25, p. 647–661, https://doi.org/10.1080/01495730290074351.

Jackson, J. A., 2002, Strength of the continental lithosphere: time to abandon the jelly sandwich?: GSA today, v. 12, p. 4-10.

Jackson, J., McKenzie, D. A. N., Priestley, K., and Emmerson, B., 2008, New views on the structure and rheology of the lithosphere: Journal of the Geological Society, v. 165(2), p. 453-465.

Jamtveit, B., Austrheim, H., and Malthe-Sørenssen, A., 2000, Accelerated hydration of the Earth's deep crust induced by stress perturbations: Nature, v. 408(6808), p. 75.

Jamtveit, B., Austrheim, H., and Putnis, A., 2016, Disequilibrium metamorphism of stressed lithosphere: Earth-Science Reviews, v. 154, p. 1-13.

Jamtveit, B., Ben-Zion, Y., Renard, F., and Austrheim, H., 2018, Earthquake-induced transformation of the lower crust: Nature, v. 556(7702), p. 487, 10.1038/s41586-018-0045-y.

Jamtveit, B., Petley-Ragan, A., Incel, S., Dunkel, K. G., Aupart, C., Austrheim, H., and Renard, F., 2019, The Effects of Earthquakes and Fluids on the Metamorphism of the Lower Continental Crust: Journal of Geophysical Research: Solid Earth.

John, T., Medvedev, S., Rüpke, L. H., Andersen, T. B., Podladchikov, Y. Y., and Austrheim, H., 2009, Generation of intermediate-depth earthquakes by self-localizing thermal runaway: Nature Geoscience, v. 2(2), p. 137-140, DOI: 10.1038/NGEO419.

Kaus, B. J., and Podladchikov, Y. Y., 2006, Initiation of localized shear zones in viscoelastoplastic rocks: Journal of Geophysical Research: Solid Earth, v. 111(B4).

Kelemen, P. B., and Hirth, G. A., 2007, Periodic shear-heating mechanism for intermediate-depth earthquakes in the mantle: Nature, v. 446, p. 787–790. DOI: 10.1038/nature05717.

Kidder, S., Hirth, G., Avouac, J. P., and Behr, W., 2016, The influence of stress history on the grain size and microstructure of experimentally deformed quartzite: Journal of Structural Geology, v. 83, p. 194-206, https://doi.org/10.1016/j.jsg.2015.12.004.

Kilian, R., and Heilbronner, R., 2017, Analysis of crystallographic preferred orientations of experimentally deformed Black Hills Quartzite: Solid Earth, v. 8, p. 1095-1117, https://doi.org/10.5194/se-8-1095-2017.

Kilian, R., Heilbronner, R., and Stünitz, H., 2011, Quartz grain size reduction in a granitoid rock and the transition from dislocation to diffusion creep: Journal of Structural Geology, v. 33(8), p. 1265-1284, DOI: 10.1016/j.jsg.2011.05.004.

Kingery, W.D., 1955, Factors affecting thermal stress resistance of ceramic materials: Journal of the American Ceramic Society, v. 38, p. 3–15, https://doi.org/10.1111/j.1151-2916.1955.tb14545.x.

Kirby, S. H., 1983, Rheology of the lithosphere: Reviews of Geophysics, v. 21(6), p. 1458-1487.

Kirkpatrick, J. D., and Rowe, C. D., 2013, Disappearing ink: How pseudotachylytes are lost from the rock record: Journal of Structural Geology, v. 52, p. 183-198.

Kruhl, J. H., and Huntemann, T., 1991, The structural state of the former lower continental crust in Calabria (S. Italy): Geologische Rundschau, v. 80(2), p. 289-302.

Ide, S., Baltay, A., and Beroza, G. C., 2011, Shallow dynamic overshoot and energetic deep rupture in the 2011 Mw 9.0 Tohoku-Oki earthquake: Science, v. 332(6036), p. 1426-1429.

Langone, A., Gueguen, E., Prosser, G., Caggianelli, A., and Rottura, A., 2006, The Curinga-Girifalco fault zone (northern Serre, Calabria) and its significance within the Alpine tectonic evolution of the western Mediterranean: Journal of Geodynamics, v. 42(4-5), p. 140-158.

Langone, A., Godard, G., Prosser, G., Caggianelli, A., Rottura, A., and Tiepolo, M., 2010, P–T–t path of the Hercynian low-pressure rocks from the Mandatoriccio complex (Sila Massif, Calabria, Italy): new insights for crustal evolution: Journal of Metamorphic Geology, v. 28(2), p. 137-162.

Leib, S. E., Moecher, D. P., Steltenpohl, M. G., and Andresen, A., 2016, Thermobarometry of metamorphosed pseudotachylyte and associated mylonite: Constraints on dynamic Co-seismic rupture depth attending Caledonian extension, North Norway: Tectonophysics, v. 682, p. 85-95.

Lin A., 1994a, Glassy pseudotachylyte veins from the Fuyun fault zone, northwest China: Journal of Structural Geology, v. 16, p. 71–83.

Lin A., 1994b, Microlite morphology and chemistry in pseudotachylite, from the Fuyun fault zone, China: The Journal of Geology, v. 102, p. 317–329.

Lin, A., and Shimamoto, T., 1998, Selective melting processes as inferred from experimentally generated pseudotachylytes: Journal of Asian Earth Sciences, v. 16(5-6), p. 533-545.

Lin, A., Sun, Z., and Yang, Z., 2003, Multiple generations of pseudotachylyte in the brittle to ductile regimes, Qinling–Dabie Shan ultrahigh-pressure metamorphic complex, central China: Island Arc, v. 12(4), p. 423-435.

Lin, A., Maruyama, T., Aaron, S., Michibayashi, K., Camacho, A., and Kano, K. I., 2005, Propagation of seismic slip from brittle to ductile crust: Evidence from pseudotachylyte of the Woodroffe thrust, central Australia: Tectonophysics, v. 402(1-4), p. 21-35, DOI:10.1016/j.tecto.2004.10.016.

Lin, A., 2008, Seismic slip in the lower crust inferred from granulite-related pseudotachylyte in the Woodroffe thrust, Central Australia: Pure and Applied Geophysics, v. 165(2), p. 215-233.

Lloyd, G. E., Farmer, A. B., and Mainprice, D., 1997, Misorientation analysis and the formation and orientation of subgrain and grain boundaries: Tectonophysics, v. 279(1-4), p. 55-78, https://doi.org/10.1016/S0040-1951(97)00115-7.

Lu, T.J., and Fleck, N.A., 1998, The thermal shock resistance of solids: Acta Materialia, v. 46, p. 4755–4768, https://doi.org/10.1016/S1359-6454(98)00127-X.

Lund, M.G., and Austrheim, H., 2003, High-pressure metamorphism and deep-crustal seismicity: evidence from contemporaneous formation of pseudotachylytes and eclogite facies coronas: Tectonophysics, v. 372, p. 59–83, https://doi.org/10.1016/S0040-1951(03)00232-4.

Lund, M. G., Austrheim, H., and Erambert, M., 2004, Earthquakes in the deep continental crust-insights from studies on exhumed high-pressure rocks: Geophysical Journal International, v. 158(2), p. 569-576.

Maddock, R. H., 1983, Melt origin of fault-generated pseudotachylytes demonstrated by textures: Geology, v. 11(2), p. 105-108.

Maddock, R. H., 1992, Effects of lithology, cataclasis and melting on the composition of fault-generated pseudotachylytes in Lewisian gneiss, Scotland: Tectonophysics, v. 204(3-4), p. 261-278.

Magloughlin, J. F., 1989, The nature and significance of pseudotachylite from the Nason terrane, North Cascade Mountains, Washington: Journal of Structural Geology, v. 11(7), p. 907-917.

Magloughlin, J. F., and Spray, J. G., 1992, Frictional melting processes and products in geological materials: introduction and discussion: Tectonophysics, v. 204(3-4), p. 197-204.

Magloughlin, J. F., 2005, Immiscible sulfide droplets in pseudotachylyte: Evidence for high temperature (> 1200 C) melts: Tectonophysics, v. 402(1-4), p. 81-91, https://doi.org/10.1016/j.tecto.2004.11.011.

Maggi, A., Jackson, J. A., Mckenzie, D., and Priestley, K., 2000, Earthquake focal depths, effective elastic thickness, and the strength of the continental lithosphere: Geology, v. 28(6), p. 495-498.

Mancktelow, N. S., and Pennacchioni, G., 2004, The influence of grain boundary fluids on the microstructure of quartz-feldspar mylonites: Journal of Structural Geology, v. 26(1), p. 47-69, 10.1016/s0191-8141(03)00081-6.

Mancktelow, N. S., and Pennacchioni, G., 2005, The control of precursor brittle fracture and fluid–rock interaction on the development of single and paired ductile shear zones: Journal of Structural Geology, v. 27(4), p. 645-661.

Manzotti, P., and Zucali, M., 2012, The pre-Alpine tectonic history of the Austroalpine continental basement in the Valpelline unit (Western Italian Alps): Geological Magazine, v. 150(1), p. 153-172.

Manzotti, P., Ballevre, M., Zucali, M., Robyr, M., and Engi, M., 2014a, The tectonometamorphic evolution of the Sesia–Dent Blanche nappes (internal Western Alps): review and synthesis: Swiss Journal of Geosciences, v. 107(2-3), p. 309-336, DOI: 10.1007/s00015-014-0172-x.

Manzotti, P., Zucali, M., Ballevre, M., Robyr, M., and Engi, M., 2014b, Geometry and kinematics of the Roisan-Cignana Shear Zone, and the orogenic evolution of the Dent Blanche Tectonic System (Western Alps): Swiss Journal of Geosciences, v. 107(1), p. 23-47.

Menant, A., Angiboust, S., Monie, P., Oncken, O., and Guigner, J. M., 2018, Brittle deformation during Alpine basal accretion and the origin of seismicity nests above the subduction interface: Earth and Planetary Science Letters, v. 487, p. 84-93.

McNulty, B. A., 1995, Pseudotachylyte generated in the semi-brittle and brittle regimes, Bench Canyon shear zone, central Sierra Nevada: Journal of Structural geology, v. 17(11), p. 1507-1521.

Menegon, L., Nasipuri, P., Stünitz, H., Behrens, H., and Ravna, E., 2011, Dry and strong quartz during deformation of the lower crust in the presence of melt: Journal of Geophysical Research: Solid Earth, v. 116(B10).

Menegon, L., Fusseis, F., Stünitz, H., and Xiao, X., 2015, Creep cavitation bands control porosity and fluid flow in lower crustal shear zones: Geology, v. 43(3), p. 227-230, DOI:10.1130/G36307.1.

Menegon, L., Pennacchioni, G., Malaspina, N., Harris, K., and Wood, E., 2017, Earthquakes as precursors of ductile shear zones in the dry and strong lower crust: Geochemistry Geophysics Geosystems, v. 18, p. 4356–4374, https://doi.org/10.1002/2017GC007189.

Moecher, D. P., and Brearley, A. J., 2004, Mineralogy and petrology of a mullite-bearing pseudotachylyte: constraints on the temperature of coseismic frictional fusion: American Mineralogist, v. 89(10), p. 1486-1495.

Moecher, D.P., and Steltenpohl, M.G., 2009, Direct calculation of rupture depth for an exhumed paleoseismogenic fault from mylonitic pseudotachylyte: Geology, v. 37, p. 999–1002, https://doi.org/10.1130/G30166A.1.

Moore, H.E., and Sibson, R.H., 1978, Experimental thermal fragmentation in relation to seismic faulting: Tectonophysics, v. 49, p. T9–T17, https://doi.org/10.1016/0040-1951(78)90092-6.

Moresi M. Paglionico A., Piccarreta G. and Rottura A., 1978, The deep crust in Calabria (Polia-Copanello Unit): a comparison with the Ivrea-Verbano zone: Mem. Soc. Geol. Padova, v. 33, p. 233-242.

Nielsen, S., Spagnuolo, E., and Violay, M., 2012, Composite sample mount assembly (SAMOA): The ultimate sample preparation for rotary shear experiments. (Tech. Rep. 215). Istituto Nazionale di Geofisica e Vulcanologia.

Niemeijer, A., Di Toro, G., Nielsen, S., and Di Felice, F., 2011, Frictional melting of gabbro under extreme experimental conditions of normal stress, acceleration, and sliding velocity: Journal of Geophysical Research, v. 116, p. B07404. https://doi.org/10.1029/2010JB008181

O'Hara, K., 1992, Major-and trace-element constraints on the petrogenesis of a fault-related pseudotachylyte, western Blue Ridge province, North Carolina: Tectonophysics, v. 204(3-4), p. 279-288.

Ohuchi, T., Lei, X., Ohfuji, H., Higo, Y., Tange, Y., Sakai, T., Fujino, K., and Irifune, T., 2017, Intermediate-depth earthquakes linked to localized heating in dunite and harzburgite: Nature Geoscience, v. 10, p. 771-776, https://doi.org/10.1038/ngeo3011.

Paglionico and Festa, , Note illustrative della Carta Geologica d'Italia alla scala 1:50.000, Foglio 580 Soverato. Servizio Geologico d'Italia.

Papa, S., Pennacchioni, G., Angel, R.J., and Faccenda, M., 2018, The fate of garnet during (deep-seated) co-seismic frictional heating: the role of thermal shock: Geology, v. 46(5), p. 471-474, https://doi.org/10.1130/G40077.1.

Passchier, C.W., 1982, Pseudotachylyte and the development of ultramylonite bands in the Saint-Barthelemy Massif, French Pyrenees: Journal of Structural Geology, v. 4, p. 69–79, https://doi.org/10.1016/0191-8141(82)90008-6.

Passelègue, F., Spagnuolo, E., Violay, M., Nielsen, S., Di Toro, G., and Schubnel, A., 2016, Frictional evolution, acoustic emissions activity, and off-fault damage in simulated faults sheared at seismic slip rates: Journal of Geophysical Research. Solid Earth, v. 121, p. 7490–7513, https://doi.org/10.1002/2016JB012988.

Pennacchioni, G., and Cesare, B., 1997, Ductile-brittle transition in pre-Alpine amphibolite-facies mylonites during evolution from water-present to water-deficient conditions (Mont Mary nappe,

Italian Western Alps): Journal of metamorphic Geology, v. 15(6), p. 777-791, https://doi.org/10.1111/j.1525-1314.1997.00055.x.

Pennacchioni, G., Di Toro, G., and Mancktelow, N. S., 2001, Strain-insensitive preferred orientation of porphyroclasts in Mont Mary mylonites: Journal of Structural Geology, v. 23(8), p. 1281-1298, https://doi.org/10.1016/S0191-8141(00)00189-9.

Pennacchioni, G., Di Toro, G., Brack, P., Menegon, L., and Villa, I. M., 2006, Brittle–ductile–brittle deformation during cooling of tonalite (Adamello, Southern Italian Alps): Tectonophysics, v. 427(1-4), p. 171-197.

Pennacchioni, G., and Mancktelow, N. S., 2007, Nucleation and initial growth of a shear zone network within compositionally and structurally heterogeneous granitoids under amphibolite facies conditions: Journal of Structural Geology, v. 29(11), p. 1757-1780.

Pennacchioni, G., Menegon, L., Leiss, B., Nestola, F., and Bromiley, G., 2010, Development of crystallographic preferred orientation and microstructure during plastic deformation of natural coarse-grained quartz veins: Journal of Geophysical Research: Solid Earth, v. 115(B12), B12405, 10.1029/2010JB007674.

Petley-Ragan, A., Dunkel, K. G., Austrheim, H., Ildefonse, B., and Jamtveit, B., 2018, Microstructural records of earthquakes in the lower crust and associated fluid-driven metamorphism in plagioclase-rich granulites: Journal of Geophysical Research: Solid Earth, v. 123(5), p. 3729-3746.

Petley-Ragan, A., Ben-Zion, Y., Austrheim, H., Ildefonse, B., Renard, F., and Jamtveit, B., 2019, Dynamic earthquake rupture in the lower crust: Science Advances, v. 5(7).

Phillips, N.J., Rowe, C.D., and Ujiie, K., 2019, For how long are pseudotachylytes strong? Rapid alteration of basalt-hosted pseudotachylytes from a shallow subduction complex: Earth and Planetary Science Letters, v. 518, p. 108–115, https://doi.org/https://doi.org/10.1016/j.epsl.2019.04.033

Piluso, E., and Morten, L., 2004, Hercynian high temperature granulites and migmatites from the Catena Costiera, northern Calabria, southern Italy: Periodico di Mineralogia, v. 73(2), p. 159-172.

Pittarello, L., Pennacchioni, G., and Di Toro, G., 2012, Amphibolite-facies pseudotachylytes in Premosello metagabbro and felsic mylonites (Ivrea Zone, Italy): Tectonophysics, v. 580, p. 43–57, https://doi.org/10.1016/j.tecto.2012.08.001.

Pittarello, L., Habler, G., Abart, R., and Rhede, D., 2015, Garnet growth in frictional melts of the Ivrea Zone (Italy): Italian Journal of Geosciences, v. 134(1), p. 149-161.

Price, N. A., Johnson, S. E., Gerbi, C. C., and West Jr, D. P., 2012, Identifying deformed pseudotachylyte and its influence on the strength and evolution of a crustal shear zone at the base of the seismogenic zone: Tectonophysics, v. 518, p. 63-83.

Prieto, G. A., Florez, M., Barrett, S. A., Beroza, G. C., Pedraza, P., Faustino Blanco, J., Poveda, E., 2013, Seismic evidence for thermal runaway during intermediate-depth earthquake rupture: Geophysical Research Letters, v. 40(23), p. 6064–6068, doi:10.1002/2013GL058109.

Prieto, G. A., Froment, B., Yu, C., Poli, P., and Abercrombie, R., 2017, Earthquake rupture below the brittle-ductile transition in continental lithospheric mantle: Science advances, v. 3(3), p. e1602642.

Ray, S. K., 1999, Transformation of cataclastically deformed rocks to pseudotachylyte by pervasion of frictional melt: inferences from clast-size analysis: Tectonophysics, v. 301(3-4), p. 283-304.

Ray, S. K., 2004, Melt–clast interaction and power-law size distribution of clasts in pseudotachylytes: Journal of structural geology, v. 26(10), p. 1831-1843.

Reches, Z. and Dewers, T.A., 2005. Gouge formation by dynamic pulverization during earthquake rupture: Earth and Planetary Science Letters, v. 235, p. 361–374, https://doi.org/10.1016/j.epsl.2005.04.009.

Rempel, A.W., and Weaver, S.L., 2008, A model for flash weakening by asperity melting during high-speed earthquake slip: Journal of Geophysical Research, v. 113, B11308, doi:10.1029 /2008JB005649.

Rice, J.R., 2006, Heating and weakening of faults during earthquake slip: Journal of Geophysical Research, v. 111, B05311, doi:10.1029/2005JB004006.

Roda, M., and Zucali, M., 2008, Meso and microstructural evolution of the Mont Morion metaintrusive complex (Dent-Blanche nappe, Austroalpine domain, Valpelline, Western Italian Alps): BOLLETTINO-SOCIETA GEOLOGICA ITALIANA, v. 127(1), p. 105.

Rolandone, F., Bürgmann, R., and Nadeau, R. M., 2002, Time-dependent depth distribution of aftershocks: Implications for fault mechanics and crustal rheology: Seism. Res. Lett, v. 73(229), p. 2002.

Rottura, A., Del Moro, A., Pinarelli, L., Petrini, R., Peccerillo, A., Caggianelli, A., and Piccarreta, G., 1991, Relationships between intermediate and acidic rocks in orogenic granitoid suites: petrological, geochemical and isotopic (Sr, Nd, Pb) data from Capo Vaticano (southern Calabria, Italy): Chemical Geology, v. 92(1-3), p. 153-176.

Scambelluri, M., Pennacchioni, G., Gilio, M., Bestmann, M., Plümper, O., and Nestola, F., 2017, Fossil intermediate-depth earthquakes in subducting slabs linked to differential stress release: Nature Geoscience, v. 10, p. 960-966, https://doi.org/10.1038/s41561-017-0010-7.

Schenk, V., 1980, U-Pb and Rb-Sr radiometric dates and their correlation with metamorphic events in the granulite-facies basement of the Serre, southern Calabria (Italy): Contributions to Mineralogy and Petrology, v. 73(1), p. 23-38.

Schenk, V., 1981, Synchronous uplift of the lower crust of the Ivrea Zone and of southern Calabria and its possible consequences for the Hercynian orogeny in southern Europe: Earth and Planetary Science Letters, v. 56, p. 305-320.

Schenk, V., 1984, Petrology of felsic granulites, metapelites, metabasics, ultramafics, and metacarbonates from Southern Calabria (Italy): prograde metamorphism, uplift and cooling of a former lower crust: Journal of Petrology, v. 25(1), p. 255-296.

Schmalholz, S. M., Kaus, B. J., and Burg, J. P., 2009, Stress-strength relationship in the lithosphere during continental collision: Geology, v. 37(9), p. 775-778.

Schmid, S. M., and Casey, M., 1986, Complete fabric analysis of some commonly observed quartz c-axis patterns: Mineral and rock deformation: Laboratory studies, v. 36, p. 263-286, 10.1029/GM036p0263.

Shaw, B. E., and Wesnousky, S. G., 2008, Slip-length scaling in large earthquakes: The role of deep-penetrating slip below the seismogenic layer: Bulletin of the Seismological Society of America, v. 98(4), p. 1633-1641.

Shimamoto, T., and Tsutsumi, A., 1994, A new rotary-shear high-speed frictional testing machine: its basic design and scope of research (in Japanese with English abstract): J Tecton Res Group Jpn, v. 39, p. 65–78

Segall, P., and Simpson, C., 1986, Nucleation of ductile shear zones on dilatant fractures: Geology, v. 14(1), p. 56-59.

Shi, F., Wang, Y., Yu, T., Zhu, L., Zhang, J., Wen, J., and Chen, T., 2018, Lower-crustal earthquakes in southern Tibet are linked to eclogitization of dry metastable granulite: Nature communications, v. 9(1), p. 3483.

Shimada, K., Tanaka, H., Toyoshima, T., Obara, T., and Niizato, T., 2004, Occurrence of mylonite zones and pseudotachylyte veins around the base of the upper crust: Earth, planets and space, v. 56(12), p. 1217-1223.

Sibson, R.H., 1975, Generation of pseudotachylyte by ancient seismic faulting: Geophysical Journal International, v. 43, p. 775–794, https://doi.org/10.1111/j.1365-246X.1975.tb06195.x.

Sibson, R. H., 1980, Transient discontinuities in ductile shear zones: Journal of Structural Geology, v. 2(1-2), p. 165-171, https://doi.org/10.1016/0191-8141(80)90047-4.

Sibson, R.H., and Toy, V.G., 2006, The habitat of fault-generated pseudotachylyte: Presence vs. absence of friction-melt, in Abercrombie, R., et al., eds., Earthquakes: Radiated Energy and the Physics of Faulting: Washington, D.C., AGU Geophysical Monograph, v. 170, p. 153–166, https://doi.org/10.1029/170GM16.

Spear, F. S., 2017, Garnet growth after overstepping: Chemical Geology, v. 466, p. 491-499.

Spray, J. G., 1987, Artificial generation of pseudotachylyte using friction welding apparatus: simulation of melting on a fault plane: Journal of Structural Geology, v. 9(1), p. 49-60.

Spray, J. G., 1988, Generation and crystallization of an amphibolite shear melt: an investigation using radial friction welding apparatus: Contributions to Mineralogy and Petrology, v. 99(4), p. 464-475.

Spray, J.G., 1992, A physical basis for the frictional melting of some rock-forming minerals: Tectonophysics, v. 204, p. 205–221, https://doi.org/10.1016/0040-1951(92)90308-S.

Spray, J.G., 1995, Pseudotachylyte controversy: Fact or friction?: Geology, v. 23, p. 1119–1122, https://doi.org/10.1130/0091-7613(1995)023<1119:PCFOF>2.3.CO;2.

Spray, J. G., 2010, Frictional melting processes in planetary materials: From hypervelocity impact to earthquakes: Annual Review of Earth and Planetary Sciences, v. 38, p. 221-254.

Steltenpohl, M.G., Kassos, G., and Andresen, A., 2006, Retrograded eclogite-facies pseudotachylytes as deep-crustal paleoseismic faults within continental basement of Lofoten, north Norway: Geosphere, v. 2, p. 61–72, https://doi.org/10.1130/GES00035.1.

Stewart, C. A., and Miranda, E. A., 2017, The Rheological Evolution of Brittle-Ductile Transition Rocks During the Earthquake Cycle: Evidence for a Ductile Precursor to Pseudotachylyte in an Extensional Fault System, South Mountains, Arizona: Journal of Geophysical Research: Solid Earth, v. 122(12), p. 10643-10665, https://doi.org/10.1002/2017JB014680.

Stipp, M., Stünitz, H., Heilbronner, R., and Schmid, S. M., 2002, The eastern Tonale fault zone: a 'natural laboratory' for crystal plastic deformation of quartz over a temperature range from 250 to 700 °C: Journal of Structural Geology, v. 24(12), p. 1861-1884, DOI: 10.1016/S0191-8141(02)00035-4.

Swanson, M. T., 1992, Fault structure, wear mechanisms and rupture processes in pseudotachylyte generation: Tectonophysics, v. 204(3-4), p. 223-242, https://doi.org/10.1016/0040-1951(92)90309-T.

Tacchetto, T., 2014, Evidence of deformation in granulite facies on Amaroni mylonitic line: EBSD quartz application (in italian), unpublished B.Sc. thesis, University of Padova.

Takagi, H., Goto, K., and Shigematsu, N., 2000, Ultramylonite bands derived from cataclasite and pseudotachylyte in granites, northeast Japan: Journal of Structural Geology, v. 22(9), p. 1325-1339.

Thielmann, M., Rozel, A., Kaus, B. J. P., and Ricard, Y., 2015, Intermediate-depth earthquake generation and shear zone formation caused by grain size reduction and shear heating: Geology, v. 43(9), p. 791-794, https://doi.org/10.1130/g36864.1.

Thielmann, M., 2018, Grain size assisted thermal runaway as a nucleation mechanism for continental mantle earthquakes: Impact of complex rheologies: Tectonophysics, v. 746, p. 611-623, https://doi.org/10.1016/j.tecto.2017.08.038.

Thomson, S. N., 1994, Fission track analysis of the crystalline basement rocks of the Calabrian Arc, southern Italy: evidence of Oligo-Miocene late-orogenic extension and erosion: Tectonophysics, v. 238(1-4), p. 331-352.

Ting, B.Y., and Winer, W.O., 1989, Friction-induced thermal influences in elastic contact between spherical asperities: The American Society of Mechanical Engineers (ASME): Journal of Tribology, v. 111, p. 315–322, https://doi.org/10.1115/1.3261916.

Tinkham, D. K., Zuluaga, C. A., and Stowell, H. H., 2001, Metapelite phase equilibria modeling in MnNCKFMASH: the effect of variable Al2O3 and MgO/(MgO+ FeO) on mineral stability: Geological Materials Research, v. 3(1), p. 1-42.

Tokle, L., Hirth, G., and Behr, W. M., 2019, Flow laws and fabric transitions in wet quartzite: Earth and Planetary Science Letters, v. 505, p. 152-161, 10.1016/j.epsl.2018.10.017.

Toy, V. G., Prior, D. J., and Norris, R. J., 2008, Quartz fabrics in the Alpine Fault mylonites: Influence of pre-existing preferred orientations on fabric development during progressive uplift: Journal of Structural Geology, v. 30(5), p. 602-621, doi:10.1016/j.jsg.2008.01.001.

Toyoshima, T., 1990, Pseudotachylite from the Main Zone of the Hidaka metamorphic belt, Hokkaido, northern Japan: Journal of Metamorphic Geology, v. 8(5), p. 507-523.

Trepmann C.A., and Stöckhert, B., 2002, Cataclastic deformation of garnet: A record of synseismic loading and postseismic creep: Journal of Structural Geology, v. 24, p. 1845-1856, https://doi.org/10.1016/S0191-8141(02)00004-4.

Trepmann, C. A., Stöckhert, B., Dorner, D., Moghadam, R. H., Küster, M., and Röller, K., 2007, Simulating coseismic deformation of quartz in the middle crust and fabric evolution during postseismic stress relaxation—an experimental study: Tectonophysics, v. 442(1-4), p. 83-104, 10.1016/j.tecto.2007.05.005.

Tse, S. T., and Rice J. R., 1986, Crustal earthquake instability in relation to the depth variation of frictional slip properties: Journal of Geophysical Research: Solid Earth, v. 91(B9), p. 9452-9472, https://doi.org/10.1029/JB091iB09p09452.

Tsutsumi, A., and Shimamoto, T., 1997, High-velocity frictional properties of gabbro: Geophysical Research Letters, v. 24(6), p. 699-702.

Turcotte, D.L., and Schubert, G., 2002, Geodynamics (second edition): Cambridge, UK, Cambridge University Press, 456 p, https://doi.org/10.1017/CBO9780511807442.

Verberne, B. A., Chen, J., Niemeijer, A. R., de Bresser, J. H., Pennock, G. M., Drury, M. R., and Spiers, C. J., 2017, Microscale cavitation as a mechanism for nucleating earthquakes at the base of the seismogenic zone: Nature communications, v. 8(1), p. 1645.

Violay, M., Nielsen, S., Gibert, B., Spagnuolo, E., Cavallo, A., Azais, P., and Di Toro, G., 2014, Effect of water on the frictional behavior of cohesive rocks during earthquakes: Geology, v. 42, p. 27–30, https://doi.org/10.1130/G34916.1.

Wang, B.L., and Li, J.E., 2013, Thermal shock resistance of solids associated with hyperbolic heat conduction theory: Proceedings of the Royal Society of London A: Mathematical, Physical and Engineering Sciences, v. 469, p. i–xiv, DOI: 10.1098/rspa.2012.0754.

Wang, B.L., Li, J.E., and Yang, C., 2015, Thermal shock fracture mechanics analysis of a semi-infinite medium based on the dual-phase-lag heat conduction model: Proceedings of the Royal Society of

London A: Mathematical, Physical and Engineering Sciences, v. 471, 20140595, doi:10.1098/rspa.2014.0595.

Wenk, H. R., and Weiss, L. E., 1982, Al-rich calcic pyroxene in pseudotachylite: an indicator of high pressure and high temperature?: Tectonophysics, v. 84(2-4), p. 329-341.

Wex, S., Mancktelow, N., Hawemann, F., Camacho, A., and Pennacchioni, G., 2018, Inverted distribution of ductile deformation in the relatively" dry" middle crust across the Woodroffe Thrust, central Australia: Solid Earth, v. 9(4), p. 859-878.

Wex, S., Mancktelow, N. S., Camacho, A., and Pennacchioni, G., 2019, Interplay between seismic fracture and aseismic creep in the Woodroffe Thrust, central Australia–Inferences for the rheology of relatively dry continental mid-crustal levels: Tectonophysics, v. 758, p. 55-72.

White, J. C., 1996, Transient discontinuities revisited: pseudotachylyte, plastic instability and the influence of low pore fluid pressure on deformation processes in the mid-crust: Journal of Structural Geology, v. 18(12), p. 1471-1486, https://doi.org/10.1016/S0191-8141(96)00059-4.

White, J. C., 2012, Paradoxical pseudotachylyte–Fault melt outside the seismogenic zone: Journal of Structural Geology, v.38, p. 11-20, https://doi.org/10.1016/j.jsg.2011.11.016.

White, S., 1979, Grain and sub-grain size variations across a mylonite zone: Contributions to Mineralogy and Petrology, v. 70(2), p. 193-202, https://doi.org/10.1007/BF00374448.

Yardley, B. W., and Valley, J. W., 1997, The petrologic case for a dry lower crust: Journal of Geophysical Research: Solid Earth, v. 102(B6), p. 12173-12185.

Zucali, M., Manzotti, P., Diella, V., Pesenti, C., Risplendente, A., Darling, J., and Engi, M., 2011, Permian tectonometamorphic evolution of the Dent-Blanche Unit (Austroalpine domain, Western Italian Alps): Rendiconti online della Società Geologica Italiana, v. 15, p. 133-136.